Scanning gate microscopy as a tool for extracting electronic properties in quantum transport

Ousmane Ly

To cite this version:

Ousmane Ly. Scanning gate microscopy as a tool for extracting electronic properties in quantum transport. Condensed Matter [cond-mat]. Université de Strasbourg, 2017. English. NNT : 2017STRAE022 . tel-01729054

HAL Id: tel-01729054
https://theses.hal.science/tel-01729054v1

Submitted on 12 Mar 2018

UNIVERSITÉ DE STRASBOURG

ÉCOLE DOCTORALE DE PHYSIQUE ET CHIMIE-PHYSIQUE

INSTITUT DE PHYSIQUE ET CHIMIE DES MATERIAUX DE STRASBOURG

THÈSE présentée par :

Ousmane Boune Oumar LY

soutenue le : **23 Novembre 2017**

pour obtenir le grade de : **Docteur de l'Université de Strasbourg**

Discipline/ Spécialité : Physique de la matière condensée

Scanning gate microscopy as a tool for extracting local electronic properties in quantum transport

THÈSE dirigée par :

Mr. WEINMANN Dietmar	Dr, Université de Strasbourg

RAPPORTEURS :

Mr. IHN Thomas	Prof. Dr, ETH Zurich
Mr. WAINTAL Xavier	Dr, CEA Grenoble

AUTRES MEMBRES DU JURY :

Mme. GOYHENEX Christine	Dr, Université de Strasbourg	(Examinatrice)

Acknowledgments

I would like to thank my advisor Dietmar Weinmann, to whom I owe a debt of gratitude for giving me the opportunity to work with him during the past three years. I kindly appreciated all the time I passed under his supervision. I have really learned a lot of things from him, not only at the scientific level but also at the personal level. This accomplishment would not have been possible without his continuous encouragement and help.

I am also grateful to Rodolfo A. Jalabert for advises during all the period of this thesis, and for his close involvement in all the fine details of this theoretical work. Special thanks go to Christine Goyhenex, Thomas Ihn and Xavier Waintal for evaluating my work.

I would like to thank Adel Abbout, Boris Brun, Cosimo Gorini, Christina Pöltl and Guillaume Weick for useful discussions as well as Steven Tomsovic for fruitful collaboration and Keith Fratus for reading the manuscript, and all my office neighbors, Adam Brandstetter-Kunc, François Férnique, and Mauricio Gomez Viloria. I also would like to thank my colleagues from ETH Zurich, Klaus Ensslin, Thomas Ihn, Beat Braem, Carolin Gold and Richard Steinacher for collaboration and useful discussions.

I would like to express my very profound gratitude to my parents and my family for their support during my undergraduate studies.

Finally, I would like to acknowledge financial support from the doctoral school "Physique et Chimie-Physique" of the University of Strasbourg and the Mauritanian ministry of higher education and scientific research.

Contents

List of Figures

Chapter 1

General introduction to quantum transport

Advances in miniaturization of micro and nanostructures have led to the development of new theoretical and experimental aspects that have considerably deepened our understanding of condensed matter at the nanoscale. Devices with sizes smaller than the coherence length L_ϕ (the distance over which the electronic wave-function maintains a well-defined phase), have attracted particular interest of condensed matter physicists and have led to what we call mesoscpic physics, where quantum corrections are important. Besides the quantum mechanical effects we encounter when studying mesoscopic samples, some classical aspects. This is the reason why semi-classical tools have been developed [12], in order to better understand the underlying physics at such a scale.

The understanding of the quantum transport properties has led to important discoveries in the field of nanoscience.

Quantum transport is a branch of condensed matter physics that is important to the field of mesoscopic physics. It deals with the transport properties of mesoscopic devices at the quantum mechanical level. Thus, a nice mixture of classical and quantum effects is encountered. Moreover, fascinating phenomena characteristic of quantum "particles" arise.

Different regimes of quantum transport can be distinguished by comparing some characteristic length scales with the size of the studied sample. At sufficiently low temperatures the transport through a disordered conductor is said to be coherent if the coherence length L_ϕ is larger than the size L of the underlying system. Another length scale relevant for characterizing quantum transport regimes is the elastic mean free path of the electrons l, which is the typical distance between two elastic collisions with static impurity centers. If this distance is larger than L, the sample is said to be

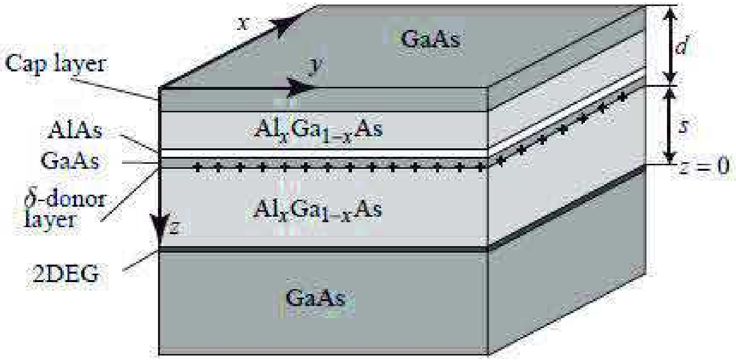

Figure 1.1: Layer sequence in a typical GaAs/AlGaAs hetero-structure with remote doping. The donor layer is situated at a distance s from the 2DEG. The figure is taken from [1].

ballistic. However if the elastic mean free path l is much smaller than the sample's size the transport is called diffusive provided that the L is smaller than the localization length ξ. In samples where L is bigger than ξ Anderson localization dominates [13].

1.1 Two dimensional electron gas

Due to the epitaxial growth techniques, the creation of electron gases with a frozen degree of freedom in the growth direction has been made possible. In these techniques, a semi-conducting material is put into contact with another semiconductor with smaller band gap. In Fig. 1.1 an AlGaAs layer is put in contact with a GaAs crystal. Since the energy band gap of the former is bigger an electrostatic potential is created by the migration of the electrons from the AlGaAs to the interface with GaAs resulting in a bending of the energy profiles as shown in Fig. 1.2. The two-dimensional electron gas forms at the interface where the Fermi energy lies inside the conduction band of GaAs.

1.2 Transport through QPCs

The quantum point contact (QPC) is an important paradigm in quantum transport and is actually one of the most investigated nanostructures. It consists of two metallic gates (see the inset of Fig. 1.3) grown on top of a

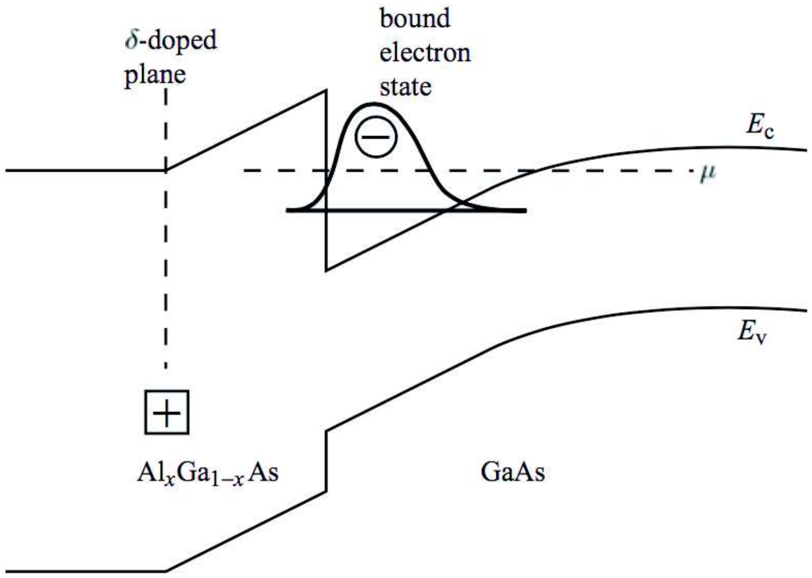

Figure 1.2: Illustration of the energy bending at the inversion layer where the 2DEG forms. The image is taken from [1].

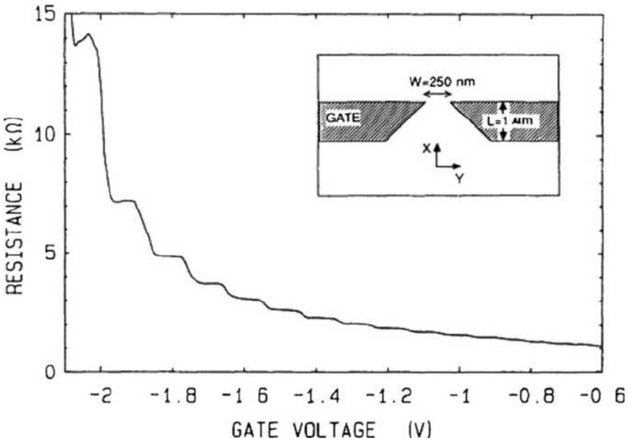

Figure 1.3: The main figure shows one of the first observations of conductance quantization. The resistance of the QPC (shown in the inset) is measured with respect to the gate voltage [2].

2DEG. As the distance between the electrostatic gates at the level of the gas is changed by applying negative voltages, the resistance (and similarly, the conductance) evolves in quantized plateaus (see Fig. 1.3) with conductance values which are multiples of $\frac{2e^2}{h}$.

In the aim at giving a description of the transport properties in QPCs we will first introduce the scattering matrix formalism and the scattering wave-functions. We will then calculate the conductance through various simplified QPC models. Relevant concepts that will be useful for the next chapters will be also introduced here.

1.3 Scattering approach to describe QPCs

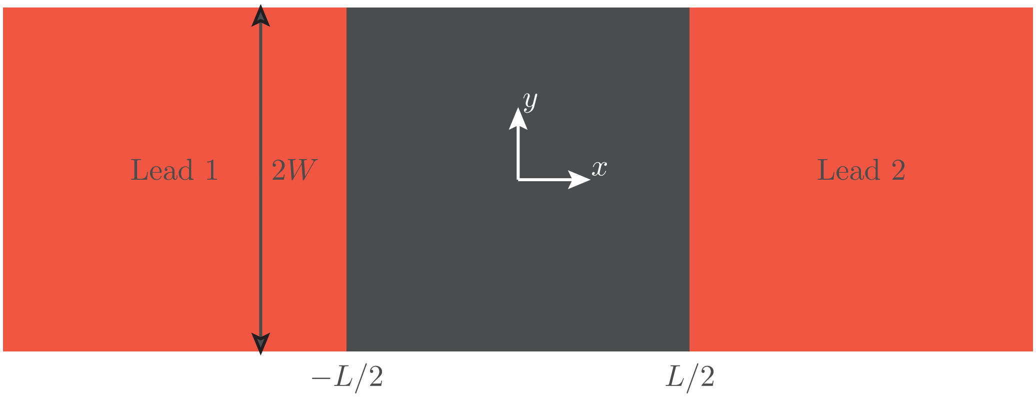

Figure 1.4: A sketch of the scattering system (black) attached to two semi infinite leads (red areas).

Let us consider a quantum scatterer attached to two 2-dimensional semi infinite waveguides of width $2W$ representing the leads (see Fig. 1.4). The wave-functions inside the waveguides are solutions of the Schrödinger equation with energy ε

$$(\varepsilon + \frac{\hbar^2}{2M_\mathrm{e}}(\partial_x^2 + \partial_y^2))\psi^{(0)}(x,y) = 0, \tag{1.1}$$

where M_e is the effective mass of the electrons. Imposing the boundary conditions

$$\psi^{(0)}(x,-W) = \psi^{(0)}(x,W) = 0, \tag{1.2}$$

the solution of (1.1) reads

$$\psi^{(0)s}_{\varepsilon a}(\mathbf{r}) = \frac{c}{\sqrt{k_a}} e^{sik_a x}\phi_a(y), \tag{1.3}$$

where $s = \pm$ stands for respectively right-moving and left-moving waves, and $c = \sqrt{\frac{M_\mathrm{e}}{2\pi\hbar^2}}$ is a convenient normalization constant leading to a current density se/h for each mode, with $s = +$ for right moving mode coming from the left lead and $s = -$ for left moving mode coming from the right lead. The ath transverse wave-function ϕ_a is given by

$$\phi_a(y) = \frac{1}{\sqrt{W}} \sin[q_a(y - W)], \tag{1.4}$$

with $q_a = \frac{\pi a}{2W}$, a integer.

The total wave-vector $k = \sqrt{k_a^2 + q_a^2}$, where k_a and q_a denote, respectively, the longitudinal and the transverse momenta, is determined by the energy

$$\varepsilon = \frac{\hbar^2 k^2}{2M_\mathrm{e}}.$$

The channels a with transverse energies $\varepsilon_a^{(t)} = \frac{\hbar^2 q_a^2}{2M_\mathrm{e}}$ smaller than ε_F are called open channels (or propagating modes). Their number is equal to

$$N = \mathrm{Int}\{2k_F W/\pi\}, \tag{1.5}$$

where the Fermi wave-vector k_F is given by

$$\varepsilon_\mathrm{F} = \frac{\hbar^2 k_F^2}{2M_\mathrm{e}}.$$

On the other hand, if the transverse energy is larger than the total energy, the corresponding longitudinal wave-number is purely imaginary, giving rise to an exponentially damped wave. These are called evanescent or closed modes since they vanish far a way from the scatterer.

Now, if the scattering potential $V(x, y)$ is considered, the solution ψ of the full Schrödinger equation can be expanded as a series in the basis of the transverse modes [14] as follows:

$$\psi^s_{l\varepsilon m}(x, y) = \sum_{a=1}^{\infty} [\psi^s_{l\varepsilon m}(x)]_a \phi_a(y), \tag{1.6}$$

l being the lead of incidence.

Inserting (1.6) into the inhomogeneous Schrödinger equation and using the differential equation

$$(\partial_y^2 + q_n^2)\phi_n(y) = 0, \tag{1.7}$$

we find

$$\sum_a (\varepsilon + \frac{\hbar^2}{2M}(\partial_x^2 - q_a^2))[\psi^s_{l\varepsilon m}(x)]_a \phi_a(y) = \sum_b [\psi^s_{l\varepsilon m}(x)]_b V(x,y)\phi_b(y), \quad (1.8)$$

writing the total energy ε as a sum of the longitudinal and the transverse energies and multiplying both sides of (1.8) by $\phi_{a'}(y)$ and integrating over y, we find that the set of coefficients α obey the equation

$$(\partial_x^2 + k_{a'}^2)[\psi^s_{l\varepsilon m}(x)]_{a'} = \sum_{b=1}^{\infty} [\psi^s_{l\varepsilon m}(x)]_b \mathcal{V}_{a'b}(x), \quad (1.9)$$

with

$$\mathcal{V}_{a'b}(x) = \frac{2M}{\hbar^2} \int_{-W}^{W} \phi_{a'}(y)V(x,y)\phi_b(y)\mathrm{d}y. \quad (1.10)$$

Notice that the sum in the left hand side of Eq. (1.8) has disappeared due to the Kronecker delta resulting from the scalar product of two transverse wave-functions.

Considering the right hand side of (1.9) as the inhomogeneous part of an otherwise homogeneous equation one introduces the unperturbed Green function $\mathcal{G}_s^{(0)}$ for the open channels given by [14]

$$\mathcal{G}_s^{(0)}(x, x', \varepsilon_a) = 2s\pi c^2 \frac{e^{isk_a|x-x'|}}{ik_a}, \quad (1.11)$$

and satisfying

$$(\partial_x^2 + k_a^2)\mathcal{G}_s^{(0)}(x, x', \varepsilon_a) = \delta(x - x'),, \quad (1.12)$$

this allows us to write

$$[\psi^s_{l\varepsilon a_0}(x)]_a = \delta_{a,a_0} \frac{c}{\sqrt{k_a}} e^{sik_a x} + \sum_{b=1}^{\infty} \int \mathcal{G}_s^{(0)}(x, x', \varepsilon_a)\mathcal{V}_{ab}(x')[\psi^s_{l\varepsilon a_0}(x')]_b dx'. \quad (1.13)$$

For the closed channels the corresponding Green function is obtained by taking k_a purely imaginary in (1.11).

The Eq. (1.13) is the Lippmann-Schwinger equation for the components $[\psi^s_{l\varepsilon a_0}(x)]_a$.

The general form of the Lipmann-Schwinger equation in arbitrary dimension d, that expresses the scattering wave-functions in terms of the unperturbed quantities is given by

$$\boxed{\psi_{l\varepsilon a}(\mathbf{r}) = \psi^{(0)}_{l\varepsilon a}(\mathbf{r}) + \int \mathrm{d}\bar{\mathbf{r}} \mathcal{G}^{(0)}(\mathbf{r}, \bar{\mathbf{r}}, \varepsilon) V(\bar{\mathbf{r}}) \psi_{l\varepsilon a}(\bar{\mathbf{r}})} \quad (1.14)$$

where $\mathcal{G}^{(0)}$ is the $d-$dimensional Green function constructed from the unperturbed wave-functions $\psi^{(0)}$ as

$$\boxed{\mathcal{G}^{(0)}(\mathbf{r},\bar{\mathbf{r}},\varepsilon)=\sum_{\bar{l}=1}^{2}\int_{\varepsilon_1^{(\mathrm{t})}}^{\infty}\frac{\mathrm{d}\bar{\varepsilon}}{\varepsilon^{+}-\bar{\varepsilon}}\sum_{\bar{a}=1}^{\bar{N}}\ \psi^{(0)*}_{\bar{l},\bar{\varepsilon},\bar{a}}(\bar{\mathbf{r}})\psi^{(0)}_{\bar{l},\bar{\varepsilon},\bar{a}}(\mathbf{r})} \tag{1.15}$$

1.4 Asymptotic form of the scattering wave-functions

Using the expression of the Green function (1.11) for $x > \frac{L}{2}$ in the Eq. (1.13) and considering the incidence from a channel a_0 in the left ($s=+$), we are left with [14]

$$[\psi^{+}_{1\varepsilon a_0}(x)]_a=\delta_{a,a_0}\frac{c}{\sqrt{k_{a_0}}}e^{ik_{a_0}x}-2\pi i\frac{c}{\sqrt{k_a}}e^{ik_a x}\sum_{b=1}^{\infty}\int\frac{c}{\sqrt{k_a}}e^{-ik_a x'}\mathcal{V}_{ab}(x')[\psi^{+}_{1\varepsilon a_0}(x')]_b dx'. \tag{1.16}$$

Similarly, in the left of the scatterer one can write

$$[\psi^{+}_{1\varepsilon a_0}(x)]_a=\delta_{a,a_0}\frac{c}{\sqrt{k_{a_0}}}e^{ik_{a_0}x}-2\pi i\frac{c}{\sqrt{k_a}}e^{-ik_a x}\sum_{b=1}^{\infty}\int\frac{c}{\sqrt{k_a}}e^{ik_a x'}\mathcal{V}_{nm}(x')[\psi^{+}_{1\varepsilon a_0}(x')]_b dx'. \tag{1.17}$$

Since the Schrödinger equation is linear, the linear combination $\alpha^{ns}_{l\varepsilon}$ of the $2N$ coefficients $[\psi^{s}_{l\varepsilon n_0}(x)]_n$ constitutes a solution of the Schrödinger equation for the same energy. It can be written as

$$\alpha^{ns}_{l\varepsilon}(x)=\sum_{n_0}^{N}(a^{(1)}_{n_0}[\psi^{s}_{1\varepsilon n_0}(x)]_n+a^{(2)}_{n_0}[\psi^{s}_{2\varepsilon n_0}(x)]_n), \tag{1.18}$$

where $a^{(1)}_{n_0}$ and $a^{(2)}_{n_0}$ with $1\leq N$, are some arbitrary coefficients. Since $[\psi^{s}_{l\varepsilon n_0}(x)]_n$ are linear combinations of the plane waves $\frac{c}{\sqrt{k_n}}e^{isk_n x}$ according to (1.13), $\alpha^{ns}_{1\varepsilon}(x)$ can be written as a linear combination of the same plane waves as

$$\alpha^{n+}_{1\varepsilon}(x)=\begin{cases}\frac{c}{\sqrt{k_n}}(a^{(1)}_n e^{ik_n x}+b^{(1)}_n e^{-ik_n x}) & x<-L/2\\ \frac{c}{\sqrt{k_n}}(a^{(2)}_n e^{-ik_n x}+b^{(2)}_n e^{ik_n x}) & x>L/2\end{cases} \tag{1.19}$$

where $a^{(l)}_n$ stands for the incoming amplitudes from lead l and $b^{(l)}_n$ the outgoing ones, and $1\leq n\leq N$.

Plugging the asymptotic form of the coefficients $[\psi_{l\varepsilon m}]_a$ in (1.6) the asymptotic behavior of the scattering wave-functions can be obtained [14].

1.5 Scattering matrix

The $2N$ by $2N$ matrix S relating the $2N$ vectors $a = \left(\begin{array}{c} a^{(1)} \\ a^{(2)} \end{array}\right)$ and $b = \left(\begin{array}{c} b^{(1)} \\ b^{(2)} \end{array}\right)$ as :

$$b = Sa \tag{1.20}$$

This is the definition of the scattering matrix in the basis of the lead wavefunctions (1.3).

The scattering matrix can be written in terms of the reflection $r(r')$ and transmission $t(t')$ submatrices, where the unprimed quantities are those corresponding to the incidence from the left lead and the primed ones correspond to incidence from the right

$$\boxed{S = \left(\begin{array}{cc} r & t' \\ t & r' \end{array}\right)} \tag{1.21}$$

According to the asymptotic coefficients in (1.17) and (1.16) one can obtain the explicit form of the reflection and transmission submatrices as

$$r_{nn_0} = -2\pi i \sum_{m=1}^{\infty} \int \frac{c}{\sqrt{k_n}} e^{ik_n x} V_{nm}(x) [\psi^+_{1\varepsilon n_0}(x)]_m dx, \tag{1.22}$$

and

$$t_{nn_0} = \delta_{n,n_0} - 2\pi i \sum_{m=1}^{\infty} \int \frac{c}{\sqrt{k_n}} e^{-ik_n x} V_{nm}(x) [\psi^+_{1\varepsilon n_0}(x)]_m dx. \tag{1.23}$$

r_{nn_0} is simply the amplitude of the reflected wave in channel n when incidence is from n_0 and t_{nn_0} is the amplitude of the transmitted wave in channel n when incidence is from n_0 in the left lead. In order to obtain the matrix elements of r' and t' we have to consider the incidence to be from the right.

1.6 Unitarity and symmetry of the scattering matrix

The conservation of the current imposes that the current flowing towards the system has to be equal in absolute value to the one flowing outwards of it. This conservation law reads

$$b^\dagger b = a^\dagger a, \tag{1.24}$$

now starting from (1.20) one can write

$$b^\dagger b = a^\dagger S^\dagger S a, \tag{1.25}$$

with the current conservation law (1.24) the scattering matrix S has to be unitary

$$S^\dagger = S^{-1}. \tag{1.26}$$

Another remarkable feature of the matrix S of a time reversal invariant system, is its symmetry property. In fact, for a system with time reversal symmetry the complex conjugate of (1.19) leads to the time reversal partner of the scattering wave-function (1.6). The corresponding coefficients of such scattering state are

$$\alpha_{l\varepsilon}^{n+*}(x) = \begin{cases} \frac{c}{\sqrt{k_n}}(a_n^{(1)*}e^{-ik_nx} + b_n^{(1)*}e^{ik_nx}) & x < -L/2 \\ \frac{c}{\sqrt{k_n}}(a_n^{(2)*}e^{ik_nx} + b_n^{(2)*}e^{-ik_nx}) & x > L/2 \end{cases} \tag{1.27}$$

Since the time reversal partner of the scattering wave-function is a solution of the corresponding Schrödinger equation with the same energy, the amplitudes in (1.27) are related by the same scattering matrix S

$$a^* = Sb^*, \tag{1.28}$$

the complex conjugation of (1.28) with inversion leads to

$$b = (S^*)^{-1}a, \tag{1.29}$$

therefore using the unitarity of S (1.25) we obtain the relation

$$S = S^T, \tag{1.30}$$

expressing the symmetry property of the scattering matrix of a spinless system with time-reversal symmetry.

1.7 Scattering wave-functions in the transmission eigenbasis

In the basis of the $2N$ incoming and outgoing modes, the scattering matrix is defined by (1.21).

However it is more convenient to write S using the polar decomposition [14]. In the case of time-reversal symmetry, S takes the form

$$S = \begin{pmatrix} u_1^{\mathrm{T}} & 0 \\ 0 & u_2^{\mathrm{T}} \end{pmatrix} \begin{pmatrix} -\mathcal{R} & \mathcal{T} \\ \mathcal{T} & \mathcal{R} \end{pmatrix} \begin{pmatrix} u_1 & 0 \\ 0 & u_2 \end{pmatrix}. \tag{1.31}$$

$\mathcal{R}$ and $\mathcal{T}$ are diagonal reflection and transmission submatrices with real entries, while u_1 and u_2 are unitary matrices.

The transmission eigenmodes (forming the transmission eigenbasis in which the current matrix is diagonal) can be written as linear combinations of the lead modes (1.3). If we shrink the scatterer into $x = 0$, the transmission eigenmodes are given by [15]

$$\begin{aligned} \varrho^{(-)}_{1,\varepsilon,m}(\mathbf{r}) &= \textstyle\sum_{a=1}^{N} [u_1]^*_{ma} \;\; \varphi^{(-)}_{1\varepsilon a}(\mathbf{r})\,, \quad x < \;0\;, \\ \varrho^{(-)}_{2,\varepsilon,m}(\mathbf{r}) &= \textstyle\sum_{a=1}^{N} [u_2]^*_{ma} \;\; \varphi^{(-)}_{2\varepsilon a}(\mathbf{r})\,, \quad x > \;0\;, \end{aligned} \tag{1.32}$$

with

$$\begin{aligned} \varphi^{(\pm)}_{1,\varepsilon,a}(\mathbf{r}) &= \tfrac{c}{\sqrt{k_a}} e^{\mp i k_a x} \phi_a(y)\,, \quad x < \;0\;, \\ \varphi^{(\pm)}_{2,\varepsilon,a}(\mathbf{r}) &= \tfrac{c}{\sqrt{k_a}} e^{\pm i k_a x} \phi_a(y)\,, \quad x > \;0\;. \end{aligned} \tag{1.33}$$

Identifying (1.21) and (1.31), the transmission and reflection submatrices can be expressed as $t = u_2^T \mathcal{T} u_1$, $t' = u_1^T \mathcal{T} u_2$, $r = -u_1^T \mathcal{R} u_1$, and $r' = u_2^T \mathcal{R} u_2$. Thus, $t^\dagger t = u_1^\dagger \mathcal{T}^2 u_1$ and $t'^\dagger t' = u_2^\dagger \mathcal{T}^2 u_2$.

Considering the vector of coefficients $C_{1(2)m} = ([u^*_{1(2)}]_{m1}, [u^*_{1(2)}]_{m2}, ...)^T$ of the transmission eigenmode $\varrho^{(-)}_{1,\varepsilon,m}(\mathbf{r})$, one can write

$$t^\dagger t C_{1m} = u_1^\dagger \mathcal{T}^2 u_1 C_{1m} = \mathcal{T}_m^2 C_{1m}\,. \tag{1.34}$$

The second equality stems from the definition of C_{1m} and implies that C_{1m} is an eigenvector of $t^\dagger t$ with the eigenvalue $\mathcal{T}_m^2$. In the same way, one finds that C_{2m} is an eigenvector of $t'^\dagger t'$ with the same eigenvalue.

The scattering eigenstates in the region $x > 0$ for an incoming transmission eigenmode $\varrho^{(-)}_{1,\varepsilon,m}(\mathbf{r})$ are obtained as $tC_{1m} = u_2^T \mathcal{T} u_1 C_{1m}$. Using again the definition of $C_{1(2)m}$ and the unitarity of u_1 we find

$$tC_{1m} = \mathcal{T}_m C^*_{2m}\,, \tag{1.35}$$

and similarly

$$rC_{1(2)m} = \mp \mathcal{R}_m C^*_{1(2)m}\,. \tag{1.36}$$

Thus, the basis of scattering eigenfunctions is asymptotically given by

$$\boxed{\begin{aligned} \chi_{1,\varepsilon,m}(\mathbf{r}) \quad &= \begin{cases} \varrho^{(-)}_{1,\varepsilon,m}(\mathbf{r}) - \mathcal{R}_m\, \varrho^{(+)}_{1,\varepsilon,m}(\mathbf{r}), & x < 0 \\ \mathcal{T}_m\, \varrho^{(+)}_{2,\varepsilon,m}(\mathbf{r}), & x > 0 \end{cases} \\ \chi_{2,\varepsilon,m}(\mathbf{r}) \quad &= \begin{cases} \mathcal{T}_m\, \varrho^{(+)}_{1,\varepsilon,m}(\mathbf{r}), & x < 0 \\ \varrho^{(-)}_{2,\varepsilon,m}(\mathbf{r}) + \mathcal{R}_m\, \varrho^{(+)}_{2,\varepsilon,m}(\mathbf{r}), & x > 0 \end{cases} \;. \end{aligned}} \tag{1.37}$$

This basis is very convenient and useful when discussing the conductance formulas of the perturbation theory that will be presented in the following chapter.

1.8 Landauer-Büttiker approach for quantum conductance

The Kubo formalism [16] is the traditional framework for evaluating the response functions of non-equilibrium systems in terms of equilibrium correlations up to first order in the forces driving the system out of equilibrium. Instead of using the Kubo approach, Rolf Landauer [17] used a counting argument as well as the Einstein relation between diffusion constant and mobility in order to express the conductance of a disordered one-dimensional conductor in terms of its reflection and transmission coefficients. Therefore, in the Landauer approach the transport problem is reduced to a quantum mechanical scattering problem. To obtain the quantum conductance formula let us consider the same system as the one we considered in the first section of this chapter.

The matrix elements of the current density operator in the transmission eigenbasis is

$$[j(\mathbf{r})]^{\bar{l}l}_{\bar{m}m}(\bar{\varepsilon},\varepsilon) = \frac{e\hbar}{2iM_\mathrm{e}}\left[\chi^*_{\bar{l},\bar{\varepsilon},\bar{m}}(\mathbf{r})\;\partial_x\chi_{l,\varepsilon,m}(\mathbf{r}) - \chi_{l,\varepsilon,m}(\mathbf{r})\;\partial_x\chi^*_{\bar{l},\bar{\varepsilon},\bar{m}}(\mathbf{r})\right], \quad (1.38)$$

where l and $\bar{l}$ stand for lead indices. Its diagonal matrix element $j_{l\varepsilon m}$ represents the current density associated to the scattering state $\chi_{l,\varepsilon,m}$. Considering that the incidence is from the left we shall take $l = 1$.

Using the expression of $\chi_{1,\varepsilon,m}$ in (1.38) and taking the diagonal matrix element we have for $x > 0$

$$j_{1\varepsilon m}(\mathbf{r}) = \mathcal{T}^2_m\left[\frac{e\hbar}{2iM_\mathrm{e}}\left(\varrho^{(-)}_{2,\varepsilon,m}(\mathbf{r})\;\partial_x\varrho^{(+)}_{2,\varepsilon,m}(\mathbf{r}) - \varrho^{(+)}_{2,\varepsilon,m}(\mathbf{r})\;\partial_x\varrho^{(-)}_{2,\varepsilon,m}(\mathbf{r})\right)\right], \quad (1.39)$$

since the lead wave-functions $\varphi^{(\pm)}_{l\varepsilon a}(\mathbf{r})$ are normalized such that the current carried by each mode is e/h, the same holds for the states $\varrho^{(\pm)}_{l\varepsilon m}(\mathbf{r})$ of the transmission eigenbasis. Therefore the quantity between brackets in (1.39) after integration over y reduces to e/h, and thus the energy dependent current of each mode m is simply

$$\mathcal{I}_{1\varepsilon m} = \frac{e}{h}\mathcal{T}^2_m. \quad (1.40)$$

The current flowing between two reservoirs set at different chemical potentials μ_1 and μ_2 is

$$I_1 = \frac{e}{h}\int_{\mu_1}^{\mu_2}\sum_m \mathcal{T}^2_m(f_1 - f_2)\mathrm{d}\varepsilon, \quad (1.41)$$

where f_l is the Fermi-Dirac distribution of the electrons in lead l with chemical potential μ_l.

At zero temperature the derivative of the Fermi-Dirac distribution function with respect to the energy variable reduces to a Dirac delta, and the current is given in first order to the applied bias $V = \frac{\mu_1 - \mu_2}{e}$ by

$$I_1 = \frac{2e^2}{h} \sum_m \mathcal{T}_m^2 V, \tag{1.42}$$

where the factor 2 is for spin degeneracy. We define the dimensionless zero temperature linear conductance $g = I_1/V$ (i.e in units of $G_0 = \frac{2e^2}{h}$) as

$$\boxed{g = \mathrm{Tr}[\mathcal{T}^2] = \mathrm{Tr}[t^\dagger t]} \tag{1.43}$$

The previous derivation gives the two-probe multichannel conductance formula provided by Daniel Lee and Patrick Fisher as a generalization [18] of the original formula proposed by Landauer for a one dimensional disordered conductor [17]. The multiprobe version of (1.43) has been later proposed by Markus Büttiker [19].

The formula (1.43) implies that a fully transmitting one dimensional wire (e.g) would have a finite resistance of $\frac{h}{2e^2}$. This counter-intuitive observation has led to a controversy in the mesoscopic community [20]. It was only later, that this residual resistance has been understood [21, 22] to be arising from the contact between the electron reservoirs and the conducting wire.

Although the initial Landauer formula has been derived in the single electron scattering picture, a similar formula for the quantum conductance of an interacting scatterer has been derived [23] in the non-equilibrium Keldish Green function framework by Yigal Meir and Ned S. Wingreen.

1.9 Conductance of a narrow-wide geometry

Following the discussion of Ref. [24], let us consider the narrow-wide (NW) geometry sketched in Fig.1.5.

The asymptotic behavior of the scattering wave functions coming from the left lead with energy ε in the narrow region can be written as

$$\psi_{1\varepsilon a}(x, y) = \frac{c}{\sqrt{k_a}} \Phi_a(y) e^{ik_a x} + \sum_b \frac{c}{\sqrt{k_b}} \Phi_b(y) r_{ba} e^{-ik_b x}, \tag{1.44}$$

and,

$$\psi_{1\varepsilon a}(x, y) = \sum_b \frac{c}{\sqrt{K_b}} \phi_b(y) t_{ba} e^{iK_b x}, \tag{1.45}$$

in the wide region, where Φ and ϕ are the transverse wave-functions in the wide and the narrow regions and K_a, k_a the longitudinal momenta in the two regions given by $K_a = \sqrt{k^2 - (\pi a/2W)^2}$ and $k_a = \sqrt{k^2 - (\pi a/2w)^2}$ with k the total momentum.

Matching the wave-functions and their derivatives at the interface between the two regions ($x = 0$) we obtain

$$\Phi_a(y) + \sum_b \sqrt{\frac{K_a}{k_b}} r_{ba} \Phi_b(y) = \sum_b t_{ba} \sqrt{\frac{K_a}{k_b}} \phi_b(y), \tag{1.46}$$

$$\Phi_a(y) - \sum_b \sqrt{\frac{k_b}{K_a}} r_{ba} \Phi_b(y) = \sum_b t_{ba} \sqrt{\frac{k_b}{K_a}} \phi_b(y). \tag{1.47}$$

Multiplying (1.46) by Φ_m and (1.47) by ϕ_m and integrating over the transverse direction we get

$$\delta_{am} + \sqrt{\frac{K_a}{k_m}} r_{ma} = \sum_b t_{ba} \sqrt{\frac{K_a}{k_b}} \mathcal{O}_{bm}, \tag{1.48}$$

$$\mathcal{O}_{am} - \sum_b \sqrt{\frac{k_b}{K_a}} r_{ba} \mathcal{O}_{bm} = \sqrt{\frac{k_m}{K_a}} t_{ma}. \tag{1.49}$$

here we have introduced the overlap $\mathcal{O}$ between the transverse wave functions in the two regions, it is given by

$$\mathcal{O}_{bm} = \int_{-W}^{W} \Phi_b(y) \phi_m(y) \Theta(w - |y|) dy, \tag{1.50}$$

where Θ is the Heaviside step-function.

Eliminating r_{ma} between (1.48) and (1.49) we arrive at the set of equations

$$\sqrt{K_m} t_{ma} + \sum_b \frac{t_{ba}}{\sqrt{K_b}} A_{bm} = 2\sqrt{k_a} \mathcal{O}_{am}, \tag{1.51}$$

with

$$A_{bm} = \sum_n k_n \mathcal{O}_{bn} \mathcal{O}_{nm}. \tag{1.52}$$

1.10 Mean field approximation

The equations (1.48) and (1.49) can be solved exactly numerically or by further analytic considerations [24].

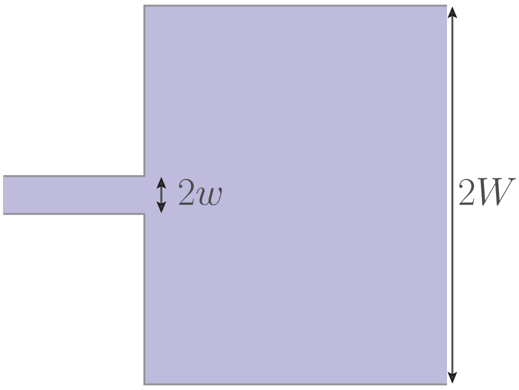

Figure 1.5: A sketch of the wide-narrow geometry.

However, noticing that the square of the overlap $\mathcal{O}_{nw}$ is peaked at w such that the transverse momenta in both regions match $q_n = q_w$, Szafer and Stone [24] have introduced the mean field approximation (MFA) stipulating that A_{nm} is small for n different to m. This has allowed to approximate the true overlaps by a uniform coupling to all modes within one level spacing of the corresponding transverse energy in the narrow region. In this approximation A_{nm} is found to be diagonal [24, 15]. Thus we can write

$$A_{nm} = \mathcal{K}_n \delta_{nm} \tag{1.53}$$

with $\mathcal{K}_n$ the average value of the longitudinal wave-number in the momentum interval $[Q_{n-1}, Q_{n+1}]$ where the overlap is appreciably different from zero, with $Q_n = \frac{\pi n}{2W}$.

Within the MFA, the average longitudinal wave-number $\mathcal{K}_n$ is given by

$$\mathcal{K}_n = \frac{w}{\pi} \int_{Q_{n-1}}^{Q_{n+1}} \mathrm{d}q \sqrt{k^2 - q^2}. \tag{1.54}$$

The transmission matrix elements in (1.51) can be expressed in term of $\mathcal{K}$ as

$$t_{ba} = 2\sqrt{k_a K_b} \frac{\mathcal{O}_{ba}}{K_b + \mathcal{K}_b}. \tag{1.55}$$

The conductance g_n of a given mode n is then found by summing $|t_{na}|^2$ over all the open channels :

$$\boxed{g_n = \sum_a |t_{na}|^2 = \frac{4K_n \mathrm{Re}\{\mathcal{K}_\mathrm{n}\}}{|K_n + \mathcal{K}_n|^2}} \tag{1.56}$$

It is worth noting that the contribution of the evanescent modes to the conductance (1.56) is incorporated by taking the corresponding K_n purely imaginary.

1.11 Conductance of a wide-narrow-wide geometry

Although the NW geometry captures the most important feature observed in QPCs being the conductance quantization [24], the wide-narrow-wide model (WNW) (see Fig. 1.6) is more similar to the realistic QPCs.

Writing the scattering wave functions in each part of the geometry and processing in the same way we have done for the NW geometry we obtain that the conductance of the nth channel through the narrow region is given by:

$$\boxed{g_n = \frac{4K_n^2 \mathrm{Re}\{\mathcal{K}_n\}^2}{|D_n|^2}} \tag{1.57}$$

where K_n is the longitudinal momentum in the narrow region, $\mathcal{K}_n$ the average momentum (calculated in Appendix A) and D_n is given by

$$D_n = (K_n + \mathcal{K}_n)^2 e^{-iK_nL} - (K_n - \mathcal{K}_n)^2 e^{iK_nL}. \tag{1.58}$$

In Ref. [24], Szafer and Stone have obtained a differently written formula for g_n. But we can show that the two formulas are equivalent (see Appendix B).

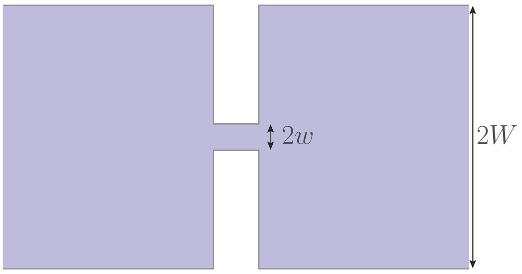

Figure 1.6: A sketch of the wide-narrow-wide geometry.

In Fig. 1.7, the conductance of the WNW geometry is plotted with respect to kw, for different lengths of the constriction. In addition to the quantized behaviour, this figure shows oscillation features that increases with increasing length. These oscillations are due to the constructive an destructive interference between the traveling channels.

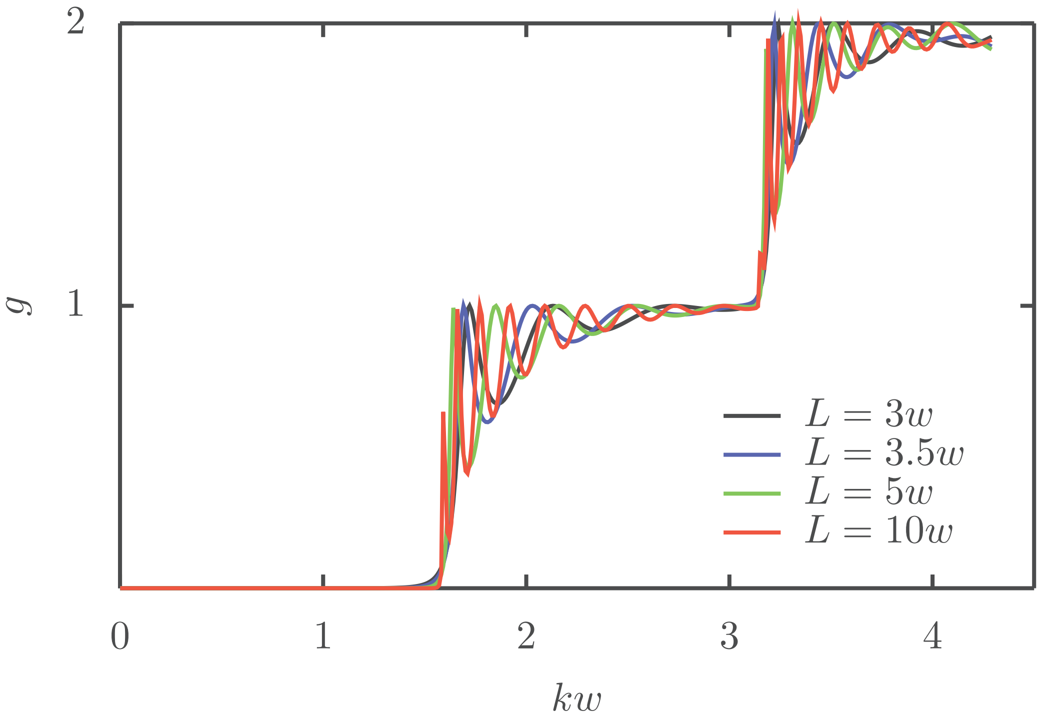

Figure 1.7: The conductance through the (WNW) geometry given by Eq.(1.57), is plotted versus kw for different lengths of the QPC.

1.12 Adiabatic QPCs

An ideal way to understand the quantized behavior of the conductance is achieved by considering a wire with finite width perfectly matching with the electron reservoirs. In this simplified picture a transport channel is either transmitted or fully reflected to the initial lead it comes from, and the total conductance is given by the number of the transmitted channels N which changes in unit steps with the width of the wire or the Fermi energy E_F of the incoming electrons that is

$$G = \frac{2e^2}{h} N(E_F). \tag{1.59}$$

If now we assume an abrupt constriction inside the wire which plays the role of a QPC the quantization of G is modified by Fabri-Perot oscillations due to interferences inside the constriction (see Fig. 1.7).

However, if the narrowing of the constriction is not uniform as shown in Fig. 1.8 the conductance quantization (shown in the main figure of Fig. 1.3) is surprising.

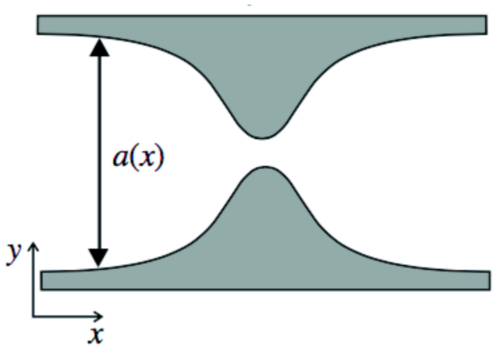

Figure 1.8: Example of an adiabatic QPC with variable cross section $a(x)$. The figure is taken from [3].

In the case of uniform narrowing of the QPC, we were able to separate the Schrödinger equation and match the wave-functions at the boundaries of the system. However, in the case of not uniform narrowing this is not possible in general.

To study the role of the continuously varying potential and why the quantization is still observed in such geometries Glazman [25] assumed the transition from the narrow constriction to the leads to be slow and smooth compared to the scale of the Fermi wavelength in the so-called adiabatic approximation. In this approximation, the solution of the Schrödinger equation can be locally separated as follows [3]

$$\psi_n(x,y) = \psi(x)\phi_n(a(x),y), \tag{1.60}$$

with $a(x)$ is the x dependent cross section (see Fig. 1.8). The local flatness of the constriction implies that the first derivative of $a(x)$ can be neglected. Therefore, the 2-dimensional Schrödinger equation leads to a simple effective one-dimensional one [3]

$$(-\frac{\hbar^2}{2M}\partial_x^2 + E_n(x))\psi(x) = E\psi(x), \tag{1.61}$$

where E_n is a channel-dependent energy playing the role of the transverse energy in the uniform narrowing problem, it is given by

$$E_n(x) = \frac{\pi\hbar^2}{2M}\frac{n^2}{a^2(x)}. \tag{1.62}$$

In Fig. 1.9, $E_n(x)$ is plotted versus the x, it shows that for each electronic channel a potential barrier is forming in the narrowest region of the constric-

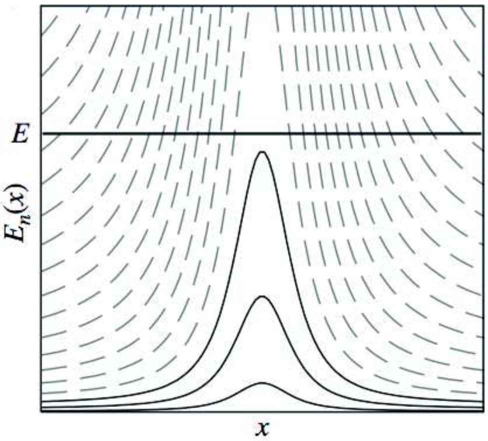

Figure 1.9: Effective potential energy for transport channels at given energy E. Three open channels are shown (solid lines). The dashed lines correspond to the closed channels. The figure is adapted from [3].

tion. So at given energy E a finite number of channels is transmitted, and the quantization of conductance is observed.

Furthermore, Glazman has shown that in the adiabatic approximation, the shape of the conductance steps depends only on the curvature at the center of the constriction and on its length. He found that the adiabatic correction to the n^{th} perfectly quantized conductance is

$$\delta G(z) = \frac{2e^2}{h}(1 + e^{-z\pi\sqrt{2R/d}})^{-1}, \tag{1.63}$$

with $z = \frac{k_F d}{\pi} - n$, d and R are the diameter and the radius of curvature at the center of the constriction and k_{F} is the Fermi wave-number. Therefore the quality of the conductance steps is governed by the local curvatures of the adiabatic QPC. In other words the conductance at the n^{th} quantized plateau is

$$G = \frac{2e^2}{h}(n - 1 + \frac{h}{2e^2}\delta G). \tag{1.64}$$

In the adiabatic approximation, the knowledge of the exact form of the confining potential is not relevant. However if a parabolic confinement is assumed the scattering problem can be exactly solved [26], yielding a similar smooth conductance behavior [27].

1.13 Numerical simulation package for quantum transport (KWANT)

In order to be able to obtain the underlying physical quantities in quantum transport, the exact solution of the Schrödinger equation is required. Unfortunately, this task cannot be analytically done except for very few physical systems.

In addition to this difficulty, the scattering wave-functions which are fundamental objects in any scattering problem involve matching conditions between different pieces of the studied system. This makes the analytical description of an arbitrary scattering problem a very difficult task. Thus, as in many other fields of physics, numerical simulations are useful and have been introduced. For this purpose, numerical methods and algorithms [28, 29] have been proposed in order to solve special scattering problems. Subsequently, different implementations of these algorithms have been adopted.

Within the idea of providing a general and unifying easy to use platform for quantum transport, a group of physicists has proposed the highly efficient software package Kwant [30] that uses sparse linear algebra library [31] to efficiently solve the underlying scattering problem.

In Kwant, the Schrödinger equation is discretized in a tight binding network in which the Hamiltonian can be written as

$$H = \sum_{ab} H_{ab} c_a^\dagger c_b, \tag{1.65}$$

where $c_a^\dagger (c_b)$ are the usual fermionic creation (annihilation) operators, a and b are indices encoding the lattice sites and the underlying degrees of freedom. To simulate a physical open system a finite number of semi infinite leads can be attached to it. This yields a priori an infinite system. However, using the translational symmetry of the leads allows to tackle the physical system. The eigenstates of the translational operator in a given lead are a product of plane waves propagating along the longitudinal direction with transversal ones, they read [30]

$$\phi_n(b) = e^{ibk_n} \chi_n, \tag{1.66}$$

with i the imaginary unit. The scattering wave-functions in the leads are then given by

$$\psi_n(j) = \phi_n^{in}(j) + \sum_{m=1}^{N} S_{mn} \phi_m^{out}(j) + \sum_{m=N+1}^{\infty} \tilde{S}_{mn} \phi_m^{ev}(j) \tag{1.67}$$

with S the scattering matrix of the propagating modes, $\tilde{S}$ the one for the evanescent modes ϕ^{ev}, for which the longitudinal momentum k_n is purely imaginary, and N is the number of the open modes. *in* (and *out*) stands respectively for incoming and outgoing waves. The scattering matrix S and the scattering wave function ϕ^S inside the system (which is here a matrix containing the system states corresponding to different incoming modes) are the main outputs we will get from Kwant. They can be found by appropriately solving the Schrödinger equation $H\psi = E\psi$ [32]. Another object we can also obtain as an output from Kwant is the Green function which is computed by simple matrix inversion.

1.13.1 Finite size effects in Kwant simulations

We consider a QPC defined with a hard walled square well of width $w = 11a$ and length $L = 19a$. The discretization of the two dimensional Schrödinger equation yields a hopping amplitude $t = \frac{\hbar^2}{2M_e a^2}$, where a is the distance between two neighboring sites in the square lattice and M_e the effective mass of the electrons. The hopping energy t and the lattice spacing a are respectively, the natural units of energy and distance. The parameters a and t can be chosen to correspond to realistic situations. For GaAs heterostructures the electron effective mass is $M_e = 0.067$. Hence, if we take $a = 10nm$, we find the hopping energy $t = 5.69meV$. If the Fermi wavelength is an order of magnitude bigger than a the tight-binding model describes the continuous system with high accuracy.

The lateral boundaries of the wide region in Fig. 1.10 lead to finite size effects. To remove this artifact periodic boundary conditions could be adopted, as provided by the module "Wraparound" included in the latest Kwant release (see kwant-project.org).

In this work we attached side leads (Fig. 1.10) to allow for translational invariance in the transverse direction. Therefore, electrons entering the side leads are not scattered back. However, the corners situated at the edges relating between two adjacent leads will still have minor effects in the transport properties. In fact, electrons supposed to enter the leads can be reflected by these corners. However, the finite size artifacts can be totally eliminated, if one dimensional leads are attached at these corners in the direction perpendicular to the 2DEG as done in Ref. [33]. Furthermore, in the presence of a fluctuating disorder, the configuration of the latter can be chosen such that there is no current flow towards these corners.

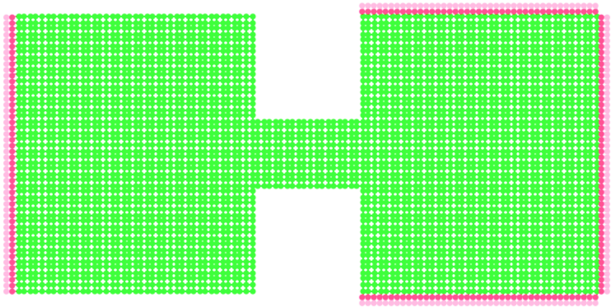

Figure 1.10: The tight binding lattice output by Kwant is shown. The width of the QPC is $w = 11a$ and its length is $L = 19a$. The red areas represent the transitionally invariant leads. Additional leads in the transverse direction are attached to the right wide region.

1.13.2 Model for long-range disorder

In order to take into account the disorder in the 2DEG, we use the method proposed by Thomas Ihn [Private communication]. We consider the disorder to be caused by the Coulomb potential of singly-ionized dopants in the doping plane, situated at the $\delta-$donor layer (see Fig. 1.1) at some distance s from the 2DEG. The distribution of the randomly placed donor atoms is given by

$$\mathcal{N}_d(\mathbf{r}, z) = \sum_{j=1}^{M} \delta(\mathbf{r} - \mathbf{r}_j)\delta(z - s), \tag{1.68}$$

where the $\mathbf{r}_j$ are drawn randomly from a two-dimensional uniform distribution defined within an area A, and M is the number of dopants. We split $\mathcal{N}_d$ into a smeared mean doping density $N_d = \frac{M}{A}$ and the fluctuating part of the density

$$C(\mathbf{r}) = \left[\sum_{j=1}^{M} \delta(\mathbf{r} - \mathbf{r}_j) - N_d\right] \delta(z - s) \tag{1.69}$$

responsible for the disorder potential in the 2DEG. In real-space, the bare fluctuating potential seen by the electrons in the 2DEG is

$$V(\mathbf{r}) = -\frac{e^2}{4\pi\epsilon\epsilon_0} \int \mathrm{d}\bar{\mathbf{r}} \frac{C(\bar{\mathbf{r}})}{\sqrt{(\mathbf{r} - \bar{\mathbf{r}})^2 + s^2}}, \tag{1.70}$$

which is a two-dimensional convolution of $C(\mathbf{r})$ with the Coulomb potential of a point charge. The quantity ϵ is the relative dielectric constant of the material. The Fourier transform of $V(\mathbf{r})$ is

$$V(\mathbf{q}) = -\frac{e^2}{2\epsilon\epsilon_0} C(\mathbf{q}) \frac{e^{-qs}}{q}, \tag{1.71}$$

Thomas-Fermi screening will reduce the potential fluctuations in the plane according to the dielectric function

$$\epsilon_{TF}(\mathbf{q}) = 1 + \frac{2}{q a_B^*}, \tag{1.72}$$

where a_B^* is the effective Bohr-radius of the material. The screening potential is given by

$$V(\mathbf{q}) = -\frac{e^2}{2\epsilon\epsilon_0} C(\mathbf{q}) \frac{e^{-qs}}{\epsilon_{TF} q} = -\frac{e^2}{2\epsilon\epsilon_0} C(\mathbf{q}) \frac{e^{-qs}}{q + q_{TF}}, \tag{1.73}$$

where $q_{TF} = 2/a_B^*$ is the Thomas-Fermi screening momentum, which does not depend on electron density in case of 2DEGs.The potential in real space can be obtained from an inverse Fourier transform of $V(\mathbf{q})$, it is given by

$$V(\mathbf{r}) = \int \frac{\mathrm{d}^2\mathbf{q}}{(2\pi)^2} V(\mathbf{q}) e^{-i\mathbf{qr}}. \tag{1.74}$$

In a tight-binding network of length L, width W and grid spacing a we have [Thomas Ihn, private communication]

$$V(x, y) = -\frac{\Delta q_x \Delta q_y}{\pi} \sum_{j(\neq 0)} \frac{e^{-q_j s}}{q_j + q_{TF}} C(\mathbf{q}_j) e^{-i\mathbf{q}_j\mathbf{r}}, \tag{1.75}$$

where $\Delta q_x = \frac{2\pi}{L}$ and $\Delta q_y = \frac{2\pi}{W}$ are the step widths of the corresponding discretized $\mathbf{q}-$space. The maximum $\mathbf{q}-$value we have to consider is

$$q_{max} = \frac{2\pi}{a} \tag{1.76}$$

in both directions. A particular realization of the fluctuating potential is obtained by drawing numbers α_j and β_j from a normal distribution with the variance $M/2$. The resulting distribution can be written as

$$C(\mathbf{q}_j) = c_j e^{i\phi_j}, \tag{1.77}$$

with random amplitudes

$$c_j = \sqrt{\alpha_j^2 + \beta_j^2} \tag{1.78}$$

and random phases

$$\phi_j = \arg(\alpha_\mathrm{j} + \mathrm{i}\beta_\mathrm{j}). \tag{1.79}$$

Given these random numbers, the potential is given by

$$V(x,y) = -\frac{\Delta q_x \Delta q_y}{\pi} \sum_{j(\neq 0)} \frac{e^{-q_j s}}{q_j + q_{TF}} c_j e^{-i(\mathbf{q}_j \mathbf{r} + \phi_j)}. \tag{1.80}$$

Making use of the symmetry property $C(-\mathbf{q}) = C^*(\mathbf{q})$ we can write

$$V(x,y) = -2\frac{\Delta q_x \Delta q_y}{\pi} \sum_{j(>0)} \frac{e^{-q_j s}}{q_j + q_{TF}} c_j e^{-i(\mathbf{q}_j \mathbf{r} + \phi_j)}. \tag{1.81}$$

Due to the exponential decay of the contributing terms with $q_j s$ one can limit the numerical efforts by neglecting the terms with large q_j. We took $3.5/s$ as a cut-off which leads to an reduction of the computational time by more than two orders of magnitude in practical cases.

To characterize the resulting disorder potential we introduce the transport mean free path l_T, which is the distance over which an initial electron momentum is randomized.

According to Fermi's Golden Rule, the life time τ of an initial state $|i\rangle$ scattered by the disorder potential $V(\mathbf{r})$ into a final state $|f\rangle$ is given by

$$\tau^{-1} = \frac{2\pi}{\hbar} |\langle f| V(\mathbf{r}) |i\rangle|^2 \rho, \tag{1.82}$$

where ρ is the 2-dimensional density of states.

Considering the initial and the final states as 2-dimensional plane waves

$$\langle \mathbf{r}| i\rangle = \frac{e^{i\mathbf{kr}}}{\sqrt{A}}, \tag{1.83}$$

and

$$\langle \mathbf{r}| f\rangle = \frac{e^{i\mathbf{k'r}}}{\sqrt{A}}, \tag{1.84}$$

the absolute square of the the matrix element in Eq. (1.82) reads

$$|\langle f| V(\mathbf{r}) |i\rangle|^2 = \frac{16\pi^2 E^*_{Ry} a^*_B}{A^2} \left| \frac{C(\mathbf{q}) e^{-qs}}{q + q_\mathrm{TF}} \right|^2, \tag{1.85}$$

where we have introduced the Rydberg energy defined by

$$\frac{e^2}{\epsilon\epsilon_0} = 8\pi E^*_{Ry} a^*_B, \tag{1.86}$$

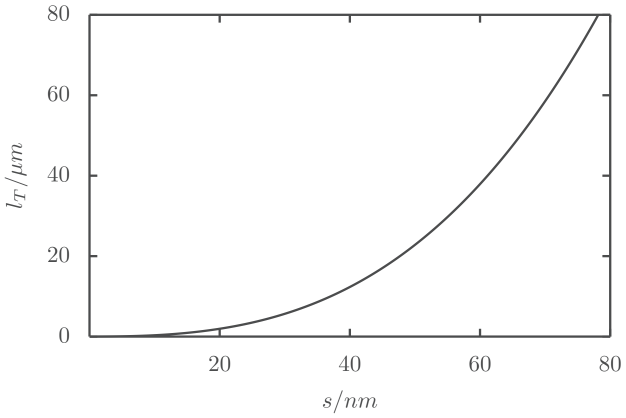

Figure 1.11: The dependence of the transport mean free path on s is shown. We take the effective Bohr radius as $a_B^* = 12nm$, a dopant density of $N_d = 4.5 \times 10^1 2cm^{-2}$ and $\varepsilon_\mathrm{F} = 16meV$.

and the momentum variable $\mathbf{q} = \mathbf{k} - \mathbf{k}'$. Therefore, the relaxation time can be obtained by taking the average of τ^{-1}.

To not take into account forward back-scattering processes, the average should be weighted by the factor $1 - \cos\theta$, with θ the collision angle between initial and final states. This yields,

$$l_T^{-1} = (\tau v_F)^{-1} = \frac{4\pi N_d E^*_\mathrm{Ry}}{\varepsilon_\mathrm{F} \lambda_F} \int_0^{2\pi} \mathrm{d}\theta (1 - \cos\theta) \frac{e^{-2q(\theta)s}}{(q(\theta) + q_\mathrm{TF})^2}, \tag{1.87}$$

with $q(\theta) = \sqrt{2(1 - \cos\theta)}k_F$, and v_F, k_F are respectively, the Fermi velocity and the Fermi wave-number.

The transport mean free path is determined by the two parameters of the disorder, the doping density N_d and the distance s between the doping layer and the 2DEG. Its value can be obtained by numerically evaluating the integral in Eq.(1.87).

In Fig. 1.11 the transport mean free path is plotted as a function of s at fixed density of donors $N_d = 4.5 \times 10^{12} cm^{-2}$, we observe that as the distance between the donor layer and the 2DEG increases, the transport mean free-path becomes longer. For $s = 60nm$ we find $l_T = 38\mu m$, which is a realistic value for the transport mean free path in high mobility 2DEGs.

In principle, to change the disorder strength we could modify N_d and/or s. But this will result in changing the disorder configuration too. Therefore, it is advantageous to introduce a factor γ to account for the disorder strength. It will be a pre-factor multiplying $V(\mathbf{r})$. Consequently, if l_T is the transport mean free path in the presence of the disorder potential V, then the transport mean free path corresponding to the potential γV is equal to l_T/γ^2, according to the above presented calculation.

Chapter 2

Introduction to Scanning gate microscopy

2.1 Overview

Scanning gate microscopy (SGM) is an innovative technique that has been developed in the group of R. Westervelt at Harvard University [34, 4] during the last decade of the twentieth century. In this technique, the conductance through a mesoscopic sample is measured while the tip of an atomic force microscope (AFM) is scanned above its surface.

The AFM tip acts as a movable gate which induces a potential that scatters the electrons, leading to a space modulation of the measured conductance. This spatial dimension added to the transport experiment is the most important ingredient of the SGM technique.

SGM is not the only technique that leads to such spatial resolution. The scanning tunneling microscopy (STM) [35], for instance, has the same property, and has been used to access the local density of states by measuring the transversal current through a given structure.

The STM technique is therefore useful when conducting surfaces are studied. However, if the region of interest is buried underneath some distance from the surface this technique fails.

SGM gives a hope to have space resolved quantum transport measurements where the probe tip is weakly invasive, such that information about the unperturbed transport properties of the nanostructure can be extracted.

Since the very early days of its development, the measured conductance change induced by the SGM tip has been interpreted in terms of the current flow in the considered nanostructures [4, 5].

Nevertheless, no complete view has been yet offered in order to fully understand the circumstances and regimes under which this interpretation holds. One of the most investigated nanostructures is the quantum point contact (QPC)[2, 36] defined in a two dimensional electron gas (2DEG).When the tip is raster-scanned over the surface of the system, electrons are backscattered to the QPC, giving rise to a conductance map that exhibits a branched pattern. In the case of a QPC opening into an unconstrained 2DEG these patterns have been interpreted as a signature of the electron flow in the disordered potential resulting from the ionized donor atoms [5, 37]. Thus, a link is presumed to exist between SGM measurements and local properties (local densities of states [LDOS] and current densities) of the unperturbed devices. Typically, the tip voltages used to study QPC setups operating in the regime of conductance quantization are strong enough to create a large depletion disk (much bigger than the Fermi wavelength) in the 2DEG underneath the tip. The connection with local properties has been argued to concern the classical turning point of the electron trajectories with the Fermi energy that leave the QPC and encounter the tip potential [38] .

In order to address this problem, the paradigmatic case of a QPC perturbed by a weak tip has been considered in the linear [11, 15] and non-linear [39] regimes (in source-drain bias voltage). In particular, in the regime of conductance quantization of clean 2DEGs, spatial and time-reversal symmetries have been shown to play a key role in establishing a correspondence of the SGM response with the LDOS and the current density on both sides of the QPC in the weakly invasive regime.

The SGM technique has also been used to study systems with a variety of electronic confinements, including open quantum dots [40, 41, 42, 43, 44, 45]and Aharonov-Bohm rings built in high-mobility semiconductor heterostructures [46, 47, 48, 6], as well as carbon nanotubes [49] and graphene-based microstructures [50, 51]. For systems with sufficient electronic confinement, charging effects are relevant, and for very small quantum dots a biased SGM tip mainly acts as a gate that modifies the number of electrons in the dot and affects the conductance via the Coulomb-blockade phenomenon [52, 53, 49, 54, 50].

For relatively large and open quantum dots, the charging effects are not crucial and, as in the case of QPC setups, the connection between the SGM measurements and local properties has been pursued. In these systems, qualitative similarity between conductance changes and LDOS has been noted whenever the LDOS exhibits some localized structure. For instance, minima of the SGM response appear where the LDOS vanishes [48, 6] . Furthermore, numerical simulations for rectangular resonant cavities [55] indicated that the conductance terms derived in Ref. [11] are correlated with the LDOS when the Fermi energy is close to a resonance with a cavity state. For one-dimensional systems, a perturbative approach has revealed that the conductance change in the presence of a delta-tip up to first-order in tip strength is related to the Hilbert transform of the LDOS [56, 48] .

It is important to note that electronic confinement is associated with a change in the interpretation of SGM maps with respect to the case of a QPC. Specifically tailored experiments have shown the need of such a change of interpretation when the QPC setup is modified by electronic confinement guiding the electron transport [8, 45]. The need of different interpretations for setups with and without electronic confinement can be traced, in the case of weakly invasive probes, to special features of conductance quantization characterizing QPCs in the absence of confinement, where the transmission channels are either completely open or closed [11].

The issue of whether the transmission channels are completely open (and otherwise completely closed), i.e. the perfect transmission case, turns out to play a crucial role in the interpretation of measurements and their relationships to local properties. It has been shown that in the case of perfect transmission, the second order conductance change in tip strength is the first non-vanishing term in a perturbation series [11] and it is proportional to the square of the LDOS [15]. However, as we will see in chapter 6, the analytic relationship between conductance changes and local properties becomes more complicated for imperfect transmission.

2.2 Concepts of local partial density of states

In a paper of 1993, Büttiker, Prêtre and Thomas introduced the concept of local partial densities of states, or partial local density of states (PLDOS) as we prefer to call it here. In this paper such a quantity appeared as a mathematical object naturally arising when the equilibrium admittance matrix is calculated [56].

Three years later, in a paper entitled *Partial densities of states, scattering matrices and Green function*, Gasparian, Christen and Büttiker discussed the relevance of PLDOS as a physically meaningful quantity. The latter was expressed in terms of the functional derivatives of the scattering matrix with respect to the confining electrostatic potential as well as the Green function of the underlying system.

In a one dimensional picture, these authors showed that the PLDOS is related to the imaginary part of the diagonal Green function. A further more general study has considered the PLDOS in a quasi one-dimensional scattering problem [57].

The PLDOS can be seen as a decomposition of the total local density of states (LDOS). This decomposition is related to the fact that the scattering matrix is itself constructed from reflection and transmission submatrices. The definition of PLDOS is based on both a preselection and a postselection of carriers. This means that the asymptotic region from which the carriers come from or the region into which they are scattered have to be considered.

In the same framework the authors have pointed out that the PLDOS involving only the carriers reflected to the same region from which they are originally emitted does not have physical meaning of density, since they even do reach negative values. Accordingly, they have called the PLDOS generated by the carriers incident from a given asymptotic region regardless into which region these carriers are scattered the injectivity of the emitting asymptotic region. So this is a preselection of carriers indeed. In this sense the PLDOS for electrons incoming from lead l with energy ε can be defined as

$$\rho_{l\varepsilon}(\mathbf{r}) = 2\pi \sum_{a=1}^{N} |\psi_{l,\varepsilon,a}(\mathbf{r})|^2 \,, \tag{2.1}$$

where $\psi_{l,\varepsilon,a}(\mathbf{r})$ is the scattering wave function coming from the a^{th} mode of lead l at energy ε.

A postselection of carriers has also led to another type of PLDOS they have called emmisivity. It basically represents the PLDOS generated by carriers scattered to a given lead regardless of the region they are emitted from. But this quantity will not be considered here. Therefore when we talk about PLDOS in the framework of this thesis we are referring to the injectivity of a given lead in the sense of Ref. [56].

Furthermore, the PLDOS has been shown to be related to some characteristic times in quantum dynamics [58, 59]. Namely, the dwell time which is the time a density of carriers would remain in a given interval of space. While the results in [58, 59] were specific for 1D systems, Innacone [60] demonstrated that for a 2D system the LDOS can be also expressed as a sum of all dwell times of the various incoming channels .

2.2.1 SGM in Quantum point contacts

Among the most investigated nanostructures using SGM are QPCs described in the previous chapter. We have seen that the conductance of such a system can assume well-defined plateaus. If the QPC is tuned to a quantized value of conductance, the effect of the tip is to reduce the conductance, depending on its position yielding different space resolved properties, among them interference fringes and branching behavior.

We study whether the measured conductance changes have some simple or complex relationship with the local properties of the traveling electrons via different interference mechanisms [5, 38].

The question we should ask is, can we quantitatively extract some physically relevant, and meaningful quantities such as local current densities, local density of states or LDOS from an SGM measurement?

In Fig.2.1 the SGM response measured at temperature $T = 1.7\mathrm{K}$ is shown for the first three plateaus ($g = 1$, 2 and 3). The Fermi energy of the electrons is $\varepsilon_{\mathrm{F}} = 16\mathrm{meV}$ corresponding to a Fermi wavelength of $\lambda_F = 37\mathrm{nm}$.

Besides the interference fringes spaced by half the electron Fermi wavelength shown in Fig.2.1 evidencing the fact that the imaged features are of coherent origin, the branching behavior reveals quite rich information related to the potential landscape in which electrons move that is defined by the ionized donor atoms located at some distance from the 2DEG.

The branches in Fig. 2.2 are understood to be due to the fluctuating potential induced by the donor atoms situated few tens of nanometers from the 2DEG [5]. The same interference fringes observed in Fig.2.1 are visible along the branches.

In [4] a qualitative comparison between the measured SGM and numerically calculated PLDOS has been made see (Fig. 2.3). The suppression of the interference fringes presented above is due to the fact that the measurements are done at high source drain voltage, fifteen times bigger than the one applied in the data of Fig. 2.1.

One observes that the angular propagation and the number of lobes of the electron flow are qualitatively the same for both, SGM and PLDOS.

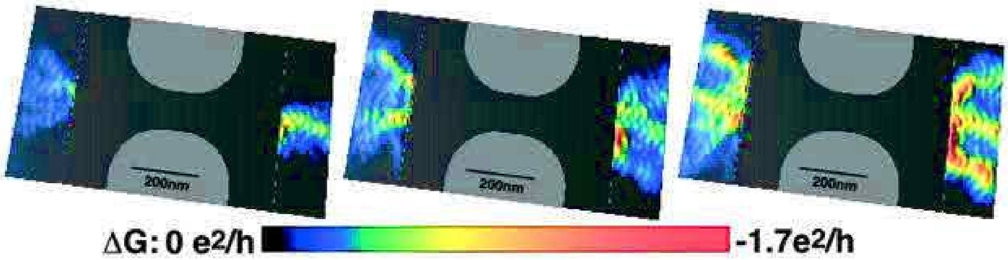

Figure 2.1: SGM measurement in the neighborhood of a QPC (depicted in gray) for the first three plateaus of conductance ordered from left to right. The figure is adapted from [4].

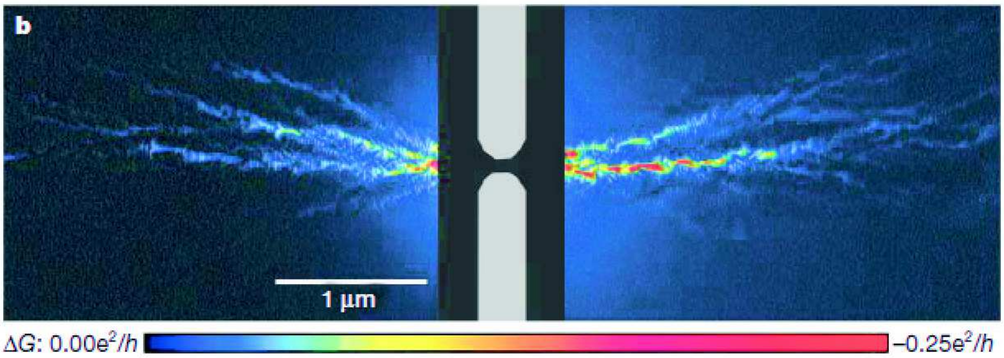

Figure 2.2: SGM measurement of transport through a QPC (tuned to the first plateau of conductance) with a branching pattern is shown. Fringes similar to those observed in 2.1 can be seen along the branches. The figure is taken from [5].

2.2.2 SGM in quantum rings

Another system that has been widely studied, both theoretically and experimentally, is the quantum ring [48, 6] (see Fig.2.4). Since the boundaries of the studied geometry play an important role in the scattering process, the wave functions coming from both sides of the ring have to be taken into consideration. In this situation the total LDOS has been shown to play a role in the interpretation of the measured conductance [48].

Based on a one-dimensional model the authors of Ref. [48] found that the first-order conductance correction due to a local tip is proportional to the Kramers-Kronig partner of the LDOS. In other terms, they found that the SGM is directly related to the Hilbert transform of the LDOS.

Although they did not evaluate the Kramers-Kronig partner of the calculated LDOS to be compared with the SGM conductance, they have qualitatively compared between the direct quantities (i.e. SGM and LDOS) which are apparently similar as we can see from Fig.2.4.

Furthermore, experimental and numerical results [61, 7] have evidenced the presence of recurrent quantum scars (concentration of wave functions along classical periodic orbits) [62] in the SGM response of a mesoscopic graphene ring.

In the graphene ring [61] the period of the recurrent features is found to be proportional to the Fermi energy, in contrast to what has been reported for conventional semiconductor nanostructures where the period of the recurrent scars has been found to be proportional to the square root of the Fermi energy [63, 64].

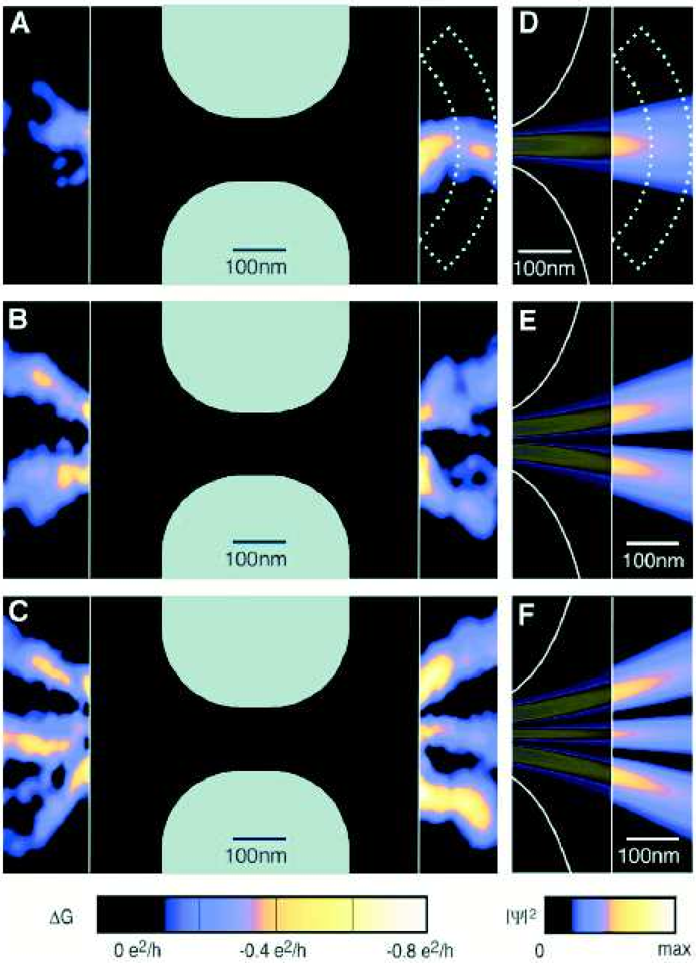

Figure 2.3: In the left column the measured SGM responses at high voltage for the first three plateaus are shown. The corresponding calculated PLDOS are shown in the right column. Figure from Ref.[4].

This difference has been understood as a signature of the energy dispersions which are not the same for normal semiconductors and Dirac materials.

In panels a and b of Fig.2.5 the SGM response is measured at two different energies separated by a period of recurrence of the star-like shape [7].

Although the interpretation of the observed shapes as quantum scars has no strong theoretical support, the presence of such recurrent features in the computed LDOS (see the right panel of 2.5) with the same period of appearance as for the SGM maps suggests a link between the SGM conductance change and the LDOS.

A more technical analysis about the SGM-LDOS correspondence will be

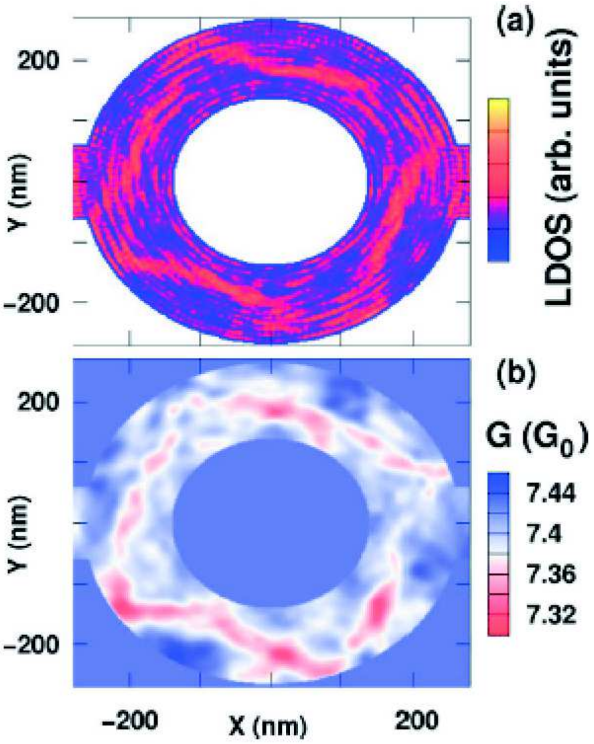

Figure 2.4: The calculated LDOS in a quantum ring is shown in the top figure and the conductance through the ring in the presence of a weakly invasive tip is presented in the bottom figure, the qualitative similarity between the two quantities is observed . The figure is taken from [6].

given in chapter 7.

2.3 SGM imaging in confined geometries

Recently R. Steinacher and coauthors from the group of Klaus Ensslin and Thomas Ihn at the ETH Zürich have carried out an experiment where the branches observed in the SGM measurement are guided by confining gates [8]. In this experiment, the electrons transmitted through the QPC are injected into a channel of width $w = 1\mu m$ defined by lateral Schottky gates. In Fig.2.6 the branches behind the QPC are shown. Whereas the lateral gates are set to zero voltage, the branches are found to be confined within the channel through which the electrons are injected from the neighboring QPC (situated in the center bottom of each of the maps (a) and (b) of Fig.2.6). In region I and III outside of the central channel (II) the SGM pattern is smooth,

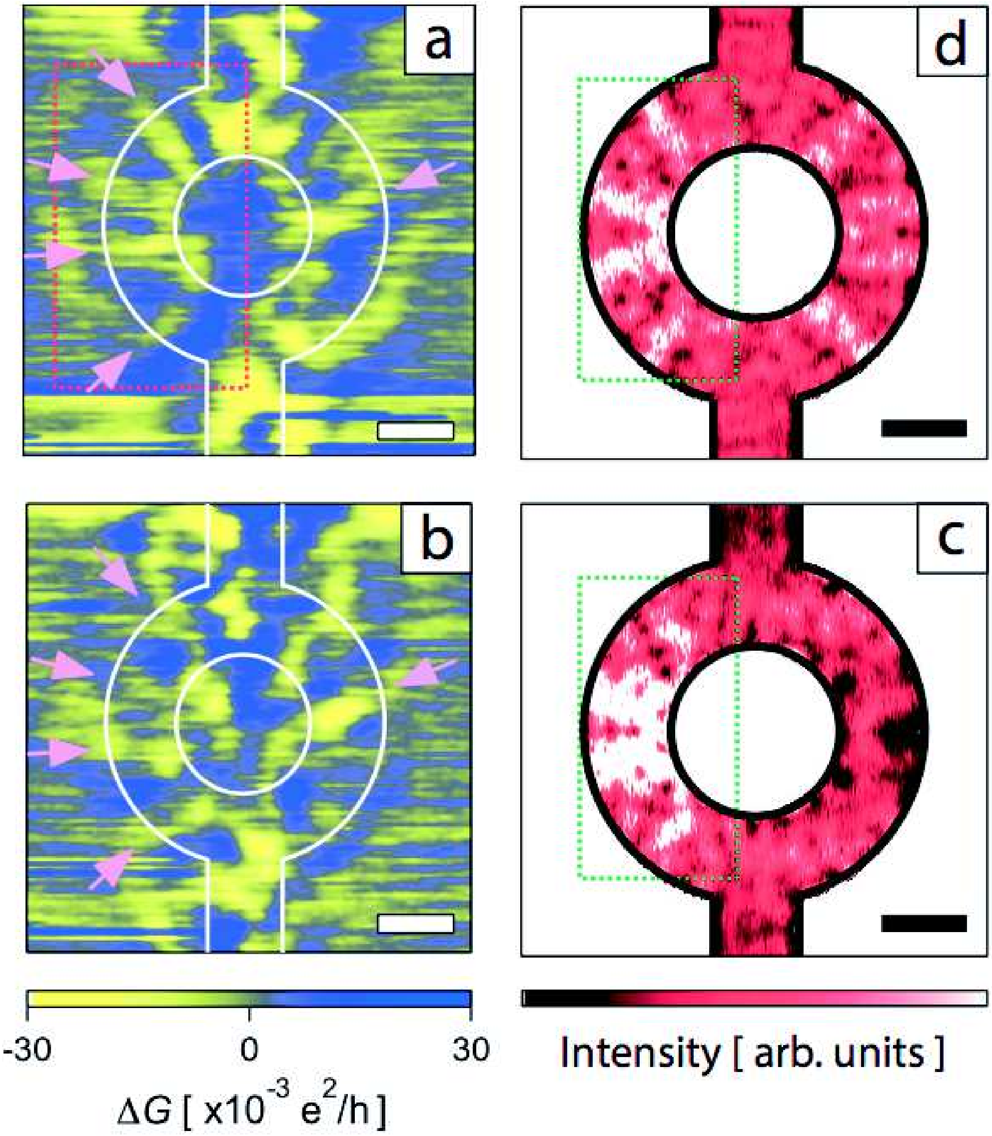

Figure 2.5: Experimental SGM images are presented at two different Fermi energies in a and b. In d and c the LDOS is calculated for two different energies. The figure is taken from [7].

meaning that the electrons have no possibility to be reflected back to the QPC. However in the central region (II) they do not have any possibility to skip out of the channel gates. This effect has been interpreted as a result of a shallow potential barrier existing below the unbiased gates [8, 9].

2.4 SGM in the weakly invasive regime

In Ref.[11] and [15] the authors have presented an analytic theory in the perturbative regime where the effect of the AFM tip on the local properties can be considered as weak. In this regime, the SGM response in first and second order in the tip strength have been analytically obtained. The corrections are given by matrix elements of the tip-induced potential with scattering wave-functions.

Since the invasiveness of the tip is usually necessary for observing the SGM signal with a sufficient signal-to-noise ratio, performing an SGM measurement in the regime where the theory applies has remained as a difficult task, at least in the case of QPCs opening to unconstrained 2DEG. In Ref. [9] and in a very recent paper [65], an interesting experimental setup (see Fig. 2.7) has been proposed to approach as much as possible the weakly invasive regime.

In order to enhance the observed SGM signal, a circular reflector has been put in front of the QPC. This enhances the scattering wave-functions within the region between the QPC and the reflector, allowing by consequence for a significant SGM signal even when applying smaller tip voltages. As shown in Fig.2.7 the SGM response could be observed at relatively small tip voltages provided that the reflector gate is biased.

2.5 Signatures of spin-orbit coupling in SGM response

In Ref. [10], the authors have numerically investigated the signatures of spin-orbit coupling (SOC) in the SGM response of a QPC opening to a disorder-free 2DEGs.

In their work the authors have considered the Rashba type SOC, which turns out to be important in InGaAs hetero-structures.

The Rashba interaction reads

$$H_R = \alpha(\sigma_x k_y - \sigma_y k_x), \tag{2.2}$$

where α is the strength of the SO interaction, $\sigma_{x(y)}$ is the $x(y)$ component of the Pauli matrix σ, and $k_{x(y)}$ is the momentum projection along the $x(y)$ direction. The QPC was modeled by a smooth potential

$$V(x,y) = \frac{m^*\omega^2 x^2}{2}\exp[-((y - Y_{qpc})/\sqrt{2}w)^2], \tag{2.3}$$

where Y_{qpc} is the position of the QPC along the y direction, $w = 100nm$ controls its length, and $\hbar\omega$ describes its parabolic confinement in the transverse direction (the x direction).

In Fig. 2.8, the SGM response has been calculated for the three first plateaus in the absence of SOC (upper row) and in the presence of SOC (lower row). In the presence of SOC, additional features between the usual lobes appear.

The additional lobes have been explained [10] to be due to particular values of the transfer probability, resulting from the transformation of the kinetic energies between anti-crossing modes, due to the spin mixing caused by the last term of the Rashba SOC (2.2).

2.6 Motivation of this thesis

According to the Heisenberg uncertainty principle we cannot measure at the same moment the position and the velocity of a quantum mover. However, the quantum "particles" are described by some wave-functions whose dynamics is governed by a deterministic equation (the Schrödinger equation) in the sense that the latter allows us to predict the wave-functions at each later time provided its knowledge at a given initial moment.

Interestingly, the SGM technique provides position-dependent conductance data and one can ask the question whether those can be used to access some quantities directly related to the electronic local properties by experimental measurements ?

Although the first experimental studies have claimed imaging coherent electron flow in mesoscopic devices, a quantitative study of the link between the measured SGM conductance and the local electronic properties is missing.

In this PhD thesis a theoretical effort is devoted to develop the necessary tools for a quantitative extraction of the local electronic properties from SGM measurements in realistic mesoscopic systems.

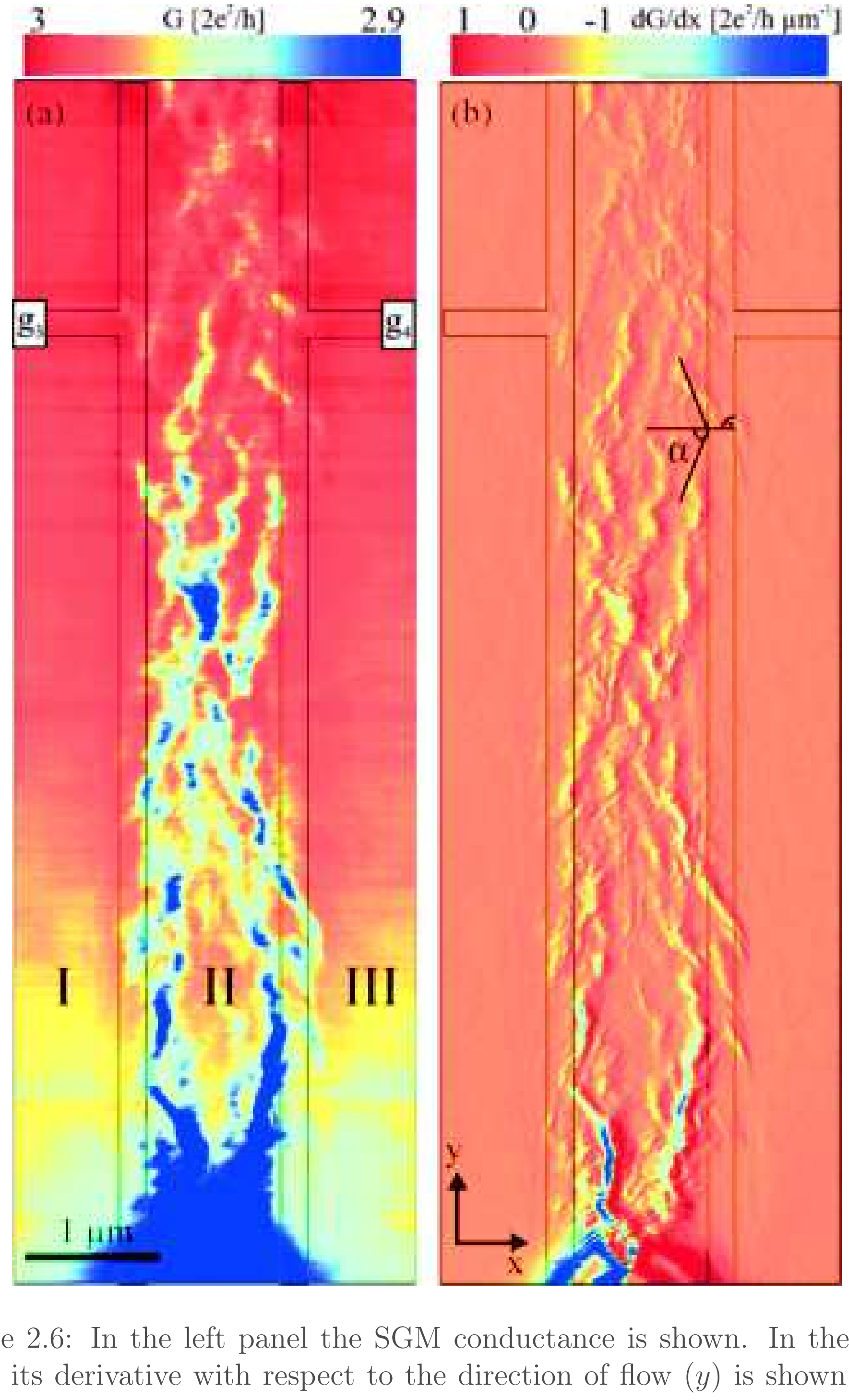

Figure 2.6: In the left panel the SGM conductance is shown. In the right panel its derivative with respect to the direction of flow (y) is shown. The QPC is at the bottom of the figures. The thin line indicates the position of the guiding gates. The figure is taken from [8].

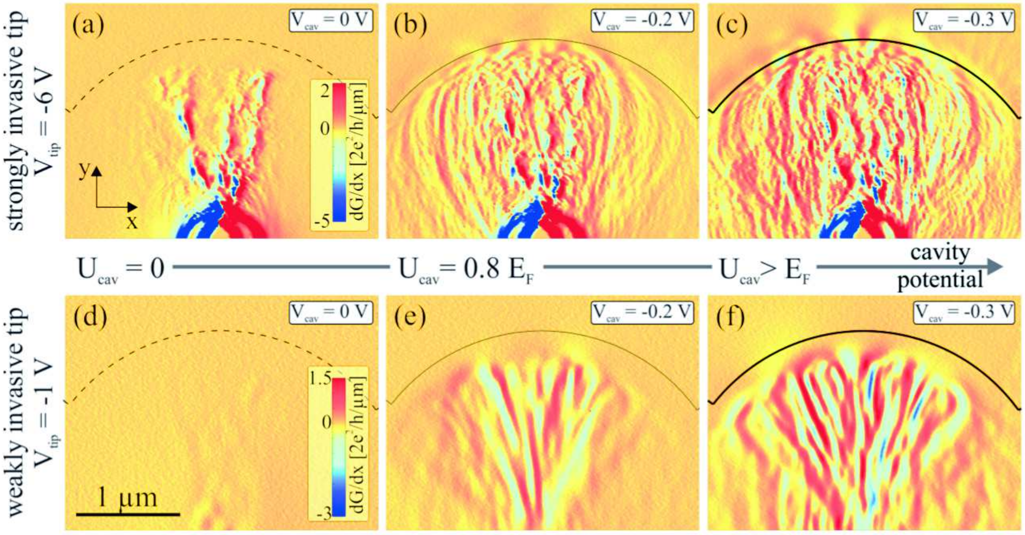

Figure 2.7: Spatial derivative of the SGM conductance measured throughout a QPC positioned some distances from the center bottom of each figure as a function of tip position is shown, at different tip voltages and for different reflector gate (the circular arc in front of the QPC) bias [9]. One observes that for a fixed tip voltage, the SGM resolution is enhanced just by applying a bias to the reflector. The QPC is tuned to the third plateau of conductance.

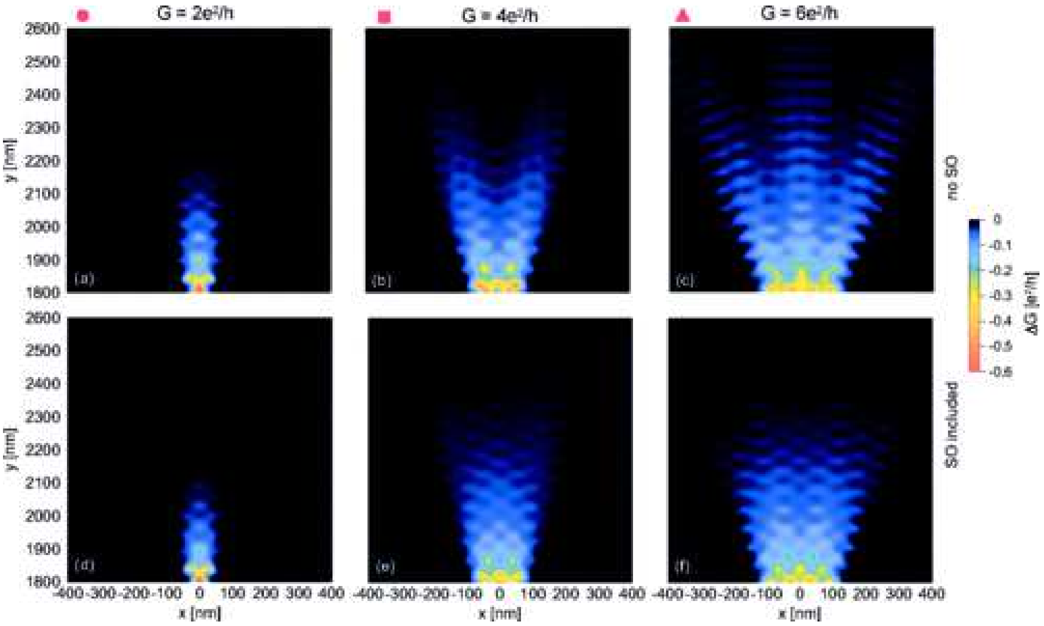

Figure 2.8: Simulation of SGM images for the three first plateaus. The QPC model of (2.3) is used. In the upper (lower) row of data, the SGM conductance without (with) SOC is shown. The figure is taken from [10].

Chapter 3

Analytical formulation of the SGM response (perturbation theory)

In this chapter we want to present the lowest order terms of the perturbation theory for the conductance corrections due to a local potential, following Ref.[11]. The calculated conductance corrections will be crucial for the next chapters.

3.1 First order correction

Let us consider a quantum scatterer attached to two semi infinite leads as the one sketched in Fig. 1.4 in the previous chapter. The asymptotic form of the unperturbed scattering wave-functions can be written in terms of the matrix element of the scattering matrix and the transverse wave-functions of the leads as well as the longitudinal one :

$$
\begin{aligned}
\Psi^{(0)}_{1,\varepsilon,a}(\mathbf{r}) &= \begin{cases} \varphi^{(-)}_{1\varepsilon a}(\mathbf{r}) + \sum_{b=1}^{N} r_{ba}\, \varphi^{(+)}_{1\varepsilon a}(\mathbf{r}), & x<0 \\ \sum_{b=1}^{N} t_{ba}\, \varphi^{(+)}_{2\varepsilon b}(\mathbf{r}), & x>0 \end{cases} \\
\Psi^{(0)}_{2,\varepsilon,a}(\mathbf{r}) &= \begin{cases} \sum_{b=1}^{N} t'_{ba}\, \varphi^{(+)}_{1\varepsilon a}(\mathbf{r}), & x<0 \\ \varphi^{(-)}_{2\varepsilon a}(\mathbf{r}) + \sum_{b=1}^{N} r'_{ba}\, \varphi^{(+)}_{2\varepsilon b}(\mathbf{r}), & x>0 \end{cases}
\end{aligned}
\tag{3.1}
$$

The matrices r, r', t and t' are submatrices of the scattering matrix S given by (1.21). The lead wave-functions $\varphi^{(s)}_{l\varepsilon a}(\mathbf{r})$ have been defined in Sec. 1.7.

In general, the n^{th} order correction to the scattering wave-function is obtained from (1.14) as follows

$$\Psi^{(n)}_{l,\varepsilon,a}(\mathbf{r}) = \int \mathrm{d}\bar{\mathbf{r}}\ \mathcal{G}^{(0)}(\mathbf{r},\bar{\mathbf{r}},\varepsilon)V_{\mathrm{T}}(\bar{\mathbf{r}})\Psi^{(n-1)}_{l,\varepsilon,a}(\mathbf{r}')\ , \tag{3.2}$$

where $V_{\mathrm{T}}(\bar{\mathbf{r}})$ is the potential induced by the tip. Up to linear order in the tip potential the correction to the scattering wave-function in the presence of the tip is obtained by taking $n = 1$ in (3.2), which gives

$$\Psi^{(1)}_{l,\varepsilon,a}(\mathbf{r}) = \int \mathrm{d}\bar{\mathbf{r}}\ \mathcal{G}^{(0)}(\mathbf{r},\bar{\mathbf{r}},\varepsilon)V_{\mathrm{T}}(\bar{\mathbf{r}})\Psi^{(0)}_{l,\varepsilon,a}(\bar{\mathbf{r}})\ . \tag{3.3}$$

The first-order correction to the current density associated with such a state specified by the corresponding lead index l, energy ε and mode number a, is given by

$$\delta^{(1)}J_{l\varepsilon a} = \frac{e\hbar}{M_e}\mathrm{Im}(\Psi^{(0)*}_{l\varepsilon a}(\mathbf{r})\partial_x\Psi^{(1)}_{l\varepsilon a}(\mathbf{r}) - \Psi^{(1)}_{l\varepsilon a}(\mathbf{r})\partial_x\Psi^{(0)*}_{l\varepsilon a}(\mathbf{r})). \tag{3.4}$$

Substituting $\Psi^{(1)}_{l\varepsilon a}$ by its expression (11.1) in Eq. (11.2), the current correction up to first order in V_{T} reads

$$\delta^{(1)}J_{l\varepsilon a}(\mathbf{r}) = 2\sum_{\bar{l}=1}^{2}\mathrm{Re}\left\{\int_{\varepsilon_1^{(\mathrm{t})}}^{\infty}\frac{\mathrm{d}\bar{\varepsilon}}{\varepsilon^{+}-\bar{\varepsilon}}\ \sum_{\bar{a}=1}^{\bar{N}}\left[j(\mathbf{r})\right]^{l,\bar{l}}_{a\bar{a}}(\varepsilon,\bar{\varepsilon})\ \left[V_{\mathrm{T}}\right]^{\bar{l},l}_{\bar{a}a}(\bar{\varepsilon},\varepsilon)\right\}\ , \tag{3.5}$$

where

$$\left[j(\mathbf{r})\right]^{l,\bar{l}}_{a\bar{a}}(\varepsilon,\bar{\varepsilon}) = \frac{e\hbar}{2iM_{\mathrm{e}}}\left[\Psi^{(0)*}_{l,\varepsilon,a}(\mathbf{r})\ \partial_x\Psi^{(0)}_{\bar{l},\bar{\varepsilon},\bar{a}}(\mathbf{r}) - \Psi^{(0)}_{\bar{l},\bar{\varepsilon},\bar{a}}(\mathbf{r})\ \partial_x\Psi^{(0)*}_{l,\varepsilon,a}(\mathbf{r})\right], \tag{3.6}$$

is the longitudinal current density matrix element after integration over the transverse direction, and

$$\left[V_{\mathrm{T}}\right]^{\bar{l},l}_{\bar{a}a}(\bar{\varepsilon},\varepsilon) = \int \Psi^{(0)*}_{\bar{l},\bar{\varepsilon},\bar{a}}(\bar{\mathbf{r}})V_{\mathrm{T}}(\bar{\mathbf{r}})\Psi^{(0)}_{l,\varepsilon,a}(\bar{\mathbf{r}})\mathrm{d}\bar{\mathbf{r}}, \tag{3.7}$$

the matrix element of the tip potential between two scattering wave-functions.

If we are interested in the current coming from the left to the right we shall take $l = 1$.

$$\left[j(\mathbf{r})\right]^{11}_{\bar{a}a}(\varepsilon,\bar{\varepsilon}) \quad = \quad \frac{e}{2h}\sum_{b=1}^{\hat{N}}\left(\sqrt{\frac{\bar{k}_b}{k_b}} + \sqrt{\frac{k_b}{\bar{k}_b}}\right)t^{*}_{ba}\bar{t}_{b\bar{a}}\exp\left[i(\bar{k}_b - k_b)x\right] \tag{3.8}$$

$$\begin{aligned}[j(\mathbf{r})]^{12}_{\bar{a}a}(\varepsilon,\bar{\varepsilon}) &= \frac{e}{2h}\left(\sqrt{\frac{k_{\bar{a}}}{\bar{k}_{\bar{a}}}}-\sqrt{\frac{\bar{k}_{\bar{a}}}{k_{\bar{a}}}}\right)t^*_{\bar{a}a}\exp\left[-i(\bar{k}_{\bar{a}}+k_{\bar{a}})x\right] \\ &+ \frac{e}{2h}\sum_{b=1}^{\hat{N}}\left(\sqrt{\frac{\bar{k}_b}{k_b}}+\sqrt{\frac{k_b}{\bar{k}_b}}\right)t^*_{ba}\bar{r}'_{b\bar{a}}\exp\left[i(\bar{k}_b-k_b)x\right]. \quad (3.9)\end{aligned}$$

While the matrix t is taken at the energy ε, the matrices $\bar{t}$ and $\bar{r}'$ are evaluated at the energy $\bar{\varepsilon}$. The summations in (3.9) is up to $\hat{N} = min(N(\varepsilon), N(\bar{\varepsilon}))$.

According to Appendix C, the first term of $[j(\mathbf{r})]^{12}_{\bar{a}a}(\varepsilon,\bar{\varepsilon})$ plugged in (3.5) leads to a vanishing energy integral. Therefore, only $[j(\mathbf{r})]^{11}_{\bar{a}a}(\varepsilon,\bar{\varepsilon})$ and the second term of $[j(\mathbf{r})]^{12}_{\bar{a}a}(\varepsilon,\bar{\varepsilon})$ contribute to $\delta^{(1)}J_{1\varepsilon a}(\mathbf{r})$.

Using the results of Appendix C.1 we find that the current resulting from a given mode a in lead 1 at energy ε in first-order in the tip potential is

$$I^{(1)}_{1,\varepsilon,a} = \frac{e}{\hbar}\,\mathrm{Im}\left\{t^\dagger t\;\mathcal{V}^{11} + t^\dagger r'\;\mathcal{V}^{21}\right\}_{aa}, \tag{3.10}$$

where $\mathcal{V}^{l\bar{l}}_{a\bar{a}} = [V_{\mathrm{T}}]^{l\bar{l}}_{a\bar{a}}(\varepsilon,\varepsilon)$. Summing over all the modes we obtain the total current as

$$I^{(1)}_{1,\varepsilon} = \frac{e}{\hbar}\,\mathrm{Im}(\mathrm{Tr}\left\{t^\dagger t\;\mathcal{V}^{11} + t^\dagger r'\;\mathcal{V}^{21}\right\}). \tag{3.11}$$

In the linear response regime the zero temperature conductance is obtained by differentiating the total current with respect to the applied voltage, that is

$$G^{(1)} = \frac{2e}{\Delta\mu}(\Delta\mu I^{(1)}_{1,\varepsilon_{\mathrm{F}}}), \tag{3.12}$$

with $\Delta\mu$ the chemical potential difference between the two probes. The $\Delta\mu$ factor in the numerator results from the fact that at zero temperature only the Fermi energy current contributes to the transport and therefore the integration between the two chemical potentials reduces to a multiplication by $\Delta\mu$. This leads to the dimensionless conductance (in units of $\frac{2e^2}{h}$) [15, 11]

$$g^{(1)} = 4\pi\mathrm{Im}\left\{\mathrm{Tr}\left[t^\dagger t\;\mathcal{V}^{11} + t^\dagger r'\;\mathcal{V}^{21}\right]\right\}. \tag{3.13}$$

Since the first term of 3.13 is real $g^{(1)}$ simplifies to [11, 15]

$$\boxed{g^{(1)} = 4\pi\mathrm{Im}\left\{\mathrm{Tr}\left[t^\dagger r'\;\mathcal{V}^{21}\right]\right\}} \tag{3.14}$$

3.2 Second order correction

The obtained first order correction (11.9) is applicable to any open system. In the case of a quantum point contact where the conductance is quantized, this linear contribution vanishes on a conductance plateau ($r' = 0$). Therefore, the second order conductance correction has been also calculated [11, 15] .

The current density carried by the second order scattering wave-function from (3.2) can be separated into two contributions

$$\delta^{(2)} J^{(\alpha)}_{l\varepsilon a} = \frac{e\hbar}{M_e} \mathrm{Im}(\Psi^{(0)*}_{l\varepsilon a}(\mathbf{r})\partial_x \Psi^{(2)}_{l\varepsilon a}(\mathbf{r}) - \Psi^{(2)}_{l\varepsilon a}(\mathbf{r})\partial_x \Psi^{(0)*}_{l\varepsilon a}(\mathbf{r})) \tag{3.15}$$

and

$$\delta^{(2)} J^{(\beta)}_{l\varepsilon a} = \frac{e\hbar}{M_e} \mathrm{Im}(\Psi^{(1)*}_{l\varepsilon a}(\mathbf{r})\partial_x \Psi^{(1)}_{l\varepsilon a}(\mathbf{r})). \tag{3.16}$$

Replacing the second order scattering wave-functions by their expressions from (3.2) (with $n = 2$) in (3.15), the contribution $\delta^{(2)} J^{(\alpha)}_{1\varepsilon a}$ can be written as

$$\delta^{(2)} J^{(\alpha)}_{1\varepsilon a} = 2 \sum_{\bar{l},\bar{\bar{l}}=1}^{2} \mathrm{Re} \left\{ \int_{\varepsilon_1^{(\mathrm{t})}}^{\infty} \frac{\mathrm{d}\bar{\varepsilon}}{\varepsilon^{+} - \bar{\varepsilon}} \int_{\varepsilon_1^{(\mathrm{t})}}^{\infty} \frac{\mathrm{d}\bar{\bar{\varepsilon}}}{\varepsilon^{+} - \bar{\bar{\varepsilon}}} \sum_{\bar{a},\bar{\bar{a}}} [j(\mathbf{r})]^{1\bar{l}}_{a\bar{a}} (\varepsilon, \bar{\varepsilon}) \; [V_{\mathrm{T}}]^{\bar{l},\bar{\bar{l}}}_{\bar{a}\bar{\bar{a}}} (\bar{\varepsilon}, \bar{\bar{\varepsilon}}) \, [V_{\mathrm{T}}]^{\bar{\bar{l}}1}_{\bar{\bar{a}}a} (\bar{\bar{\varepsilon}}, \bar{\varepsilon}) \right\}. \tag{3.17}$$

To benefit from the results of the above calculation of the first-order correction, we write $\delta^{(2)} J^{(\alpha)}_{1\varepsilon a}$ as

$$\delta^{(2)} J^{(\alpha)}_{1\varepsilon a} = 2 \sum_{\bar{l}=1}^{2} \mathrm{Re} \left\{ \int_{\varepsilon_1^{(\mathrm{t})}}^{\infty} \frac{\mathrm{d}\bar{\varepsilon}}{\varepsilon^{+} - \bar{\varepsilon}} \sum_{\bar{a}} [j(\mathbf{r})]^{1\bar{l}}_{a\bar{a}} (\varepsilon, \bar{\varepsilon}) \; [W]^{\bar{l}1}_{\bar{a}a} (\bar{\varepsilon}, \varepsilon) \right\}, \tag{3.18}$$

where

$$[W]^{\bar{l}1}_{\bar{a}a} (\bar{\varepsilon}, \varepsilon) = \sum_{\bar{\bar{l}}=1}^{2} \int_{\varepsilon_1^{(\mathrm{t})}}^{\infty} \frac{\mathrm{d}\bar{\bar{\varepsilon}}}{\varepsilon^{+} - \bar{\bar{\varepsilon}}} \sum_{\bar{\bar{a}}} [V_{\mathrm{T}}]^{\bar{l},\bar{\bar{l}}}_{\bar{a}\bar{\bar{a}}} (\bar{\varepsilon}, \bar{\bar{\varepsilon}}) \, [V_{\mathrm{T}}]^{\bar{\bar{l}}1}_{\bar{\bar{a}}a} (\bar{\bar{\varepsilon}}, \bar{\varepsilon}).$$

Noticing that W plays the same role of V_T in Eq. (3.5), the conductance correction resulting from $\delta^{(2)} J^{(\alpha)}_{1\varepsilon a}$, after summation over a can be straightforwardly deduced from (3.13) as

$$\boxed{g^{(2)\alpha} = 4\pi v_{\mathrm{T}} \mathrm{Im} \left\{ \mathrm{Tr} \left[t^{\dagger} t \, \mathcal{W}^{11} + t^{\dagger} r' \, \mathcal{W}^{21} \right] \right\}} \tag{3.19}$$

with $\mathcal{W}^{l\bar{l}}_{a\bar{a}} = [W]^{l\bar{l}}_{a\bar{a}} (\varepsilon, \varepsilon)$.

Using the Sokhotsky's formula ([66], Sec.5.7), $\mathcal{W}$ can be written as

$$\mathcal{W}^{l\bar{l}}_{a\bar{a}} = -i\pi \sum_{\bar{\bar{l}}} \sum_{\bar{\bar{a}}} \left[V_{\mathrm{T}}\right]^{\bar{l},\bar{\bar{l}}}_{\bar{a}\bar{\bar{a}}} (\varepsilon, \bar{\bar{\varepsilon}}) \left[V_{\mathrm{T}}\right]^{\bar{\bar{l}}1}_{\bar{\bar{a}}a} (\bar{\bar{\varepsilon}}, \varepsilon) + \mathcal{P}\{\mathcal{W}^{l\bar{l}}_{a\bar{a}}\}, \tag{3.20}$$

and the $\alpha-$ like term of the second-order formula provided by [11, 15, 67] is straightforwardly obtained. Furthermore, if we assume that the tip is of the form

$$V_{\mathrm{T}}(\mathbf{r}) = v_{\mathrm{T}}\delta(\mathbf{r} - \mathbf{r}_{\mathrm{T}}), \tag{3.21}$$

$\mathbf{r}_{\mathrm{T}}$ being the position of the tip and v_{T} its strength, the following relation

$$\left[V_{\mathrm{T}}\right]^{\bar{l},\bar{\bar{l}}}_{\bar{a}\bar{\bar{a}}} (\bar{\varepsilon}, \bar{\bar{\varepsilon}}) \left[V_{\mathrm{T}}\right]^{\bar{\bar{l}}1}_{\bar{\bar{a}}a} (\bar{\bar{\varepsilon}}, \bar{\varepsilon}) = \left[V_{\mathrm{T}}\right]^{\bar{l}1}_{\bar{a}a} (\bar{\varepsilon}, \varepsilon) \left[V_{\mathrm{T}}\right]^{\bar{\bar{l}},\bar{l}}_{\bar{\bar{a}}\bar{a}} (\bar{\bar{\varepsilon}}, \bar{\varepsilon}) \tag{3.22}$$

holds. Therefore, one can write

$$\mathcal{W}^{\bar{l}1}_{\bar{a}a} = v_{\mathrm{T}} \mathcal{V}^{\bar{l}1}_{\bar{a}a} \mathcal{G}^{(0)}(\mathbf{r}_{\mathrm{T}}, \mathbf{r}_{\mathrm{T}}, \varepsilon). \tag{3.23}$$

As a consequence, the α-like term of the conductance correction due to a δ-tip is simply

$$g^{(2)\alpha} = 4\pi v_{\mathrm{T}} \mathrm{Im}\mathrm{Tr}\left\{\mathcal{G}^{(0)}(\mathbf{r}_{\mathrm{T}}, \mathbf{r}_{\mathrm{T}})(t^{\dagger}t\ \mathcal{V}^{11} + t^{\dagger}r'\ \mathcal{V}^{21})\right\}\ . \tag{3.24}$$

On the other hand the beta like term (3.16) can be written as

$$\delta^{(2)} J^{(\beta)}_{1\varepsilon a} = \frac{e\hbar}{M_{\mathrm{e}}} \sum_{\bar{l},\bar{\bar{l}}=1}^{2} \mathrm{Im} \left\{ \int_{\varepsilon_1^{(\mathrm{t})}}^{\infty} \frac{\mathrm{d}\bar{\varepsilon}}{\varepsilon^{-} - \bar{\varepsilon}} \int_{\varepsilon_1^{(\mathrm{t})}}^{\infty} \frac{\mathrm{d}\bar{\bar{\varepsilon}}}{\varepsilon^{+} - \bar{\bar{\varepsilon}}} \sum_{\bar{a},\bar{\bar{a}}} \left[V_{\mathrm{T}}\right]^{l\bar{l}}_{a\bar{a}} (\varepsilon, \bar{\varepsilon}) \left[j_{1/2}\right]^{\bar{l},\bar{\bar{l}}}_{\bar{a}\bar{\bar{a}}} (\bar{\varepsilon}, \bar{\bar{\varepsilon}})\ \left[V_{\mathrm{T}}\right]^{\bar{\bar{l}}l}_{\bar{\bar{a}}a} (\bar{\bar{\varepsilon}}, \varepsilon) \right\}, \tag{3.25}$$

where

$$\left[j_{1/2}\right]^{\bar{l}l}_{\bar{a}a} (\bar{\varepsilon}, \varepsilon) = \frac{e\hbar}{2iM_{\mathrm{e}}} \int \left[\Psi^{(0)*}_{\bar{l},\bar{\varepsilon},\bar{a}}(\mathbf{r})\ \partial_x \Psi^{(0)}_{l,\varepsilon,a}(\mathbf{r})\right] \mathrm{d}y. \tag{3.26}$$

After performing the energy integrals as in the Appendix C.2, this current correction leads to the following conductance correction [11, 15, 67]

$$\boxed{g^{(2)\beta} = 4\pi^2 \mathrm{Tr}\left\{\mathrm{Re}[\mathcal{V}^{11} t^{\dagger} t \mathcal{V}^{11} + 2\mathcal{V}^{11} t^{\dagger} r' \mathcal{V}^{21} + \mathcal{V}^{12} r'^{\dagger} r' \mathcal{V}^{21}]\right\}} \tag{3.27}$$

On a perfect conductance plateau ($r = r' = 0$) the total change of conductance up to second-order reduces to $g^{(2)}$, which simplifies to

$$g^{(2)} = 4\pi^2 \mathrm{Tr}\{t^{\dagger} t \mathcal{V}^{11}(\mathcal{V}^{11} - \rho(\mathbf{r}_{\mathrm{T}}, \varepsilon)\mathbb{1})\}, \tag{3.28}$$

with $\mathbb{1}$ the identity matrix and $\rho(\mathbf{r}_{\mathrm{T}}, \varepsilon) = -\frac{1}{\pi}\mathrm{Im}\mathcal{G}^{(0)}(\mathbf{r}_{\mathrm{T}}, \mathbf{r}_{\mathrm{T}}, \varepsilon)$. The obtained first and second order corrections, are real and basis independent. The traces have to be taken over the incoming right moving modes.

The results of this theory are important and will lead to an unambiguous interpretation of the SGM experiment as presented in Chapter 6.

Chapter 4

Higher order terms of the conductance expansion

In the previous chapter we have recalled how the lowest two orders of the perturbation theory can be obtained in the general case for any tip profile. It turns out that if the tip has the form of a δ-function, the full scattering wave-function is proportional to the unperturbed one. This enables us to sum up all the conductance corrections.

The calculation of the higher order terms of the conductance allows us to have an idea of how the SGM response behaves at large tip strengths.

4.1 The scattering wave-function in the case of a delta tip

Assuming a delta tip potential

$$V(\mathbf{r}) = v_{\mathrm{T}}\delta(\mathbf{r} - \mathbf{r}_{\mathrm{T}}), \tag{4.1}$$

let us start again from the Lippmann-Schwinger equation, giving

$$\psi_{l\varepsilon a}(\mathbf{r}) = \psi_{l\varepsilon a}^{(0)}(\mathbf{r}) + v_{\mathrm{T}}\mathcal{G}^{(0)}(\mathbf{r}, \mathbf{r}_{\mathrm{T}}, \varepsilon)\psi_{l\varepsilon a}(\mathbf{r}_{\mathrm{T}}). \tag{4.2}$$

Since the arguments of the scattering wave-function in the two sides of the equation are different one cannot simply isolate it. We can however take $\psi_{l\varepsilon a}(\mathbf{r})$ at the tip position $\mathbf{r}_{\mathrm{T}}$, which yields

$$\psi_{l\varepsilon a}(\mathbf{r}_{\mathrm{T}}) = \psi_{l\varepsilon a}^{(0)}(\mathbf{r}_{\mathrm{T}}) + v_{\mathrm{T}}\mathcal{G}^{(0)}(\mathbf{r}_{\mathrm{T}}, \mathbf{r}_{\mathrm{T}}, \varepsilon)\psi_{l\varepsilon a}(\mathbf{r}_{\mathrm{T}}). \tag{4.3}$$

Thus, the scattering wave function at the tip position is given by

$$\psi_{l\varepsilon a}(\mathbf{r}_{\mathrm{T}}) = \frac{\psi_{l\varepsilon a}^{(0)}(\mathbf{r}_{\mathrm{T}})}{1 - v_{\mathrm{T}}\mathcal{G}^{(0)}(\mathbf{r}_{\mathrm{T}}, \mathbf{r}_{\mathrm{T}}, \varepsilon)} \tag{4.4}$$

Subsequently, the scattering state at an arbitrary position $\mathbf{r}$ can be written in terms of the unperturbed quantities and the strength of the tip as follows

$$\psi_{l\varepsilon a}(\mathbf{r}) = \psi^{(0)}_{l\varepsilon a}(\mathbf{r}) + \upsilon_{\mathrm{T}} \frac{\mathcal{G}^{(0)}(\mathbf{r},\mathbf{r}_{\mathrm{T}},\varepsilon)\psi^{(0)}_{l\varepsilon a}(\mathbf{r}_{\mathrm{T}})}{1-\upsilon_{\mathrm{T}}\mathcal{G}^{(0)}(\mathbf{r}_{\mathrm{T}},\mathbf{r}_{\mathrm{T}},\varepsilon)} \tag{4.5}$$

To shorten the notation we introduce the function $\beta(\mathbf{r}_{\mathrm{T}},\varepsilon)$

$$\beta(\mathbf{r}_{\mathrm{T}},\varepsilon) = \frac{1}{1-\upsilon_{\mathrm{T}}\mathcal{G}^{(0)}(\mathbf{r}_{\mathrm{T}},\mathbf{r}_{\mathrm{T}},\varepsilon)}, \tag{4.6}$$

and write $\psi_{l\varepsilon a}$ as

$$\psi_{l\varepsilon a}(\mathbf{r}) = \psi^{(0)}_{l\varepsilon a}(\mathbf{r}) + \upsilon_{\mathrm{T}}\beta(\mathbf{r}_{\mathrm{T}},\varepsilon)\mathcal{G}^{(0)}(\mathbf{r},\mathbf{r}_{\mathrm{T}},\varepsilon)\psi^{(0)}_{l\varepsilon a}(\mathbf{r}_{\mathrm{T}}). \tag{4.7}$$

Now, the aim is to evaluate the conductance correction due to the second term of Eq. (4.7). To do so, we will replace the Green function by its expression in (1.15). This yields

$$\boxed{\psi_{l\varepsilon a}(\mathbf{r}) = \psi^{(0)}_{l\varepsilon a}(\mathbf{r}) + \sum_{\bar{a},\bar{l}} \int \frac{d\bar{\varepsilon}}{\varepsilon^{+}-\bar{\varepsilon}} \tilde{V}^{\bar{l}l}_{\bar{a}a}(\bar{\varepsilon},\varepsilon)\psi^{(0)}_{\bar{l}\bar{\varepsilon}\bar{a}}(\mathbf{r})} \tag{4.8}$$

where we have introduced an effective tip matrix element as

$$\tilde{V}^{\bar{l}l}_{\bar{a}a}(\bar{\varepsilon},\varepsilon) = \upsilon_{\mathrm{T}}\beta(\mathbf{r}_{\mathrm{T}},\varepsilon)\psi^{(0)*}_{\bar{l}\bar{\varepsilon}\bar{a}}(\mathbf{r}_{\mathrm{T}})\psi^{(0)}_{l\varepsilon a}(\mathbf{r}_{\mathrm{T}}). \tag{4.9}$$

One can systematically consider the second term of the right hand side of Eq. (4.8) as an effective first-order correction to the unperturbed wave-function. This will allow us to use the same results as the previously presented ones within the perturbative approach.

The current resulting from this term will neither be linear nor quadratic in the tip strength υ_{T}. This is due to the fact that the factor $\beta(\mathbf{r}_{\mathrm{T}},\varepsilon)$ depends on the tip strength according to (4.6), and will therefore contain higher order terms in υ_{T}.

In order to simplify the calculation of the current, we write the scattering wave function as

$$\psi_{l\varepsilon a}(\mathbf{r}) = \psi^{(0)}_{l\varepsilon a}(\mathbf{r}) + \tilde{\psi}^{(1)}_{l\varepsilon a}(\mathbf{r}). \tag{4.10}$$

4.2 Current density corrections

To get the corrections to the current density, one can proceed in exactly the same way as in Chapter 3 where we have obtained the two first order corrections in υ_{T}.

In addition to its unperturbed term $J\{\psi^{(0)}_{l\varepsilon a}(\mathbf{r})\}$, the current density carried by the scattering wave function (4.10) can be split into two contributions,

$$\tilde{J}\{\psi_{l\varepsilon a}(\mathbf{r})\} = J\{\psi^{(0)}_{l\varepsilon a}(\mathbf{r})\} + \delta\tilde{J}^{(1)} + \delta\tilde{J}^{(2)}, \tag{4.11}$$

with

$$\delta\tilde{J}^{(1)} = \frac{e\hbar}{M_e}\mathrm{Im}(\tilde{\psi}^{(1)*}_{l\varepsilon a}(\mathbf{r})\partial_x\psi^{(0)}_{l\varepsilon a}(\mathbf{r}) + \psi^{(0)*}_{l\varepsilon a}(\mathbf{r})\partial_x\tilde{\psi}^{(1)}_{l\varepsilon a}(\mathbf{r})), \tag{4.12}$$

and

$$\delta\tilde{J}^{(2)} = \frac{e\hbar}{M_e}\mathrm{Im}(\tilde{\psi}^{(1)*}_{l\varepsilon a}(\mathbf{r})\partial_x\tilde{\psi}^{(1)}_{l\varepsilon a}(\mathbf{r})). \tag{4.13}$$

The corresponding conductance corrections can be easily found from the corrections given in the previous section. We just have to substitute the real potential V by the effective complex potential $\tilde{V}$ even if the latter does not present the physical meaning of a potential supposed to be real to ensure the hermiticity of the Hamiltonian of the problem.

This substitution leads to the conductance correction

$$\boxed{\tilde{g}_1 = 4\pi\mathrm{Im}\{\beta(\mathbf{r}_\mathrm{T},\varepsilon)\mathrm{Tr}[t^\dagger t\mathcal{V}^{11} + t^\dagger r'\mathcal{V}^{21}]\}} \tag{4.14}$$

which obviously presents a structure of conductance, since it is real and basis independent.

We see from the expression of $\delta\tilde{J}^{(2)}$ that only the term similar to the β term of equation (3.27) is present, this leads to the correction

$$\boxed{\tilde{g}_2 = 4\pi^2|\beta(\mathbf{r}_\mathrm{T},\varepsilon)|^2\mathrm{Tr}\left\{\mathrm{Re}[\mathcal{V}^{11}t^\dagger t\mathcal{V}^{11} + 2\mathcal{V}^{11}t^\dagger r'\mathcal{V}^{21} + \mathcal{V}^{12}r'^\dagger r'\mathcal{V}^{21}]\right\}} \tag{4.15}$$

These results are valid for any dimension provided that the tip is local.

In Ref. [68] a similar result has been obtained for the resonant level model, where two semi-infinite leads are connected by a tunable single site impurity. On a conductance plateau, $\tilde{g}_1$ and $\tilde{g}_2$ simplify to

$$\tilde{g}_1 = 4\pi\mathrm{Im}\{\beta(\mathbf{r}_\mathrm{T},\varepsilon)\mathrm{Tr}[t^\dagger t\mathcal{V}^{11}]\}, \tag{4.16}$$

$$\tilde{g}_2 = 4\pi^2|\beta(\mathbf{r}_\mathrm{T},\varepsilon)|^2\mathrm{Tr}\left\{\mathrm{Re}[\mathcal{V}^{11}t^\dagger t\mathcal{V}^{11}]\right\}. \tag{4.17}$$

Noticing that $\mathrm{Tr}[t^\dagger t\mathcal{V}^{11}]$ and $\mathrm{Tr}[\mathcal{V}^{11}t^\dagger t\mathcal{V}^{11}]$ are real the conductances (4.16) and (4.17) can be simplified to

$$\tilde{g}_1 = 4\pi\mathrm{Im}\{\beta(\mathbf{r}_\mathrm{T},\varepsilon)\}\mathrm{Tr}[t^\dagger t\mathcal{V}^{11}], \tag{4.18}$$

$$\tilde{g}_2 = 4\pi^2|\beta(\mathbf{r}_\mathrm{T},\varepsilon)|^2\mathrm{Tr}[t^\dagger t(\mathcal{V}^{11})^2]. \tag{4.19}$$

The imaginary part of $\beta(\mathbf{r}_\mathrm{T}, \varepsilon)$ in (4.18) can be expressed in terms of the imaginary part of the Green function as

$$\mathrm{Im}\{\beta(\mathbf{r}_\mathrm{T}, \varepsilon)\} = |\beta(\mathbf{r}_\mathrm{T}, \varepsilon)|^2 \mathrm{Im}\{\mathcal{G}^{(0)}(\mathbf{r}_\mathrm{T}, \mathbf{r}_\mathrm{T}, \varepsilon)\}, \tag{4.20}$$

Introducing the LDOS ρ_ε defined as

$$\rho_\varepsilon(\mathbf{r}_\mathrm{T}) = -\frac{1}{\pi} \mathrm{Im}\{\mathcal{G}^{(0)}(\mathbf{r}_\mathrm{T}, \mathbf{r}_\mathrm{T}, \varepsilon)\}, \tag{4.21}$$

$\mathrm{Im}\{\beta(\mathbf{r}_\mathrm{T}, \varepsilon)\}$ can be written as

$$\mathrm{Im}\{\beta(\mathbf{r}_\mathrm{T}, \varepsilon)\} = -\pi |\beta(\mathbf{r}_\mathrm{T}, \varepsilon)|^2 \rho(\mathbf{r}_\mathrm{T}, \varepsilon). \tag{4.22}$$

Therefore using (4.22) in (4.18) and summing up the resulting $\tilde{g}_1$ with $\tilde{g}_2$ the total conductance correction $\tilde{g} = \tilde{g}_1 + \tilde{g}_2$ reads

$$\tilde{g} = 4\pi^2 |\beta(\mathbf{r}_\mathrm{T}, \varepsilon)|^2 \mathrm{Tr}\{t^\dagger t \mathcal{V}^{11} (\mathcal{V}^{11} - \rho(\mathbf{r}_\mathrm{T}, \varepsilon)\mathbb{1})\}, \tag{4.23}$$

with $\mathbb{1}$ the identity matrix. While this conductance formula is already rather simple, its expression in the transmission eigenbasis is even simpler. In that basis one can write

$$\tilde{g} = 4\pi^2 |\beta(\mathbf{r}_\mathrm{T}, \varepsilon)|^2 \sum_m [\mathcal{U}^{11} (\mathcal{U}^{11} - \rho(\mathbf{r}_\mathrm{T}, \varepsilon)\mathbb{1})]_{mm}, \tag{4.24}$$

where $\mathcal{U}^{11}_{mn}$ are the matrix elements of the tip potential in the transmission eigenbasis they are generally given by

$$\mathcal{U}^{ll'}_{mm'} = \int \chi^*_{l\varepsilon m}(\mathbf{r}') V_\mathrm{T}(\mathbf{r}') \chi_{l'\varepsilon m'}(\mathbf{r}') \mathrm{d}\mathbf{r}'. \tag{4.25}$$

Since we have considered a delta-tip, these matrix elements are simply the product between the involved scattering states with the tip strength as a prefactor

$$\mathcal{U}^{11}_{mn} = \upsilon_\mathrm{T} \chi^*_{1\varepsilon m}(\mathbf{r}_\mathrm{T}) \chi_{1\varepsilon n}(\mathbf{r}_\mathrm{T}). \tag{4.26}$$

Plugging (4.26) in (4.24) one can write

$$\tilde{g} = 4\pi^2 |\beta(\mathbf{r}_\mathrm{T}, \varepsilon)|^2 \sum_m \mathcal{U}^{11}_{mm} (\sum_n \mathcal{U}^{11}_{nn} - \rho(\mathbf{r}_\mathrm{T}, \varepsilon)). \tag{4.27}$$

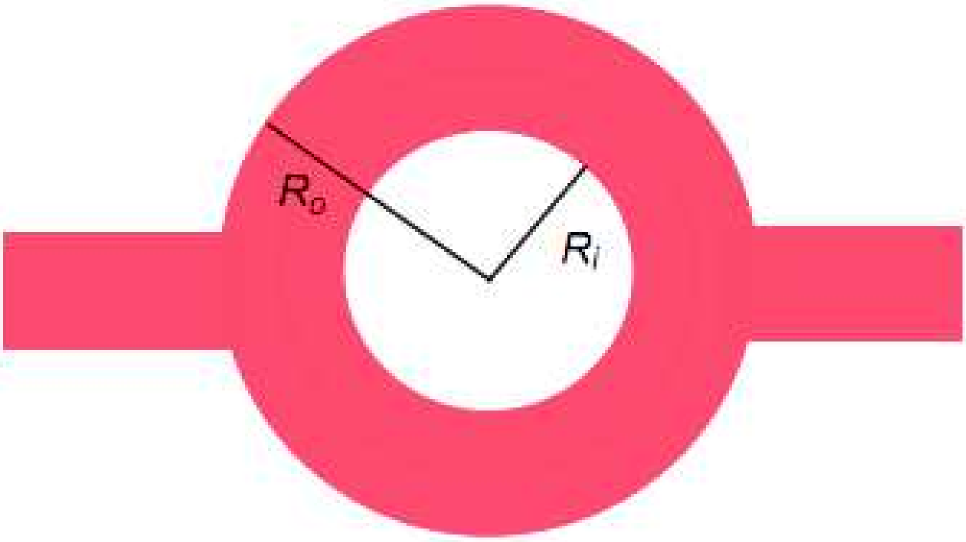

Figure 4.1: A sketch illustrating the geometry of the considered quantum ring with inner radius of $R_i = 50a$ and outer radius of $R_o = 100a$.

4.3 Numerical check of the conductance saturation

We consider a ring geometry defined in a tight binding network with lattice parameter $a = 1$ the ring possesses an inner radius of $50a$ and an outer radius of $100a$ (see Fig. 4.1). The numerical implementation is done via Kwant. The effective mass is $m^* = 0.04m$, with m the bare electron mass as in Ref. [6], where such a system was made in InGaAs/InAlAs heterostructure.

In Fig. 4.2 the conductance of the ring is plotted versus the strength v_{T} of a local tip. We observe that the conductance of the ring saturates at different values for the different tip positions. This is due to the fact that the value at which the conductance saturates depends on the diagonal Green function according to (4.14) and (4.15). We observe that the analytical predictions coincides perfectly with the numerical calculations.

In the inset of Fig. 4.2 we compare between the full SGM response and the sum of the two lowest order corrections to the conductance. We see that for relatively strong tips the higher order terms should be taken into account.

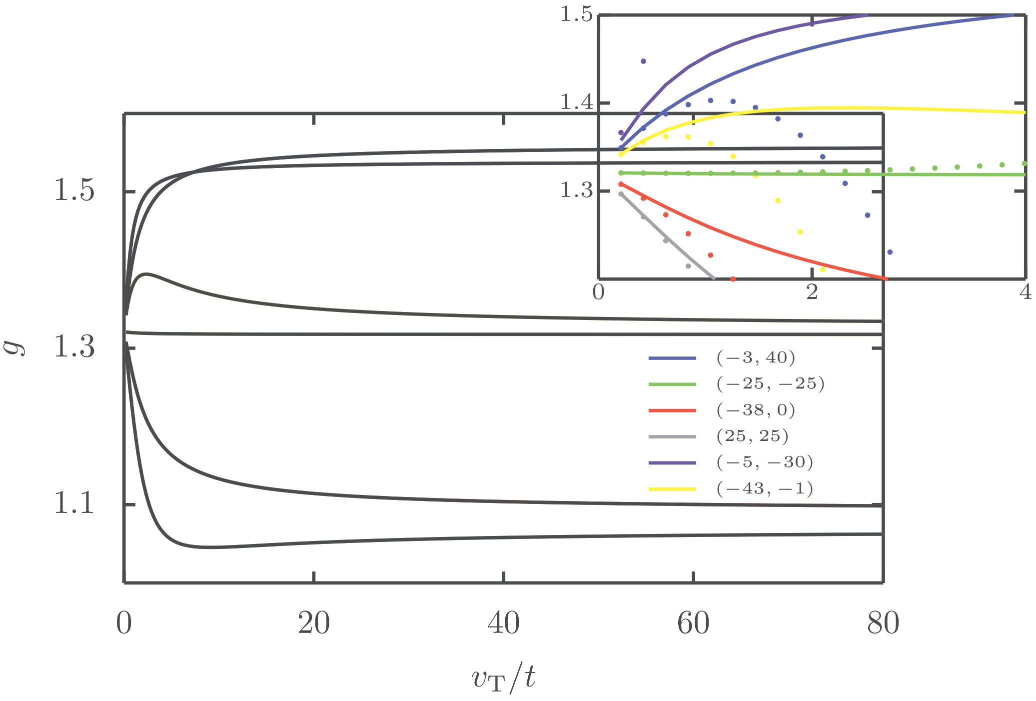

Figure 4.2: In the main figure the conductance of the quantum ring is plotted as a function of the strength of a local tip. Each color line corresponds to an arbitrarily chosen tip position in the ring geometry. The dashed lines correspond to the analytical predictions of (4.14) and (4.15). In the inset we show the sum of the two lowest order corrections to g (dots) and the full conductance g with higher order terms (solid lines).

Chapter 5

Green function method for computing the conductance in the presence of a finite-size scatterer

In the previous chapter, we have shown how the full scattering wave-function in the presence of a $\delta-$like tip can be expressed in terms of the unperturbed scattering wave-function, and this has enabled us to obtain the analytical form of the conductance corrections without any restriction on the strength of the $\delta-$like tip.

In this chapter we propose a method that allows us to iteratively construct the scattering wave-function in the presence of an arbitrary tip potential with finite range, starting from the unperturbed scattering wave-function as well as the unperturbed Green function, enabling us to compute the conductance for each position of the scatterer, just from the unperturbed quantities. This prevents us to to calculate the transmission at each tip position.

5.1 Scattering wave-function

The Lippmann-Schwinger equation is an integral equation, that is not easy to solve except for simple cases, when the scattering potential is assumed to have a simple form, a Dirac-Delta form for instance. This case has been treated in the previous chapter, as mentioned in the introductory paragraph.

Let $V(\mathbf{r})$ be an arbitrary potential, then it can be written as a convolution product with a Dirac δ

$$V(\mathbf{r}) = \int \mathrm{d}\bar{\mathbf{r}} V(\bar{\mathbf{r}}) \delta(\mathbf{r} - \bar{\mathbf{r}}). \tag{5.1}$$

In a tight-binding model the previous convolution (5.1) becomes the sum

$$V(\mathbf{r}_j) = \sum_i v_i \delta_{i,j}, \tag{5.2}$$

with $v_i = V(\mathbf{r}_i)$.

The idea therefore, is to successively consider the individual Kronecker-δs.

According to (4.7), the scattering wave-function in the presence of the first added δ localized at $\mathbf{r}_1$ is

$$\psi^{(1)}(\mathbf{r}) = \psi^{(0)}(\mathbf{r}) + v_1 \frac{\psi^{(0)}(\mathbf{r}_1)}{1 - v_1 \mathcal{G}^{(0)}(\mathbf{r}_1, \mathbf{r}_1)} \mathcal{G}^{(0)}(\mathbf{r}, \mathbf{r}_1), \tag{5.3}$$

where $\mathcal{G}^{(0)}(\mathbf{r}, \mathbf{r}_1)$, $\psi^{(0)}$ is the unperturbed Green function and the unperturbed scattering wave-function. For the quest of simplifying the notation, we have omitted the lead index, the energy and the mode index. Thus $\psi^{(0)}$ is understood to be the ath scattering wave-function coming from lead l at energy ε. Now, we add another $\delta-$function at $\mathbf{r} = \mathbf{r}_2$, and the resulting scattering wave-function can be obtained from $\psi^{(1)}$ as

$$\psi^{(2)}(\mathbf{r}) = \psi^{(1)}(\mathbf{r}) + \frac{\psi^{(1)}(\mathbf{r}_2)}{1 - v_2 \mathcal{G}^{(1)}(\mathbf{r}_2, \mathbf{r}_2)} \mathcal{G}^{(1)}(\mathbf{r}, \mathbf{r}_2). \tag{5.4}$$

To express $\psi^{(2)}$ in terms of the unperturbed scattering wave-function $\psi^{(0)}$, we replace $\psi^{(1)}$ by its expression in terms of $\psi^{(0)}$, this gives

$$\psi^{(2)}(\mathbf{r}) = \psi^{(0)}(\mathbf{r}) + \frac{\psi^{(0)}(\mathbf{r}_1)}{1 - v_1 \mathcal{G}^{(0)}(\mathbf{r}_1, \mathbf{r}_1)} \mathcal{G}^{(0)}(\mathbf{r}, \mathbf{r}_1) + \frac{\psi^{(1)}(\mathbf{r}_2)}{1 - v_2 \mathcal{G}^{(1)}(\mathbf{r}_2, \mathbf{r}_2)} \mathcal{G}^{(1)}(\mathbf{r}, \mathbf{r}_2). \tag{5.5}$$

The generalization of (5.5) for the added nth point-like potential v_n at $\mathbf{r}_n$ is straightforward, and reads

$$\boxed{\psi^{(n)}(\mathbf{r}) = \psi^{(0)}(\mathbf{r}) + \sum_{i=1}^{n} \frac{\psi^{(i-1)}(\mathbf{r}_i)}{1 - v_i \mathcal{G}^{(i-1)}(\mathbf{r}_i, \mathbf{r}_i)} \mathcal{G}^{(i-1)}(\mathbf{r}, \mathbf{r}_i)} \tag{5.6}$$

this provides the main equation of this section. The next step is to get rid of the $\mathbf{r}$ dependence in $\mathcal{G}^{(i-1)}(\mathbf{r}, \mathbf{r}_i)$ in order to be able to easily perform the energy integrals in the Green function as done in Chapter 3. This means that the dependence on $\mathbf{r}$ should appear only in the unperturbed quantities $\psi^{(0)}$ and $G^{(0)}$. Therefore, the Green function $\mathcal{G}^{(i-1)}(\mathbf{r}, \mathbf{r}_i)$ involved in (5.6) has to be expressed in terms of the unperturbed quantity $\mathcal{G}^{(0)}(\mathbf{r}, \mathbf{r}_i)$.

5.2 The full Green function in terms of the unperturbed quantities

Considering the nth $\delta-$potential as a perturbation of the system with $n-1$ δs, the Dyson equation relating the Full Green function i.e in the presence of the nth point-like potential to the Green function of the system with the first $n-1$ point-like potentials reads

$$\mathcal{G}^{(n)}(\mathbf{r},\mathbf{r}') = \mathcal{G}^{(n-1)}(\mathbf{r},\mathbf{r}') + v_n \sum_k \mathcal{G}^{(n-1)}(\mathbf{r},\mathbf{r}_k)\delta_{k,n}\mathcal{G}^{(n)}(\mathbf{r}_k,\mathbf{r}'). \tag{5.7}$$

After summation (5.7) becomes

$$\mathcal{G}^{(n)}(\mathbf{r},\mathbf{r}') = \mathcal{G}^{(n-1)}(\mathbf{r},\mathbf{r}') + v_n \mathcal{G}^{(n-1)}(\mathbf{r},\mathbf{r}_n)\mathcal{G}^{(n)}(\mathbf{r}_n,\mathbf{r}'). \tag{5.8}$$

By taking $\mathbf{r} = \mathbf{r}_n$ in (5.7), we find $\mathcal{G}^{(n)}(\mathbf{r}_n,\mathbf{r}')$ as

$$\mathcal{G}^{(n)}(\mathbf{r}_n,\mathbf{r}') = \frac{\mathcal{G}^{(n-1)}(\mathbf{r}_n,\mathbf{r}')}{1 - v_n\mathcal{G}^{(n-1)}(\mathbf{r}_n,\mathbf{r}_n)}. \tag{5.9}$$

Plugging (5.9) into (5.8) we find

$$\mathcal{G}^{(n)}(\mathbf{r},\mathbf{r}') = \mathcal{G}^{(n-1)}(\mathbf{r},\mathbf{r}') + z_n(\mathbf{r}')\mathcal{G}^{(n-1)}(\mathbf{r},\mathbf{r}_n), \tag{5.10}$$

where we have introduced the function z_n defined as

$$z_n(\mathbf{r}') = v_n \frac{\mathcal{G}^{(n-1)}(\mathbf{r}_n,\mathbf{r}')}{1 - v_n\mathcal{G}^{(n-1)}(\mathbf{r}_n,\mathbf{r}_n)}. \tag{5.11}$$

The application of (5.10) for $n = 1$ gives

$$\mathcal{G}^{(1)}(\mathbf{r},\mathbf{r}') = \mathcal{G}^{(0)}(\mathbf{r},\mathbf{r}') + z_1(\mathbf{r}')\mathcal{G}^{(0)}(\mathbf{r},\mathbf{r}_1). \tag{5.12}$$

For $n = 2$, Eq. (5.10) yields,

$$\mathcal{G}^{(2)}(\mathbf{r},\mathbf{r}') = \mathcal{G}^{(0)}(\mathbf{r},\mathbf{r}') + z_1(\mathbf{r}')\mathcal{G}^{(0)}(\mathbf{r},\mathbf{r}_1) + z_2(\mathbf{r}')\mathcal{G}^{(1)}(\mathbf{r},\mathbf{r}_2). \tag{5.13}$$

Replacing $\mathcal{G}^{(1)}(\mathbf{r},\mathbf{r}_2)$ by its expression (5.12) in (5.13) we get

$$\begin{aligned}\mathcal{G}^{(2)}(\mathbf{r},\mathbf{r}') &= \mathcal{G}^{(0)}(\mathbf{r},\mathbf{r}') + z_1(\mathbf{r}')\mathcal{G}^{(0)}(\mathbf{r},\mathbf{r}_1) \\ &+ z_2(\mathbf{r}')\mathcal{G}^{(0)}(\mathbf{r},\mathbf{r}_2) + z_1(\mathbf{r}_2)z_2(\mathbf{r}')\mathcal{G}^{(0)}(\mathbf{r},\mathbf{r}_1). \end{aligned} \tag{5.14}$$

This is more adequate to write (5.14) as

$$\begin{aligned}\mathcal{G}^{(2)}(\mathbf{r},\mathbf{r}') &= \mathcal{G}^{(0)}(\mathbf{r},\mathbf{r}') + [z_1(\mathbf{r}') + z_1(\mathbf{r}_2)z_2(\mathbf{r}')]\mathcal{G}^{(0)}(\mathbf{r},\mathbf{r}_1) \\ &+ z_2(\mathbf{r}')\mathcal{G}^{(0)}(\mathbf{r},\mathbf{r}_2). \end{aligned} \tag{5.15}$$

Similarly, for $n = 3$, the full Green function is given by

$$\begin{aligned}\mathcal{G}^{(3)}(\mathbf{r},\mathbf{r}') = \mathcal{G}^{(0)}(\mathbf{r},\mathbf{r}') + \Big\{ & z_1(\mathbf{r}') + z_1(\mathbf{r}_2)z_2(\mathbf{r}') + z_1(\mathbf{r}_3)z_3(\mathbf{r}') \\ & + z_1(\mathbf{r}_2)z_2(\mathbf{r}_3)z_3(\mathbf{r}')\Big\}\mathcal{G}^{(0)}(\mathbf{r},\mathbf{r}_1) \\ & + \Big\{z_2(\mathbf{r}') + z_2(\mathbf{r}_3)z_3(\mathbf{r}')\Big\}\mathcal{G}^{(0)}(\mathbf{r},\mathbf{r}_2) \\ & + z_3(\mathbf{r}')\mathcal{G}^{(0)}(\mathbf{r},\mathbf{r}_3). \qquad (5.16)\end{aligned}$$

We introduce the function $Z_k^{(n)}(\mathbf{r}')$ such that

$$\begin{aligned}Z_1^{(3)}(\mathbf{r}') &= z_1(\mathbf{r}') + z_1(\mathbf{r}_2)z_2(\mathbf{r}') + z_1(\mathbf{r}_3)z_3(\mathbf{r}') + z_1(\mathbf{r}_2)z_2(\mathbf{r}_3)z_3(\mathbf{r}'), \\ Z_2^{(3)}(\mathbf{r}') &= z_2(\mathbf{r}') + z_2(\mathbf{r}_3)z_3(\mathbf{r}'), \\ Z_3^{(3)}(\mathbf{r}') &= z_3(\mathbf{r}'). \qquad (5.17)\end{aligned}$$

To construct $Z_k^{(n)}$, we should perform the maximal crossing product

$$z_k(\mathbf{r}_{k+1})...z_{n-1}(\mathbf{r}_n)z_n(\mathbf{r}')$$

and add all the other possible products by decreasing a term after each iteration, until we arrive to the single element $z_k(\mathbf{r}')$.

The $Z_k^{(n)}$ obey the following two recursion relations

$$\begin{aligned}Z_k^{(n+1)}(\mathbf{r}') &= Z_k^{(n)}(\mathbf{r}') + z_{n+1}(\mathbf{r}')Z_k^{(n)}(\mathbf{r}_{n+1}), \\ Z_{k+1}^{(n)}(\mathbf{r}') &= \frac{Z_k^{(n)}(\mathbf{r}') - z_k(\mathbf{r}')}{z_k(\mathbf{r}_{k+1})}. \qquad (5.18)\end{aligned}$$

The use of (5.17) in (5.16), allows us to write $\mathcal{G}^{(3)}(\mathbf{r},\mathbf{r}')$ as

$$\begin{aligned}\mathcal{G}^{(3)}(\mathbf{r},\mathbf{r}') &= \mathcal{G}^{(0)}(\mathbf{r},\mathbf{r}') + Z_1^{(3)}(\mathbf{r}')\mathcal{G}^{(0)}(\mathbf{r},\mathbf{r}_1) \\ &+ Z_2^{(3)}(\mathbf{r}')\mathcal{G}^{(0)}(\mathbf{r},\mathbf{r}_2) + Z_3^{(3)}(\mathbf{r}')\mathcal{G}^{(0)}(\mathbf{r},\mathbf{r}_3). \qquad (5.19)\end{aligned}$$

We generalize Eq. (5.19) for any n as follows

$$\boxed{\mathcal{G}^{(n)}(\mathbf{r},\mathbf{r}') = \mathcal{G}^{(0)}(\mathbf{r},\mathbf{r}') + \sum_{k=1}^{n} Z_k^{(n)}(\mathbf{r}')\mathcal{G}^{(0)}(\mathbf{r},\mathbf{r}_k)} \qquad (5.20)$$

with $Z_n^{(n)}(\mathbf{r}') = z_n(\mathbf{r}')$.

To prove (5.20) we assume that it holds for n and show that it necessarily holds for $n+1$.

We have from (5.10)

$$\mathcal{G}^{(n+1)}(\mathbf{r},\mathbf{r}') = \mathcal{G}^{(n)}(\mathbf{r},\mathbf{r}') + z_{n+1}(\mathbf{r}')\mathcal{G}^{(n+1)}(\mathbf{r},\mathbf{r}_{n+1}). \tag{5.21}$$

Plugging (5.20) into (5.21) the latter becomes

$$\begin{aligned}\mathcal{G}^{(n+1)}(\mathbf{r},\mathbf{r}') = \mathcal{G}^{(0)}(\mathbf{r},\mathbf{r}') + \sum_{k=1}^{n}\Big\{Z_k^{(n)}(\mathbf{r}') + z_{n+1}(\mathbf{r}')Z_k^{(n)}(\mathbf{r}_{n+1})\Big\}\mathcal{G}^{(0)}(\mathbf{r},\mathbf{r}_k)\\ + z_{n+1}(\mathbf{r}')\mathcal{G}^{(0)}(\mathbf{r},\mathbf{r}_{n+1}),\end{aligned} \tag{5.22}$$

using the first line of (5.18), and the fact that $Z_{n+1}^{(n+1)}(\mathbf{r}') = z_{n+1}(\mathbf{r}')$, we end up with

$$\mathcal{G}^{(n+1)}(\mathbf{r},\mathbf{r}') = \mathcal{G}^{(0)}(\mathbf{r},\mathbf{r}') + \sum_{k=1}^{n+1} Z_k^{(n+1)}(\mathbf{r}')\mathcal{G}^{(0)}(\mathbf{r},\mathbf{r}_k). \tag{5.23}$$

This provides a proof of the recursion relation (5.20) which is the main result of the present section. It expresses the full Green function $\mathcal{G}^{(n)}$ in terms of the unperturbed Green function $\mathcal{G}^{(0)}$.

Now, let us return to the calculation of the scattering wave-function. Using Eq. (5.20) in (5.6), the scattering wave-function $\psi^{(n)}(\mathbf{r})$ (for $n > 0$) can be written as

$$\begin{aligned}\psi^{(n)}(\mathbf{r}) = \psi^{(0)}(\mathbf{r}) + \sum_{i=1}^{n}\frac{v_i\psi^{(i-1)}(\mathbf{r}_i)}{1 - v_i\mathcal{G}^{(i-1)}(\mathbf{r}_i,\mathbf{r}_i)}\Bigg\{\ \mathcal{G}^{(0)}(\mathbf{r},\mathbf{r}_i)\\ + \sum_{k=1}^{i-1} Z_k^{(i-1)}(\mathbf{r}_i)\mathcal{G}^{(0)}(\mathbf{r},\mathbf{r}_k)\Bigg\},\end{aligned} \tag{5.24}$$

with $Z_k^{(0)} = 0$.

Replacing the Green functions $\mathcal{G}^{(0)}(\mathbf{r},\mathbf{r}_i)$ and $\mathcal{G}^{(0)}(\mathbf{r},\mathbf{r}_k)$ by their expressions (Eq. (1.15)) in (11.21) we get

$$\boxed{\psi_{l\varepsilon a}^{(n)}(\mathbf{r}) = \psi_{l\varepsilon a}^{(0)}(\mathbf{r}) + \sum_{\bar{a}\bar{l}}\int\frac{\mathrm{d}\bar{\varepsilon}}{\varepsilon^{+} - \bar{\varepsilon}}\hat{V}_{\bar{a}a}^{\bar{l}l}(\bar{\varepsilon},\varepsilon)\psi_{\bar{l}\bar{\varepsilon}\bar{a}}^{(0)}(\mathbf{r})} \tag{5.25}$$

where we have introduced the matrix $\hat{V}$ with matrix elements defined by

$$\hat{V}_{\bar{a}a}^{\bar{l}l}(\bar{\varepsilon},\varepsilon) = \sum_{i=1}^{n}\frac{v_i\psi_{l\varepsilon a}^{(i-1)}(\mathbf{r}_i)}{1 - v_i\mathcal{G}^{(i-1)}(\mathbf{r}_i,\mathbf{r}_i)}\Bigg\{\psi_{\bar{l}\bar{\varepsilon}\bar{a}}^{(0)*}(\mathbf{r}_i) + \sum_{k=1}^{i-1} Z_k^{(i-1)}(\mathbf{r}_i)\psi_{\bar{l}\bar{\varepsilon}\bar{a}}^{(0)*}(\mathbf{r}_k)\Bigg\}. \tag{5.26}$$

To compute the conductance, note that the scattering wave-function (5.25) is analogous to the one given by Eq. (4.8). Therefore, the conductance correction due to the scatterer can be analogously deduced by replacing the tip matrix element by an effective one defined by (11.23). Accordingly, the resulting conductance reads

$$\begin{aligned}\delta g = 4\pi \mathrm{Im}\Big\{ \mathrm{Tr}[t^\dagger t \hat{\mathcal{V}}^{11} + t^\dagger r' \hat{\mathcal{V}}^{21}] \Big\} \\ + 4\pi^2 \mathrm{Tr}\Big\{ \mathrm{Re}[\hat{\mathcal{V}}^{11} t^\dagger t \hat{\mathcal{V}}^{11} + 2\hat{\mathcal{V}}^{11} t^\dagger r' \hat{\mathcal{V}}^{21} + \hat{\mathcal{V}}^{12} r'^\dagger r' \hat{\mathcal{V}}^{21}] \Big\},\end{aligned} \tag{5.27}$$

where $\hat{\mathcal{V}}^{l\bar{l}}_{a\bar{a}} = \hat{V}^{l\bar{l}}_{a\bar{a}}(\varepsilon, \varepsilon)$.

The case of one $\delta-$tip located at position $\mathbf{r}_0$ is obtained by noticing that $Z^{(0)}_k = 0$, therefore the Eq. (5.27) coincides with the result of the previous chapter.

5.3 Comments on the method

The advantage of the method is to provide an analytical result for the conductance. Instead of calculating the scattering matrix for each position of the scatterer, we are only concerned with the unperturbed scattering matrix, scattering wave-function and the Green function at a given energy. In principle, this method should be quicker than the traditional calculation of conductance, most remarkably if the potential extension is not large.

Interestingly, this method is quite useful in calculations involving disorder average and similar memory consuming calculations. Moreover, the method provides an algorithm that can be easily parallelized.

5.4 Summary of the method

For an implementation of the method, the following steps have to be performed

- 1) Calculate the unperturbed quantities $\mathcal{G}^{(0)}$ and $\psi^{(0)}$ and the unperturbed scattering matrix.
- 2) Construct the successive $\mathcal{G}^{(i)}$ and $\psi^{(i)}$ from step 1).
- 3) Construct the coefficients z from (5.11).

- 4) Construct the coefficients Z from (5.18).
- 5) Use the Eq. (5.27) to compute the conductance.

Chapter 6

PLDOS from SGM measurements

In this chapter the first and second order corrections to the quantum conductance given in Chapter 3 are used to derive correspondence relations between the low-temperature SGM response (that can be measured in an experiment) and the PLDOS in clean and disordered structures, thereby providing a way to indirectly measure the PLDOS. The results of this chapter are in our publication [69].

6.1 $g^{(1)}(\mathbf{r}_\mathrm{T})$ versus PLDOS in the conductance steps

Focusing first on the QPC setup without disorder sketched in Fig. 1.6, the asymptotic form of the scattering eigenfunctions can be used everywhere in the 2DEG, except in and very close to the constriction. The form (1.37) of the scattering eigenfunctions gives the product of scattering functions impinging from different leads in the first order correction (11.9) due to a weak δ-potential scanned in the right hand side of the QPC as

$$\begin{aligned}&\chi^*_{2,\varepsilon,m}(\mathbf{r})\chi_{1,\varepsilon,m}(\mathbf{r})\\ &\qquad = \mathcal{T}_m \left\{ \varrho^{(+)\,2}_{2,\varepsilon,m}(\mathbf{r}) + \mathcal{R}_m \varrho^{(+)}_{2,\varepsilon,m}(\mathbf{r}) \varrho^{(-)}_{2,\varepsilon,m}(\mathbf{r}) \right\} . \qquad (6.1)\end{aligned}$$

Using the fact that $\varrho^{(-)}_{2,\varepsilon,m}(\mathbf{r}) = \varrho^{(+)\,*}_{2,\varepsilon,m}(\mathbf{r})$ we have

$$\mathrm{Im}\left\{\chi^*_{2,\varepsilon,m}(\mathbf{r})\chi_{1,\varepsilon,m}(\mathbf{r})\right\} = \mathcal{T}_m \mathrm{Im}\left\{ \varrho^{(+)\,2}_{2,\varepsilon,m}(\mathbf{r}) \right\} . \qquad (6.2)$$

From (1.37) $\varrho^{(+)}_{2,\varepsilon,m}(\mathbf{r}) = \chi_{1,\varepsilon,m}(\mathbf{r})/\mathcal{T}_m$ for $x > 0$ and Eq. (11.9) simplifies to

$$g^{(1)}(\mathbf{r}_\mathrm{T}) = 4\pi \sum_{m=1}^{M} \mathcal{R}_m \mathrm{Im}\left\{\chi^2_{1,\varepsilon_\mathrm{F},m}(\mathbf{r}_\mathrm{T})\right\} . \qquad (6.3)$$

Denoting $\alpha_{l,\varepsilon,m}(\mathbf{r})$ the argument of $\chi_{l,\varepsilon,m}(\mathbf{r})$, Eq. (6.3) can be written as

$$g^{(1)}(\mathbf{r}_\mathrm{T}) = 4\pi \sum_{m=1}^{M} \mathcal{R}_m \sin[2\alpha_{1,\varepsilon_\mathrm{F},m}(\mathbf{r}_\mathrm{T})] |\chi_{1,\varepsilon_\mathrm{F},m}(\mathbf{r}_\mathrm{T})|^2 \,. \tag{6.4}$$

The sum over eigenmodes reduces to the contribution of the last one ($m = M$), which is the only partially open channel having $R_m > 0$.

In order to establish a link between the conductance corrections and the local properties, we recall the spinless PLDOS for electrons incoming from lead l

$$\rho_{l\varepsilon}(\mathbf{r}) = 2\pi \sum_{a=1}^{N} |\psi_{l,\varepsilon,a}(\mathbf{r})|^2 \,. \tag{6.5}$$

Interestingly, in the case of a single open channel ($M = 1$) there is a direct relation between the first-order conductance change and the PLDOS,

$$\boxed{g^{(1)}(\mathbf{r}_\mathrm{T}) = 2\mathcal{R}_1 \sin[2\alpha_{1,\varepsilon_\mathrm{F},1}(\mathbf{r}_\mathrm{T})] \rho_{1\varepsilon_\mathrm{F}}(\mathbf{r}_\mathrm{T})} \tag{6.6}$$

for $\mathbf{r}_\mathrm{T}$ in the RHS of the scatterer. In a disorder-free 2DEG, the prefactor $\sin(2\alpha_{1,\varepsilon_\mathrm{F},1})$ of the SGM response is simply $\sin(2k_\mathrm{F}r + \alpha_0)$ with a constant phase α_0, thus generating half Fermi wavelength, $\lambda_\mathrm{F}/2$, oscillations and a proportionality factor $2\mathcal{R}_1$ between the spatial oscillation amplitude of the first order conductance correction in the first step and the PLDOS.

In the case of a disordered structure, Eq. (6.6) does not apply inside the disordered region, nevertheless if the disorder is weak and leads to small-angle forward scattering only, one can expect the structure of Eq. (6.6) to mostly remain. For example, the phase oscillation cannot have such a simple position-dependence strictly speaking, but a paraxial optical approximation [70] holds and a fairly regular radial phase behavior of nearly the same wavelength persists in the eigenfunctions. In these circumstances, the explicit dependence of the SGM response on the phase of the scattering eigenfunction might be helpful in characterizing properties of the fluctuating potential in the 2DEG with further analysis.

In Fig. 6.1 we have numerically verified the validity of (6.6) in the presence of disorder. In the left panel of this figure the numerically calculated SGM for very weak tip ($v_\mathrm{T} = \varepsilon_\mathrm{F} a^2/4$) in the first conductance step is presented. We used the QPC defined in Chapter 1, the width of the QPC is $w = 11a$ and its length $L = 19a$. The disorder is generated using the procedure introduced in 1.13.2. The resulting configuration is shown in Fig. 6.2. The QPC is tuned to the first conductance step, with $g = 0.7$ corresponding to the Fermi energy $\varepsilon_\mathrm{F} = 0.06t$. In the right panel of Fig. 6.1 we evaluated

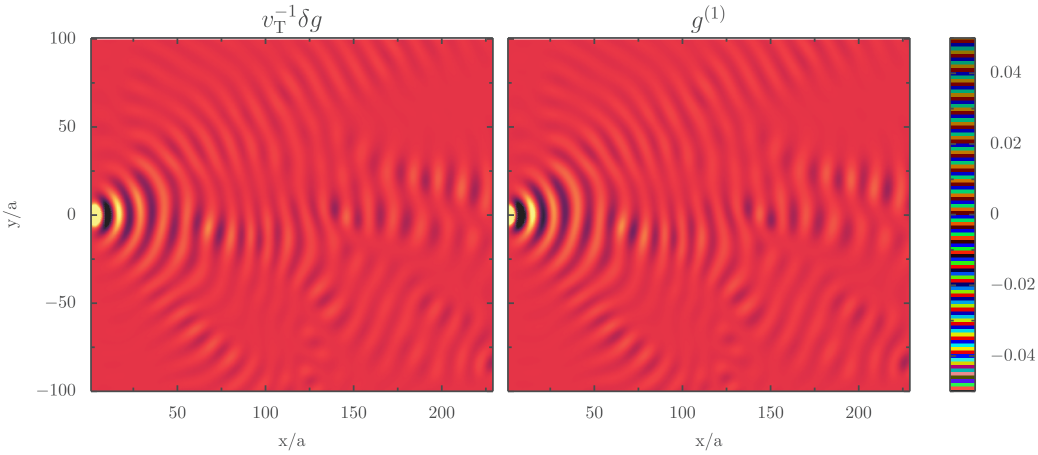

Figure 6.1: Left panel : the numerically calculated SGM for very weak tip ($v_\mathrm{T} = \varepsilon_\mathrm{F} a^2/4$) in the step of conductance is presented. Right panel : the analytical form of $g^{(1)}$ is calculated. Notice that in these conditions (weak v_T with QPC tuned to a step of conductance) the full SGM response is well-approximated by $v_\mathrm{T} g^{(1)}$.

the analytical form of $g^{(1)}$ according to (6.6). The wave-functions, their arguments $\alpha_{1,\varepsilon_\mathrm{F},1}$ and the scattering matrix are calculated using Kwant. One observes that in the presence of weak disorder the first order SGM response is related to the PLDOS exactly as predicted by the analytical theory leading to (6.6).

In general, the first-order conductance correction in tip-strength is not simply proportional to the PLDOS, even in the case of a δ-tip. In fact, $g^{(1)}(\mathbf{r}_\mathrm{T})$ is only local in the sense that (with a space independent proportionality constant) $\mathrm{Im}\left\{\chi^2_{1,\varepsilon_\mathrm{F},m}(\mathbf{r}_\mathrm{T})\right\}$ is the local information about the eigenfunction of the unperturbed system. However, in the case of a single partial mode the PLDOS provides an upper bound for the absolute value of the former, and the sinusoidal term creates a fringing effect.

For one-dimensional tight-binding systems the SGM response has been expressed in terms of the real part of the local Green function [56, 48] and thereby related to the LDOS. We have checked that in the case of a one-dimensional chain the first-order conductance correction (11.9) (and therefore also the relation (6.6)) is consistent with the result of Refs. [56, 48]. However, (11.9) is more general and (6.6) is expected to be valid whenever there is only one single partially open mode of the QPC, without being limited to strictly one-dimensional systems. This issue will be discussed later in the Chapter 8.

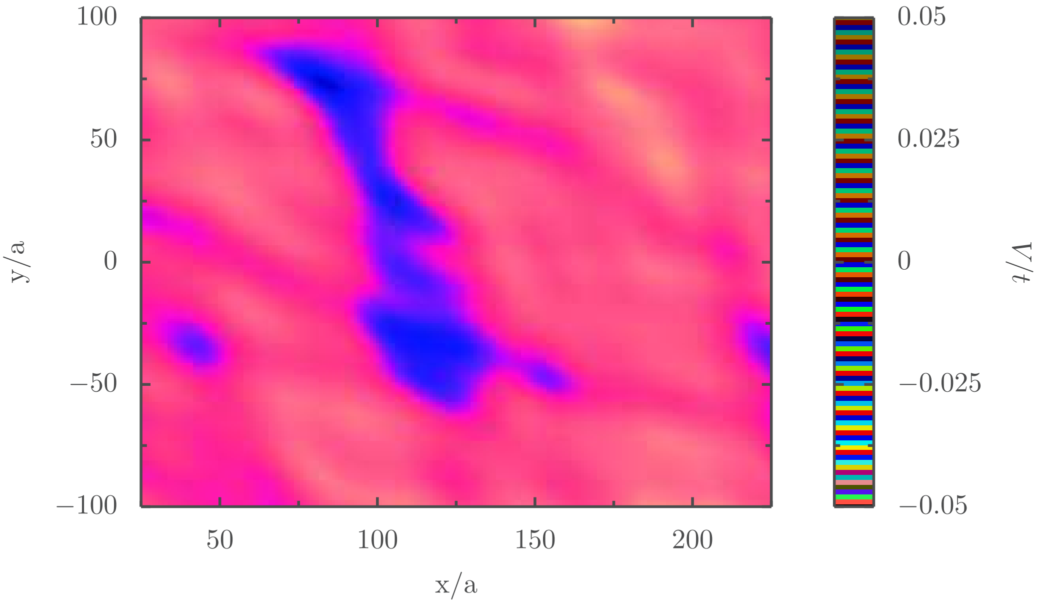

Figure 6.2: Electrostatic potential in the 2DEG resulting from the disorder configuration used in Fig. 6.1.

6.2 Correspondence between $g^{(2)}(\mathbf{r}_{\mathrm{T}})$ and PLDOS for perfect transmission

Symmetries have been shown to play a key role in the quest of identifying SGM maps with local properties [15]. In particular, for a four-fold symmetric QPC operating in the regime of perfect transmission, the conductance change induced by a non-invasive local tip in the absence of magnetic field has been shown to be proportional to the square of the LDOS, and also proportional to the local current density. In the same framework, it has been pointed out [67] that the correspondence with the PLDOS holds even for asymmetric QPCs, provided that the conductance is set to the first plateau, as long as the system remains time reversal invariant.

An important task, undertaken in this section, is the generalization of previous results to any conductance plateau of an arbitrary QPC under the sole assumptions of time-reversal symmetry and a local tip.

To describe transport within the Landauer formalism, the QPC can be treated as a scatterer centered at the origin $\mathbf{r} = 0$. With the definitions of Sec. 1.7 of Chapter 1, $\varphi^{(-)*}_{l,\varepsilon,m}(\mathbf{r}) = \varphi^{(+)}_{l,\varepsilon,m}(\mathbf{r})$, and $\varrho^{(-)*}_{l,\varepsilon,m}(\mathbf{r}) = \varrho^{(+)}_{l,\varepsilon,m}(\mathbf{r})$. Therefore, for perfectly transmitted modes with $\mathcal{R}_m = 0$,

$$\chi_{2,\varepsilon,m}(\mathbf{r}) = \chi^{*}_{1,\varepsilon,m}(\mathbf{r}) \tag{6.7}$$

in the 2DEG on both sides of the QPC. Using this relationship in the second order correction (3.28) leads to

$$\boxed{g^{(2)}(\mathbf{r}_\mathrm{T}) = -\rho^2_{1\varepsilon_\mathrm{F}}(\mathbf{r}_\mathrm{T})} \tag{6.8}$$

for $\mathbf{r}_\mathrm{T}$ on the right hand side of the QPC. Unlike the relation for the first step, which is linear and fringed, perfect transmission on any plateau leads to a quadratic dependence on the PLDOS without fringing. Therefore, the conductance change due to a local tip on a plateau is unambiguously related to the square of the PLDOS. Interestingly, no spatial symmetry is required for the correspondence in the considered regime of conductance quantization. Nevertheless, a perfect conductance quantization with exact unit transmission is a regime difficult to reach in experiments with real QPCs.

6.3 $g^{(2)}(\mathbf{r}_\mathrm{T})$ versus PLDOS near perfect transmission

In Sec. 6.2 perfect transmission is assumed in order to establish the correspondence between the second order conductance correction and the PLDOS. Here that condition is relaxed. Beyond the unity case of perfect conductance quantization where all $\mathcal{R}_m = 0$, the first-order correction (6.4) is nonzero, and all terms of the second-order correction $g^{(2)}$ in (11.11) and (3.27) must be considered.

Begin with the situation of transmission slightly below the unity case on the M^th conductance plateau, where the transmission of the highest open channel M is not perfect. The expressions of the scattering eigenstates provided by (1.37) can be used to find that

$$\chi_{2,\varepsilon,m}(\mathbf{r}) = \frac{1}{\mathcal{T}_m}\left(1 + \mathcal{R}_m e^{2i\alpha_{1,\varepsilon,m}(\mathbf{r})}\right)\chi^*_{1,\varepsilon,m}(\mathbf{r}) \tag{6.9}$$

on the RHS of a generic QPC. Here we aim at approximating the second order conductance correction $g^{(2)}$ to the lowest order in the reflection coefficient $\mathcal{R}_m$, assumed to be very small.

Starting from (11.11) and (3.27) the second order conductance correction

$g^{(2)}$ can be written as

$$\begin{aligned} g^{(2)} &= 4\pi^2 \sum_{mm'} \{\mathcal{R}_m^2 |\chi_{1,\varepsilon_{\mathrm{F}},m'}(\mathbf{r})|^2 |\chi_{2,\varepsilon_{\mathrm{F}},m}(\mathbf{r})|^2 - \mathcal{T}_m^2 |\chi_{1,\varepsilon_{\mathrm{F}},m}(\mathbf{r})|^2 |\chi_{2,\varepsilon_{\mathrm{F}},m'}(\mathbf{r})|^2\} \\ &+ 4\pi^2 \sum_{mm'} \mathcal{R}_m \mathcal{T}_m \mathrm{Re}\{\chi^*_{2,\varepsilon_{\mathrm{F}},m}(\mathbf{r})\chi_{1,\varepsilon_{\mathrm{F}},m}(\mathbf{r})\}(|\chi_{2,\varepsilon_{\mathrm{F}},m'}(\mathbf{r})|^2 - |\chi_{1,\varepsilon_{\mathrm{F}},m'}(\mathbf{r})|^2) \\ &- 4\pi \sum_{m} \mathcal{R}_m \mathcal{T}_m \mathrm{Im}\{\chi^*_{2,\varepsilon_{\mathrm{F}},m}(\mathbf{r})\chi_{1,\varepsilon_{\mathrm{F}},m}(\mathbf{r})\} \mathcal{P}\int_{\varepsilon_1^{\mathrm{t}}}^{\infty} \frac{\mathrm{d}\bar{\varepsilon}}{\bar{\varepsilon}-\varepsilon_{\mathrm{F}}} \rho_{\bar{\varepsilon}}(\mathbf{r}). \end{aligned} \tag{6.10}$$

In order to approximate $g^{(2)}$ for a tip on the RHS of the QPC, let us write it in terms of the PLDOS from the left ρ_1, expressing all the χ_2's in terms of χ_1. According to (6.9)

$$|\chi_{2,\varepsilon_{\mathrm{F}},m}(\mathbf{r})|^2 = \frac{|\chi_{1,\varepsilon_{\mathrm{F}},m}(\mathbf{r})|^2}{1-\mathcal{R}_m^2}(1+\mathcal{R}_m^2 + 2\mathcal{R}_m \cos 2\alpha_{1,\varepsilon_{\mathrm{F}},m}(\mathbf{r})). \tag{6.11}$$

On the other hand

$$\chi^*_{2,\varepsilon_{\mathrm{F}},m}(\mathbf{r})\chi_{1,\varepsilon_{\mathrm{F}},m}(\mathbf{r}) = \frac{\chi^2_{1,\varepsilon_{\mathrm{F}},m}(\mathbf{r})}{\sqrt{1-\mathcal{R}_m^2}}(1+\mathcal{R}_m e^{-2i\alpha_{1,\varepsilon_{\mathrm{F}},m}(\mathbf{r})}). \tag{6.12}$$

Thus, the real and imaginary parts of $\chi^*_{2,\varepsilon_{\mathrm{F}},m}(\mathbf{r})\chi_{1,\varepsilon_{\mathrm{F}},m}(\mathbf{r})$ appearing in the two last terms of (6.10) read

$$\begin{aligned} \mathrm{Re}\{\chi^*_{2,\varepsilon_{\mathrm{F}},m}(\mathbf{r})\chi_{1,\varepsilon_{\mathrm{F}},m}(\mathbf{r})\} &= \frac{|\chi_{1,\varepsilon_{\mathrm{F}},m}(\mathbf{r})|^2}{\sqrt{1-\mathcal{R}_m^2}}(\cos 2\alpha_{1,\varepsilon_{\mathrm{F}},m}(\mathbf{r}) + \mathcal{R}_m), \\ \mathrm{Im}\{\chi^*_{2,\varepsilon_{\mathrm{F}},m}(\mathbf{r})\chi_{1,\varepsilon_{\mathrm{F}},m}(\mathbf{r})\} &= \frac{|\chi_{1,\varepsilon_{\mathrm{F}},m}(\mathbf{r})|^2}{\sqrt{1-\mathcal{R}_m^2}} \sin 2\alpha_{1,\varepsilon_{\mathrm{F}},m}(\mathbf{r}). \end{aligned} \tag{6.13}$$

Inserting (6.11) and (6.13) into (6.10), and only keeping the lowest order terms in $\mathcal{R}_m$, $g^{(2)}$ reads

$$\begin{aligned} g^{(2)}(\mathbf{r}_{\mathrm{T}}) = -2\pi\rho_{1\varepsilon_{\mathrm{F}}}(\mathbf{r}_{\mathrm{T}}) \sum_{m=1}^{M} |\chi_{1,\varepsilon_{\mathrm{F}},m}(\mathbf{r}_{\mathrm{T}})|^2 \Bigg\{ 1 + 2\mathcal{R}_m \Bigg\{ &\cos\left[2\alpha_{1,\varepsilon_{\mathrm{F}},m}(\mathbf{r}_{\mathrm{T}})\right] \\ &+ \eta_{\varepsilon_{\mathrm{F}}} \sin\left[2\alpha_{1,\varepsilon_{\mathrm{F}},m}(\mathbf{r}_{\mathrm{T}})\right] \Bigg\}\Bigg\}, \end{aligned} \tag{6.14}$$

where

$$\eta_{\varepsilon_{\mathrm{F}}} = \eta_{\varepsilon_{\mathrm{F}}}(\mathbf{r}_{\mathrm{T}}) = \frac{1}{\pi}\mathcal{P}\int_{\varepsilon_1^{\mathrm{t}}}^{\infty} \frac{\mathrm{d}\bar{\varepsilon}}{\bar{\varepsilon}-\varepsilon_{\mathrm{F}}} \frac{\rho_{\bar{\varepsilon}}(\mathbf{r}_{\mathrm{T}})}{2\rho_{1\varepsilon_{\mathrm{F}}}(\mathbf{r}_{\mathrm{T}})} \tag{6.15}$$

for positions $\mathbf{r}$ on the RHS of the QPC. Notice that the relation of the LDOS to the imaginary part of the diagonal Green function $\mathcal{G}_{\varepsilon}(\mathbf{r},\mathbf{r})$ implies $\eta_{\varepsilon_{\mathrm{F}}}(\mathbf{r}) = -\mathrm{Re}[\mathcal{G}_{\varepsilon_{\mathrm{F}}}(\mathbf{r},\mathbf{r})]/(2\pi\rho_{1\varepsilon_{\mathrm{F}}}(\mathbf{r}))$. Taking $\mathcal{R}_m = 0$ for all $m < M$ gives

$$g^{(2)}(\mathbf{r}_{\mathrm{T}}) = -\rho^2_{1\varepsilon_{\mathrm{F}}}(\mathbf{r}_{\mathrm{T}}) - 4\pi\mathcal{R}_M\rho_{1\varepsilon_{\mathrm{F}}}(\mathbf{r}_{\mathrm{T}})|\chi_{1,\varepsilon_{\mathrm{F}},M}(\mathbf{r}_{\mathrm{T}})|^2\Big\{\cos\left[2\alpha_{1,\varepsilon_{\mathrm{F}},M}(\mathbf{r}_{\mathrm{T}})\right] + \eta_{\varepsilon_{\mathrm{F}}}\sin\left[2\alpha_{1,\varepsilon_{\mathrm{F}},M}(\mathbf{r}_{\mathrm{T}})\right]\Big\}, \tag{6.16}$$

and the small reflection amplitude is linked to the deviation from unit conductance by $\Delta g = \mathcal{R}_M^2$, where $\Delta g = M - g^{(0)}$ quantifies the departure from unit transmission on the M^{th} plateau. In the case of unit transmission we have $\mathcal{R}_M = 0$, and (6.16) reduces to (6.8). For completeness, in the same regime Eq. (6.6) can be rewritten as

$$g^{(1)}(\mathbf{r}_{\mathrm{T}}) = 4\pi\mathcal{R}_M|\chi_{1,\varepsilon_{\mathrm{F}},M}(\mathbf{r}_{\mathrm{T}})|^2\sin[2\alpha_{1,\varepsilon,M}(\mathbf{r}_{\mathrm{T}})]\ , \tag{6.17}$$

which has similarities in its form with respect to the correction terms for $g^{(2)}(\mathbf{r}_{\mathrm{T}})$. Recall however, the corresponding conductance correction varies linearly with the strength of the tip potential unlike for $g^{(2)}(\mathbf{r}_{\mathrm{T}})$.

In the case of transmission just above the unity case, with low transmission $\mathcal{T}_{M+1}$ through the QPC for the mode $M+1$, a similar procedure can be used. Assuming $\mathcal{R}_m = 0$ for all $m \leq M$ and keeping only the lowest terms in $\mathcal{T}_{M+1}$ yields

$$\begin{aligned} g^{(2)}(\mathbf{r}_{\mathrm{T}}) \;=\; & -\rho^2_{1\varepsilon_{\mathrm{F}}}(\mathbf{r}_{\mathrm{T}}) + 2\pi\mathcal{T}^2_{M+1}\left|\varrho^{(-)}_{2,\varepsilon_{\mathrm{F}},M+1}(\mathbf{r}_{\mathrm{T}})\right|^2 \\ \times\; & \Big\{\rho_{1\varepsilon_{\mathrm{F}}}(\mathbf{r}_{\mathrm{T}}) + 4\pi\left|\varrho^{(-)}_{2,\varepsilon_{\mathrm{F}},M+1}(\mathbf{r}_{\mathrm{T}})\right|^2\left(1+\cos\left[2\alpha_{1,\varepsilon_{\mathrm{F}},M+1}(\mathbf{r}_{\mathrm{T}})\right]\right)^2 \\ -\; & 2\rho_{1\varepsilon_{\mathrm{F}}}(\mathbf{r}_{\mathrm{T}})\eta_{\varepsilon_{\mathrm{F}}}\sin\left[2\alpha_{1,\varepsilon_{\mathrm{F}},M+1}(\mathbf{r}_{\mathrm{T}})\right]\Big\}. \end{aligned} \tag{6.18}$$

The small transmission in the QPC channel $M+1$ causes departures from (6.8) that are expected to be proportional to $\mathcal{T}^2_{M+1}$.

However, in a real system slightly above integer dimensionless conductance, the small transmission of the $M+1^{\mathrm{st}}$ channel can coexist with an imperfect transmission of the M^{th} channel, $\Delta g = \mathcal{R}_M^2 - \mathcal{T}^2_{M+1}$, and the departure from (6.8) has contributions from both channels. To avoid this complication, we concentrate in the following on the case of positive Δg, at positions on the conductance plateau where the opening of the next channel is exponentially suppressed and thus negligible.

It is worth emphasizing a few features of the expressions contained in Eqs. (6.16, 6.17). The scale of the deviations from the square of the PLDOS is greatly magnified by being proportional to the square root of Δg, as opposed to the case that would be encountered if the departure were linear. In other words the approach to the perfect transmission case is rather slow with respect to the limit $\Delta g \to 0$, and even tiny imperfections produce highly visible deviations. Nevertheless, all the deviations oscillate around zero with a wavelength on the order of $\lambda_F/2$, and thus a spatial averaging over a region $\lambda_F/2 \times \lambda_F/2$ results in a near uniform distribution of angles α over 2π, giving a means for the near elimination of the correction terms in (6.16). Thus, though with reduced spatial resolution, it is still possible to extract the PLDOS. The PLDOS is not proportional to the LDOS in this case, and the distinction matters.

Furthermore, since the contribution of $g^{(1)}(\mathbf{r}_\mathrm{T})$ to $\delta g(\mathbf{r}_\mathrm{T})$ is linearly proportional to the tip strength v_T and the contribution of $g^{(2)}(\mathbf{r}_\mathrm{T})$ quadratic, measurements with two well chosen values of v_T would be sufficient to separate out the contributions from Eqs. (6.16, 6.17); with a few more tip strength measurements, noise and other inaccuracies could be overcome in the separation as well. In the event that $|\chi_{1,\varepsilon_\mathrm{F},M}(\mathbf{r}_\mathrm{T})|^2$ mostly varies slowly on the scale of λ_F, then probability densities due to individual eigenstates and the spatial behavior of α could be extracted as well. Given that $\eta(\mathbf{r})$ is related to the phase of the real part of the diagonal Green function, in an ideal situation, it could also be extracted.

In order to quantify the departures of $g^{(2)}(\mathbf{r}_\mathrm{T})$ from the perfect case, introduce the ratio between the coefficient of the second order SGM correction and the square of the PLDOS

$$\boxed{\kappa(\mathbf{r}_\mathrm{T}) = -\frac{g^{(2)}(\mathbf{r}_\mathrm{T})}{\rho^2_{1\varepsilon_\mathrm{F}}(\mathbf{r}_\mathrm{T})}} \tag{6.19}$$

If the unperturbed conductance $g^{(0)}$ is just below that of $M = 1$, and the sum over QPC eigenmodes is restricted to $m = 1$, then

$$\boxed{\kappa(\mathbf{r}) = 1 + 2\sqrt{\Delta g}\,\{\cos[2\alpha(\mathbf{r})] + \eta(\mathbf{r})\sin[2\alpha(\mathbf{r})]\}} \tag{6.20}$$

The indices of α and η are omitted; it is understood that $\alpha = \alpha_{1,\varepsilon_\mathrm{F},1}$ and $\eta = \eta_{\varepsilon_\mathrm{F}}$.

As mentioned above, even fairly local spatial averaging approximately yields $\overline{\kappa} = \langle\kappa(\mathbf{r})\rangle = 1$. Interest is therefore in the quantity $\kappa - 1$. Similar to the case of the first-order SGM correction at a conductance step, discussed in Sec. (6.1), the above relationship provides bounds for the possible values of the ratio κ,

$$|\kappa - 1| \leq 2\sqrt{\Delta g}\sqrt{1+\eta_\mathrm{max}^2}\,, \tag{6.21}$$

where η_max is the maximum value of $|\eta(\mathbf{r})|$. A priori, η_max is not known, but if not extracted as described, it can be obtained by direct numerical computation of the scattering wave-functions (see Sec. (6.4)) or estimated from simple setups, like that of an abrupt QPC, where the analytical form of the scattering wave-functions is known [15]. The maximum value of η occurs in regions where the PLDOS is weak, and can in general approach infinity. Its actual value depends on the problem and region under consideration. In one numerical example given ahead, its maximum is of the order of 60.

Another interesting quantity is the variance of $\kappa - 1$ given by

$$\boxed{\sigma^2 = 2\Delta g(1+\overline{\eta^2})} \tag{6.22}$$

where $\overline{\eta^2}$ is the average value of η^2 in the scan region.

6.4 $g^{(2)}(\mathbf{r}_\mathrm{T})$ versus PLDOS for local tips : simulations

In order to test our analytical approach and go beyond the above described perturbation theory we performed numerical simulations using the quantum transport package KWANT [30] introduced in chapter 1. From Kwant, one can calculate $\delta g(\mathbf{r})$ as a direct subtraction, and $g^{(1)}(\mathbf{r}_\mathrm{T})$ or $g^{(2)}(\mathbf{r}_\mathrm{T})$ by constructing numerical derivatives with respect to v_T.

We chose an abrupt constriction defined by a hard-walled square well of width $w = 11a$ and length $L = 19a$ attached to two semi-infinite leads, sketched in the inset of Fig. 6.3. In order to optimize the computational time the left lead is narrowed. Fig. 6.3 shows the dimensionless conductance through the QPC as a function of the Fermi energy of the incoming electrons. As the latter is increased the QPC's conductance increases in steps of unit height. The structures on the plateaus are due to the abruptness of the QPC that lead to Fabry-Perot like oscillations within the constriction [24].

6.4.1 Local correspondence for perfect transmission

In order to address this regime, consider the analytically predicted relationship (6.8) between the second-order conductance correction $g^{(2)}(\mathbf{r}_\mathrm{T})$ for a δ-tip and the PLDOS for perfect conductance. On the tight binding lattice

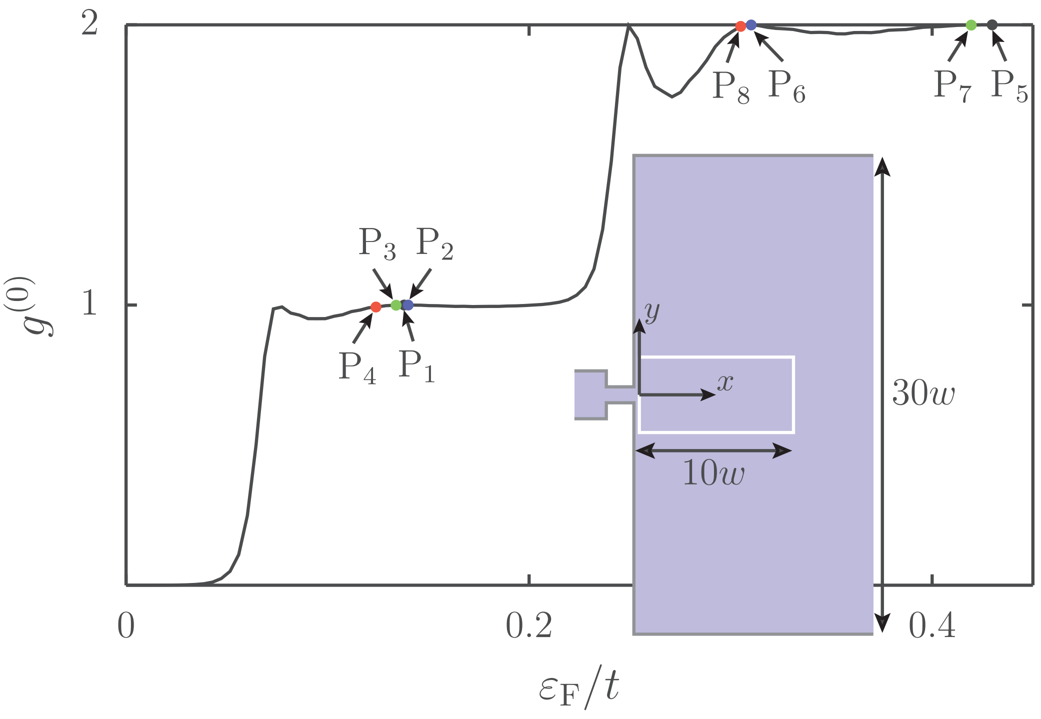

Figure 6.3: The conductance of the QPC defined in a tight binding lattice with lattice parameter a and hopping t as a function of Fermi energy. The inset shows the geometry of the QPC. The width and length of the narrow channel are $w = 11a$ and $L = 19a$, respectively. The points P$_1$–P$_8$ indicate the Fermi energies and unperturbed conductances at which the statistics of Sec. 6.4 have been performed using tip positions inside the dashed white rectangle.

with lattice parameter a, the δ-tip is modeled as an additional on-site energy ε_T on a single site, corresponding to a tip area of a^2 and thus $v_\mathrm{T} = \varepsilon_\mathrm{T} a^2$. This strength is varied so as to extract $g^{(2)}(\mathbf{r}_\mathrm{T})$. The Fermi energies are chosen on the first and second plateaus for which the values of the unperturbed conductances $g^{(0)}$ are very close to perfect transmission with $|\Delta g| < 10^{-5}$ (points P_1 and P_5 in Fig. 6.3). The corresponding Fermi wavelengths are $\lambda_\mathrm{F} = 16.8a$ and $\lambda_\mathrm{F} = 9.4a$, respectively. The resultant conductance responses are shown in Fig. 6.4, where $g^{(2)}(\mathbf{r}_\mathrm{T})$ is compared to $-\rho^2_{1\varepsilon_\mathrm{F}}$ for the first plateau case in panels (a) and (b) and likewise for the second plateau case in panels (d) and (e). The correspondence is excellent as expected given the regime of the calculation. This is illustrated in panels (c) and (f), which show the differences, $\left[\rho^2_{1\varepsilon_\mathrm{F}} + g^{(2)}(\mathbf{r}_\mathrm{T})\right]$, respectively, for the two plateaus. The differences are quite small as is expected and they show the $\lambda_\mathrm{F}/2$ oscillations, which are characteristic of the correction terms for imperfect transmission.

6.4.2 Departures from local correspondence for imperfect transmission

It is shown in Sec. 6.3 that the precise local correspondence between the second-order SGM correction and the PLDOS squared degrades away from perfect transmission. We now present a quantitative numerical analysis of the departure from local correspondence for the example of the second conductance plateau of the QPC. Similar results can be obtained on other plateaus. Fig. 6.5 presents the values of $g^{(2)}(\mathbf{r}_\mathrm{T})$ and $\rho^2_{1\varepsilon_\mathrm{F}}$ at different points of the scanned region inside the white dashed rectangle shown in the inset of Fig. 6.3. The region of length $10w$ has been chosen so as to contain points close to the QPC and at larger distances. This region width is small as compared to the width of the 2DEG ($30w$), and additional lateral leads on the full length of the right hand side are used in order to avoid finite size effects.

The data shown in Fig. 6.5 confirm that the exact point-by-point local correspondence is progressively broken as $|\Delta g|$ increases. Close to the perfect transmission condition, for the case with $\Delta g = 8 \times 10^{-6}$ (P_5 in Fig. 6.3 with scans depicted in the lower panels of Fig. 6.4), the equivalence between $-g^{(2)}(\mathbf{r}_\mathrm{T})$ and the square of the PLDOS is attained (black dots). For other points of the unperturbed conductance shown in Fig. 6.3, P_6 with $\Delta g = 5 \times 10^{-4}$ (blue), P_7 with 10^{-3} (green) and P_8 with 6×10^{-3} (red), the sampled points exhibit progressively wider distributions around the equivalence (6.8). The distributions are displayed in Fig. (6.6), where $\kappa - 1$ is plotted for different Fermi energies on the first plateau (P_1, P_2, P_3, and P_4 in Fig. 6.3), labeled by the value of Δg. In agreement with our analytical findings of the previous

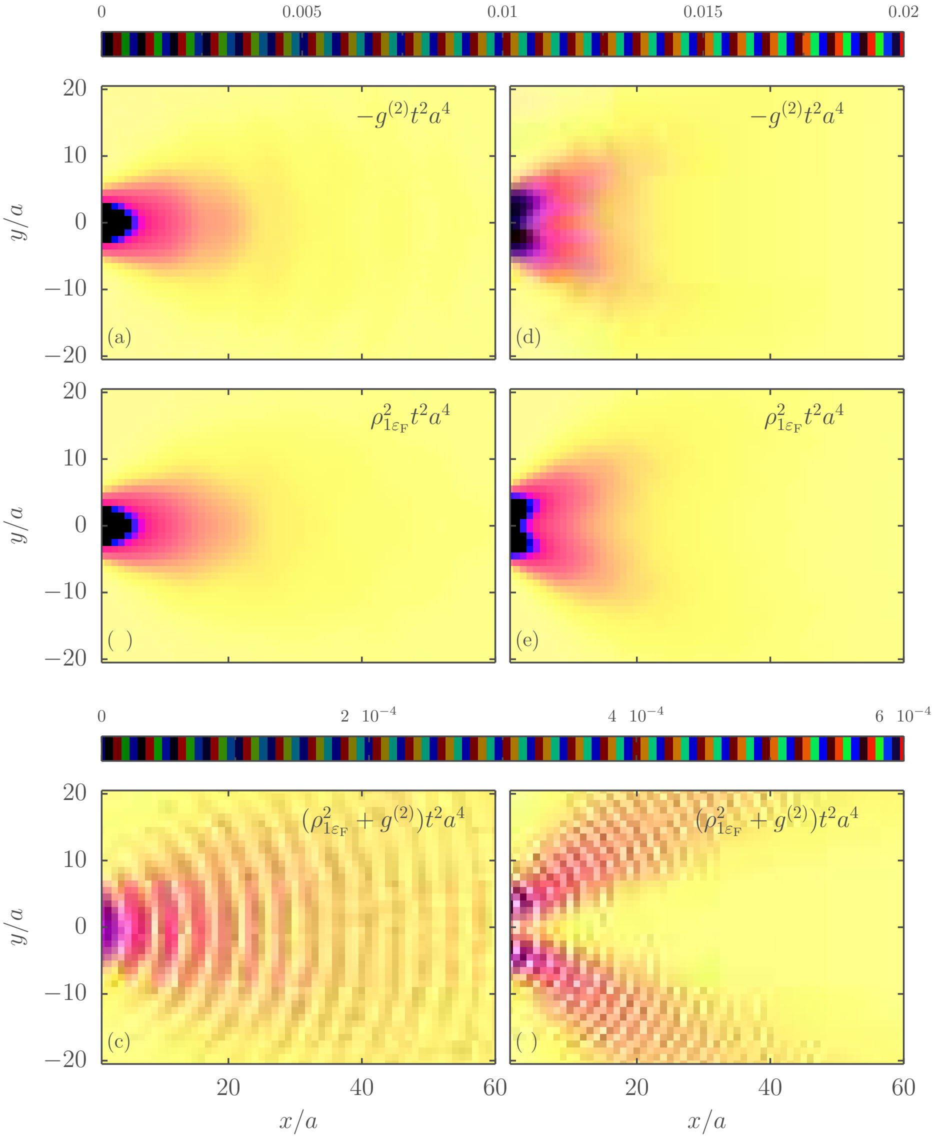

Figure 6.4: Upper row : $-g^{(2)}$ (with the energy and length units introduced through the hopping integral t and the spatial tip extension a^2) *vs.* the tip position for the first (a) and second (d) plateaus (points P_1 and P_5 in Fig. 6.3, respectively) Central row: the square of the PLDOS for the same points on the first (b) and second (e) plateau. Last row: difference between the two first rows. The QPC is situated at the left side of the figures.

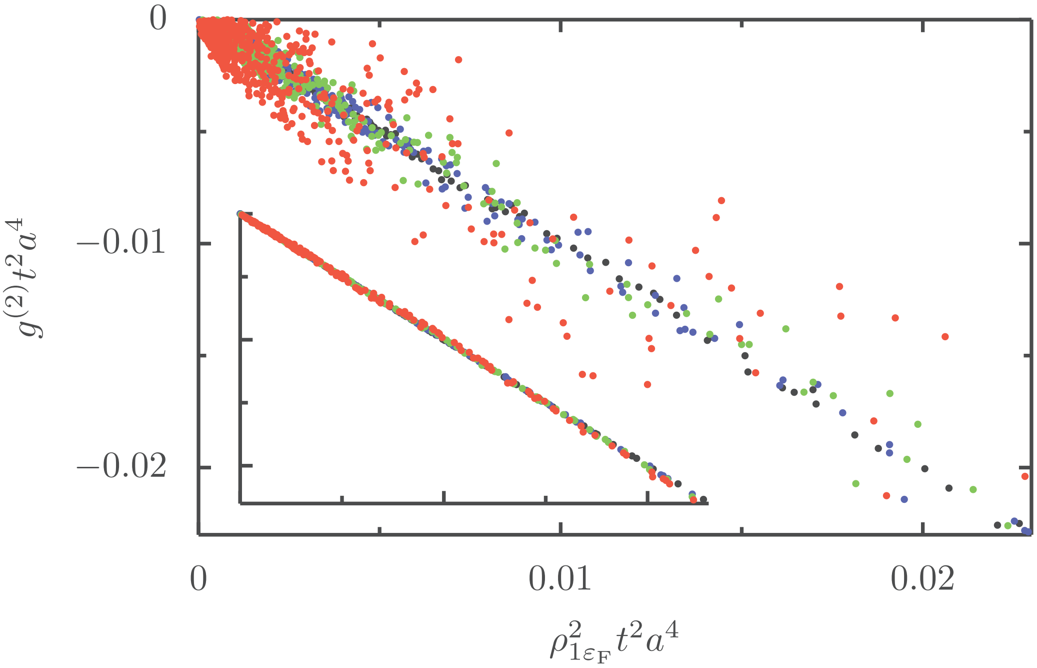

Figure 6.5: Second order SGM correction *vs.* $\rho^2_{1\varepsilon_\mathrm{F}}$ at random sampled tip positions in the scanned region for different values of the unperturbed conductance on the second plateau (points P_5, P_6, P_7, and P_8 in Fig. 6.3). The corresponding departures from the quantized value are $\Delta g = 8 \times 10^{-6}$, 5×10^{-4}, 10^{-3}, and 6×10^{-3} for the black, blue, green and red points, respectively. Inset: the same data are presented after a spatial average over a disc of radius of $\lambda_\mathrm{F}/2$, exhibiting a clear data collapse.

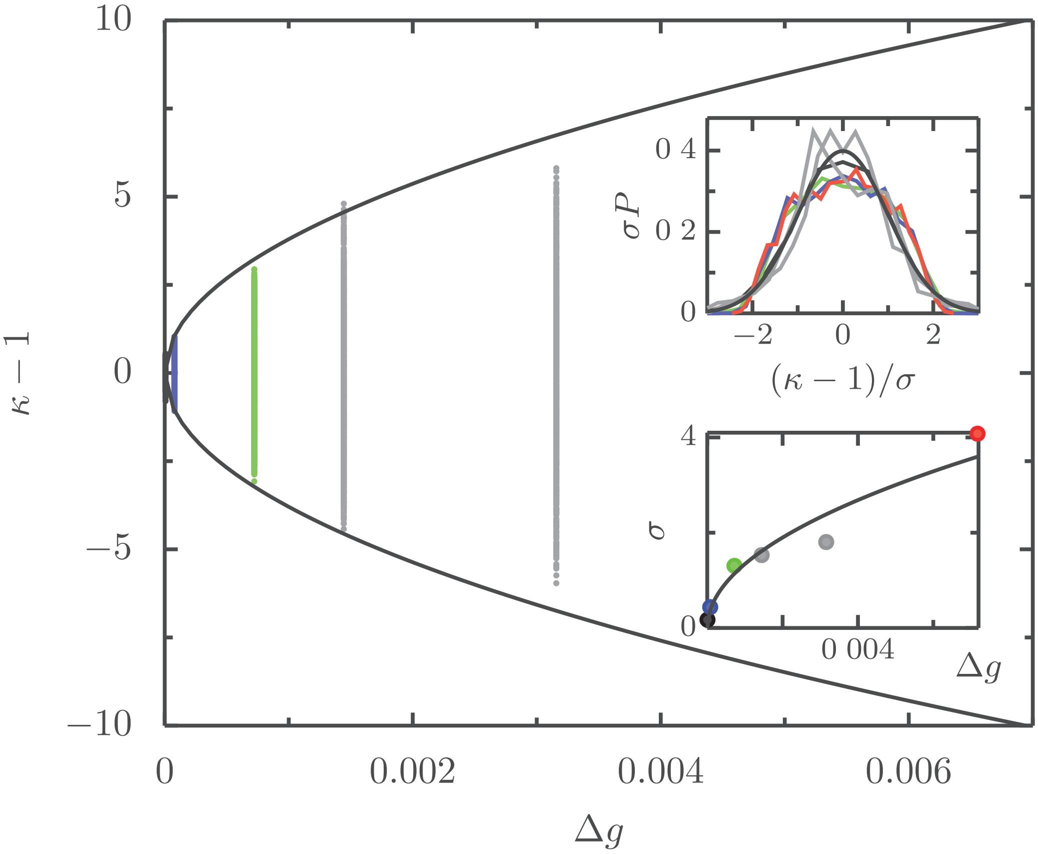

Figure 6.6: $\kappa - 1$ is plotted *vs.* the departure from perfect transmission Δg, when a wide region in the right side of the QPC is sampled. The results for the clean structure of Figs. 6.4 and 6.5, $\Delta g = 6 \times 10^{-6}$ (black; P_1 in Fig. 6.3), $\Delta g = 8 \times 10^{-5}$ (blue; P_2), 7×10^{-4} (green; P_3) are presented, but those for $\Delta g = 7 \times 10^{-3}$ (red; P_4) are out of the scale of the main figure. The data corresponding to two different disorder configurations are represented by the grey distributions. The black solid lines show the analytical bounds $\kappa_\pm$ of Eq. (6.21) taking $\eta_\mathrm{max} = 60$. Upper inset: the probability density of $\kappa - 1$. The color code is the same as in the main figure. For comparison, the dotted line shows a Gaussian probability density. Lower inset: the corresponding standard deviation *vs.* Δg. The black solid line corresponds to the analytical expression 6.22 of σ with $\overline{\eta^2} = (\eta_\mathrm{max}/2)^2$.

section, the average value of κ remains equal to one, but the width of the distribution drastically increases with Δg within the bounds $\kappa_\pm$ established in Eq. 6.21 (solid lines) using the value $\eta_\mathrm{max} = 60$ of the abrupt QPC.

The probability density of $(\kappa - 1)/\sigma$ is shown in the upper inset of Fig. 6.6, for the same positions on the first conductance plateau. The rescaling by the variance collapses the probability densities for all the values of Δg to approximately a universal Gaussian form (dotted line). The analytical result of 6.22 for the standard deviation σ of the ratio κ from its mean value ($\kappa = 1$), is evaluated using the assumption $\overline{\eta^2} = (\eta_\mathrm{max}/2)^2$, and is shown to agree with the numerical results (lower inset of Fig. 6.6).

The possible connection of SGM response with local properties needs to be extended to the realistic situation where the QPC is surrounded by a disordered 2DEG. Though it is difficult to treat this case analytically because the asymptotic form of the scattering wave-functions is attained only beyond the region of disorder far from the QPC, the incorporation of disorder in the numerically tackled model is straightforward. We assume the disorder to be due to randomly distributed donor atoms in a plane situated at a distance $z = 10a$, with a concentration of $N_d = 4 \times 10^{-4} a^{-2}$. By taking $a = 5nm$, N_d is equal to $10^{12} cm^{-2}$, which is a realistic value for a high mobility 2DEG, and corresponds to elastic and transport mean free paths of $1\mu m$ and $52\mu m$, respectively. The two vertical gray lines in Fig. 6.6 correspond to samplings of different disorder configurations resulting in small departures from unit transmission, which are quantified by the values of Δg. Thus, disordered QPCs, as well as clean ones, have departures from the local relation between $-g^{(2)}(\mathbf{r}_\mathrm{T})$ and the PLDOS squared that are uniquely governed by the crucial parameter Δg.

6.4.3 Locally averaged correspondence for local tips

Sections 6.3 and 6.4.2 show that even small deviations from perfect conductance drastically alter the SGM-PLDOS correspondence. However, according to Eq. 6.20 and the calculations of the (Fig. 6.5) inset, the average of κ is equal to unity. The precise κ values though should fluctuate in a quasi-random way with a standard deviation scaling as the square root of Δg. Such a behavior is the signature of the $\lambda_\mathrm{F}/2$-wavelength oscillations in the SGM response occurring in the clean case, which is modified in the presence of disorder. Nevertheless, as discussed in Sect. 6.3, the oscillations should self cancel once averaged over a domain of length scale as short as $\lambda_\mathrm{F}/2$ in both directions of the plane. In order to verify this interpretation, the numerically obtained values are averaged over a disk of radius of $\lambda_\mathrm{F}/2$. As illustrated in the inset of Fig. 6.5, the averaging results in a data collapse yielding the

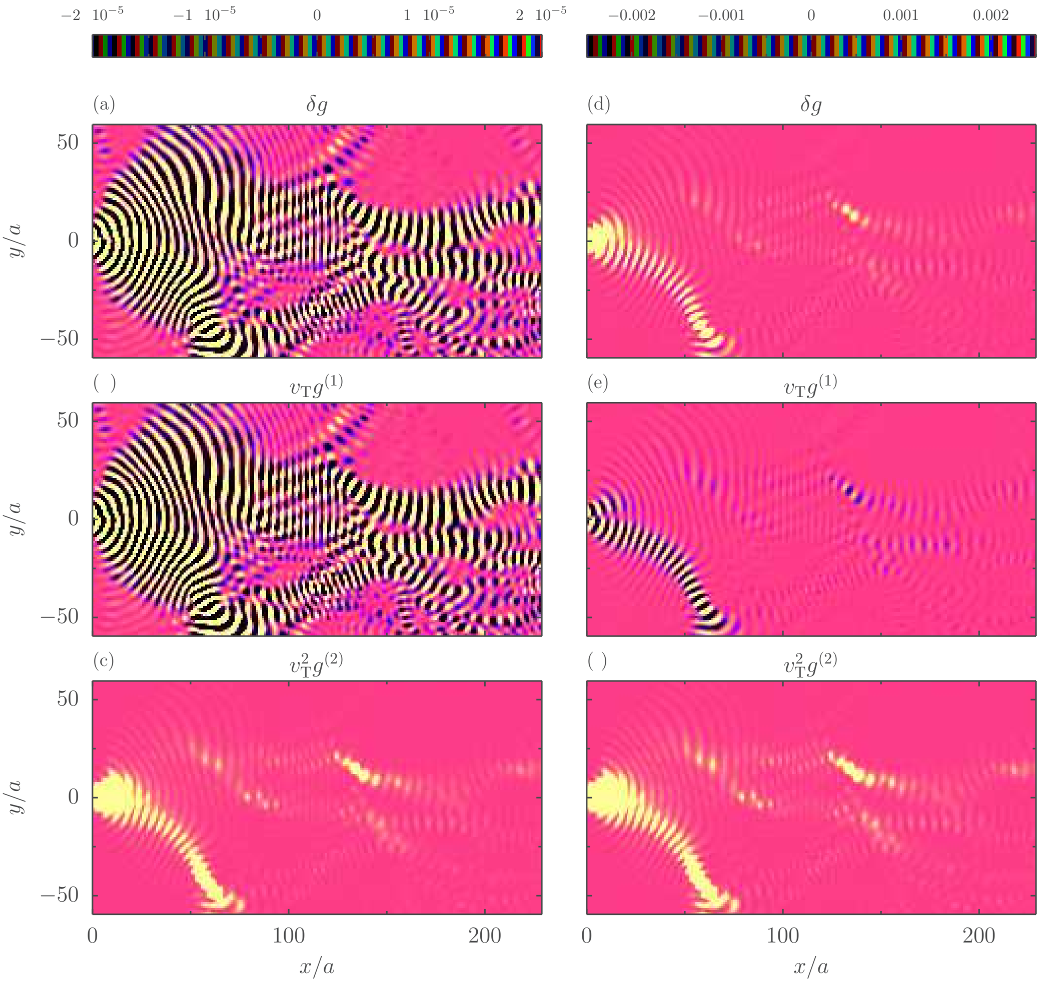

Figure 6.7: SGM response for two tip strengths, $v_{\mathrm{T}} = \varepsilon_{\mathrm{F}} a^2/4$ (left column) and $v_{\mathrm{T}} = 3\varepsilon_{\mathrm{F}} a^2$ (right column) with $\Delta g = 1.3 \times 10^{-4}$ on the second conductance plateau of a QPC in a disordered 2DEG. The disorder configuration is the same as in Sec. 6.1, but the strength is increased by a factor of 10. Ordered vertically for each case, the quantities plotted are: full response $\delta g(\mathbf{r}_{\mathrm{T}})$, first correction $g^{(1)}(\mathbf{r}_{\mathrm{T}})$, and second correction $g^{(2)}(\mathbf{r}_{\mathrm{T}})$. The changing nature and relative balance of the different order terms is clearly visible. The weaker tip strength is expected to be dominated by the first order term in the left column, but not so for the stronger tip strength in the right column.

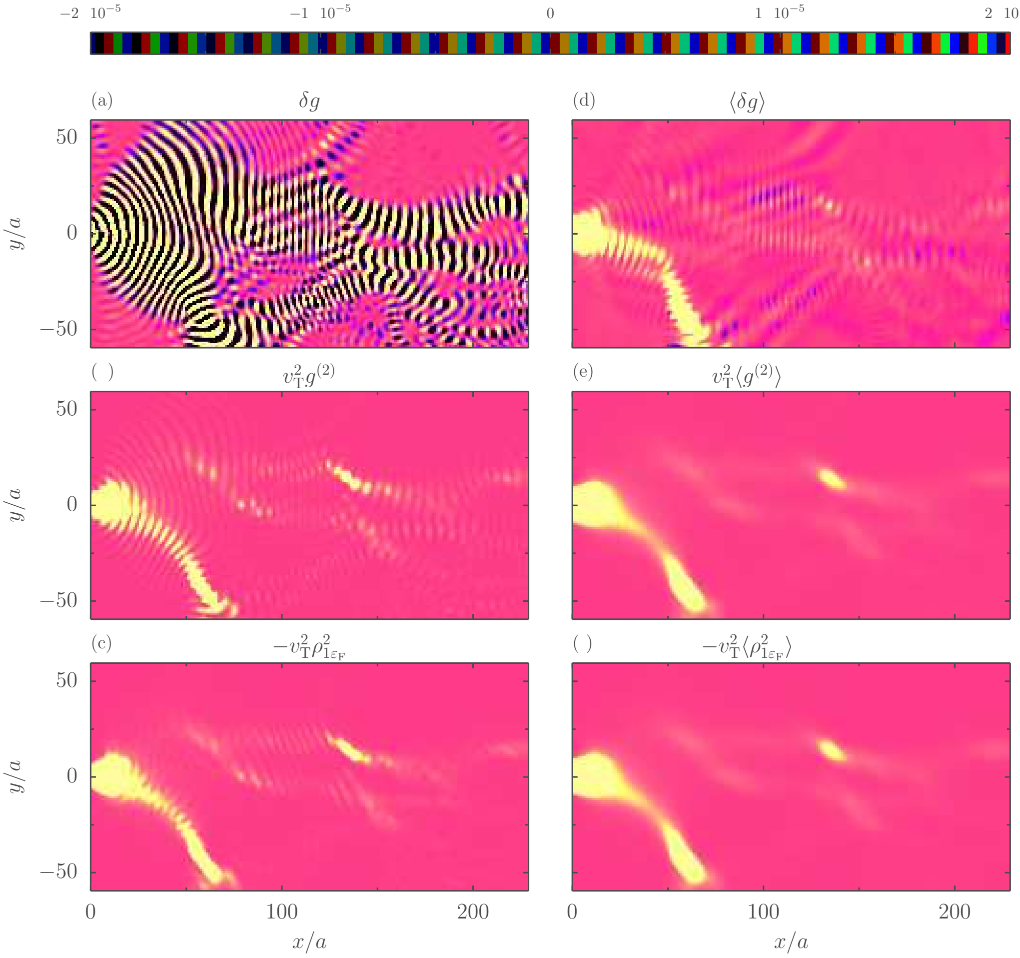

Figure 6.8: Extracting an accurate PLDOS squared from the full SGM response in the weakly invasive regime for the disorder configuration of Fig. 6.7, for the weaker tip strength $v_\mathrm{T} = \varepsilon_\mathrm{F} a^2/4$: (a) $\delta g(\mathbf{r}_\mathrm{T})$ on the right side of the QPC ; (b) the quadratic tip dependence portion of $\delta g(\mathbf{r}_\mathrm{T})$; (c) the negative of the squared PLDOS, $-\rho_{1\varepsilon_\mathrm{F}}^2$. In (d), (e), and (f), respectively, the data of panels (a), (b), and (c) have been averaged over a disc of radius $\lambda_\mathrm{F}/2$.

equivalence between $\langle -g^{(2)}(\mathbf{r}_\mathrm{T})\rangle$ and $\langle \rho^2_{1\varepsilon_\mathrm{F}}(\mathbf{r}_\mathrm{T})\rangle$, even in the case of imperfect unit transmission. The recovery of the SGM-PLDOS correspondence upon averaging shows that there is a global structural correspondence with a characteristic length scale given by the Fermi wavelength. However, this correspondence is found for a local tip and only between the PLDOS squared and the second order correction.

A finite temperature also has a tendency to reduce the fringes with period $\lambda_\mathrm{F}/2$ that are the main deviations from the SGM-PLDOS correspondence. Though the related mechanism is an energy average, very different from the spatial average proposed above, it might still be possible that a moderate temperature helps to improve the extraction of the PLDOS from SGM data.

6.5 Full SGM response for local tips

A priori, from an experimental point of view, the relationship between the various order terms and the full conductance change is not obvious. Even for weakly imperfect transmission somewhere on a plateau, depending on the tip strength, the full SGM response may depend not just on the leading second order term, but also crucially on the first and the other higher order terms. Thus, $\delta g(\mathbf{r}_\mathrm{T})$ can vary considerably as a function of the tip strength for less than perfect transmission cases, which would most often be the case in experiments. This is illustrated in Fig. 6.7, where $\delta g(\mathbf{r}_\mathrm{T}), g^{(1)}(\mathbf{r}_\mathrm{T}), g^{(2)}(\mathbf{r}_\mathrm{T})$ are plotted for two different tip strengths. The longer system treated here, in comparison with the simulations of Fig. 6.4, is numerically more demanding and thus the width of the 2DEG on the right hand side of the QPC is limited to $20w$. The specific example illustrated is on the second plateau of the quantized conductance where $\Delta g = 1.3 \times 10^{-4}$ using tip strengths of $v_\mathrm{T} = \varepsilon_\mathrm{F} a^2/4$ and $v_\mathrm{T} = 3\varepsilon_\mathrm{F} a^2$. The characteristic branching behavior of the fringes due to disorder [5] is observed. The changing nature of the full SGM response and its relationships with the linear and quadratic parts of the response are clearly seen.

Continuing to restrict ourselves to the weakly invasive regime, if the goal were to extract a local quantity, in this case, the square of the PLDOS, two operations would greatly enhance the quality of the analysis. The first is to make a few measurements with different tip strengths. Depending on the accuracy of the measurements or ambient noise, this would allow one to separate linear, quadratic, or even higher order variations with respect to tip strength. The quadratic dependent response is the one related to the PLDOS squared; see Eq. (6.16). Second, one would average the data over a region of sidelength or radius $\lambda_\mathrm{F}/2$. Consider the weak tip strength case illustrated

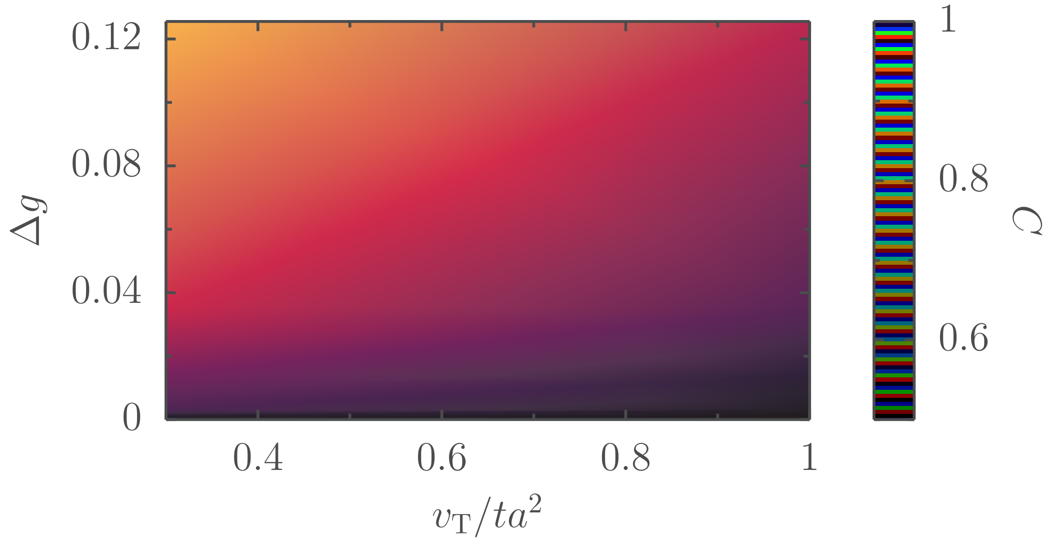

Figure 6.9: Cross-correlation factor (6.23) as a function of the strength v_{T} of a local tip (horizontal axis) and the deviation from perfect transmission (vertical axis), on the second conductance plateau of the QPC in a disordered 2DEG of Figs. 6.7 and 6.8.

in Fig. 6.7. There, the first order term dominates the full SGM response $\delta g(\mathbf{r}_{\mathrm{T}})$. Nevertheless, extracting first the quadratic tip dependent part of the full response before averaging leads to a much more accurate extraction of the PLDOS squared. This is illustrated in Fig. 6.8. In the first row, $\delta g(\mathbf{r}_{\mathrm{T}})$ is shown with its locally averaged image to the right. In the next row, the quadratic tip dependence is deduced first, and then averaged. Finally in the bottom row, the negative of the squared PLDOS is plotted along with its average. The improvement in the correspondence of the quadratic portion of $\delta g(\mathbf{r}_{\mathrm{T}})$ relative to the full response to the average PLDOS is quite striking.

The results shown in Fig. 6.8 demonstrate that the combined operations of extracting the quadratic tip dependence of $\delta g(\mathbf{r}_{\mathrm{T}})$ and $\lambda_{\mathrm{F}}/2$-averaging result in nearly perfect extraction of the PLDOS squared. Still, it is valuable to have a quantitative measure of the quality of this process to answer how well this works as a function of the imperfection of transmission on or near a plateau, and how well it works as a function of tip strength if one chooses just to use $\delta g(\mathbf{r}_{\mathrm{T}})$ without extracting the quadratic tip-dependence first. A good measure is given by the cross-correlation factor [55]

$$\boxed{C = \frac{\left|\overline{(\langle \delta g \rangle - \overline{\delta g})(\langle \rho^2 \rangle - \overline{\rho^2})}\right|}{\sigma_{\delta g}\sigma_{\rho^2}}} \tag{6.23}$$

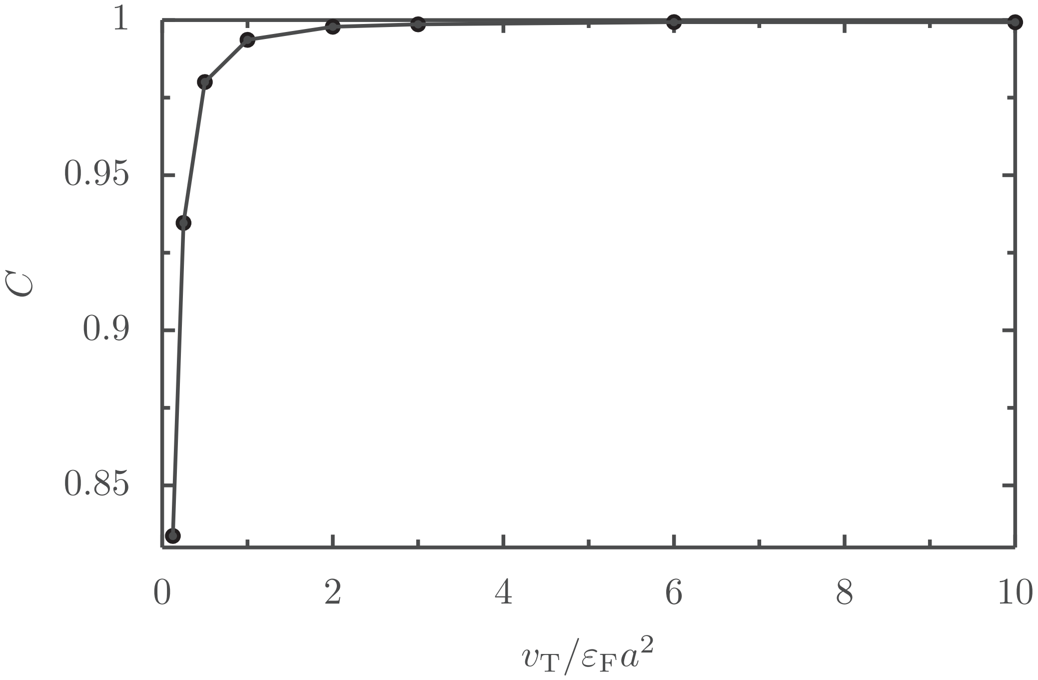

Figure 6.10: Cross-correlation factor C (6.23) *vs.* the strength of a local tip in the disordered system of Fig. 6.7.

The averages, symbolized by the overlines, are taken over the scanned area in the right of the QPC (in contradistinction to the local $O(\lambda_{\mathrm{F}}/2)$ averages, $\langle ... \rangle$, defined in Sec. 6.4). The standard deviations of the two quantities are the usual factors of a properly normalized correlation function. Applied to $\delta g(\mathbf{r}_{\mathrm{T}})$ for a range of tip strengths and Δg's gives the results shown in Fig. 6.9. It shows two correlated trends. The correlation coefficient decreases with decreasing tip strength and with increasing Δg. The value of v_{T} for which near perfect correlation is achieved depends on the departure Δg from perfect transmission. Fig. 6.10 shows an example for the case of the disordered system and tip strengths used in Fig. 6.7, where the saturation is reached rather quickly as v_{T}/a^2 increases beyond the Fermi energy.

Interestingly, the above dependence of $\delta g(\mathbf{r}_{\mathrm{T}})$ on the tip strength generates a criterion for the validity of perturbation theory [11]. Note that the criterion for the Born approximation in a one-dimensional scattering problem [71] $v_{\mathrm{T}} \ll \varepsilon_{\mathrm{F}}\lambda_{\mathrm{F}}$ is consistent with our numerical results since the linear extension of the local tip in our tight-binding model a is much smaller than λ_{F}. In this regime, close to the perfect transmission, the second order contribution prevails, and the full SGM response to a local tip is highly correlated to the PLDOS squared even for tip strengths larger than the Fermi energy.

Chapter 7

Full SGM response for non-local tips

In the previous chapter the SGM response to a local tip has been discussed. While the case of a local tip is the simplest to analyze, the existing experimental implementations of SGM setups involve extended tips. In this chapter we discuss the case of extended tips. Considering the tip as a point charge at a distance d from the 2DEG, the tip profile in the plane of the 2DEG is of the form

$$f(\mathbf{r}) = \frac{1}{2\pi d^2}\left[1+\left(\frac{\mathbf{r}-\mathbf{r}_{\mathrm{T}}}{d}\right)^2\right]^{-3/2} . \tag{7.1}$$

In Fig. 7.1 the SGM response is calculated for different tip profiles with the same depletion diameter $D = 20a$ that characterizes the size of the region in which the tip induced potential is bigger than the Fermi energy. While in (a) and (b) we have respectively used a Gaussian and a hard disc of diameter D to model the SGM tip, in (c) and (d) the profile 7.1 and a Lorentzian have been respectively considered. The prefactor of the tips has been fixed to $v_{\mathrm{T}} = 3\varepsilon_{\mathrm{F}} a^2$ and the parameter d has been adjusted to yield the same depletion diameter $D = 20a$.

As we can see from Fig. 7.1, the main features of the SGM map are mainly conserved for all tip models except at the QPC opening where the tails of the tips play an important role. This demonstrates that for tip strengths strong enough to produce a disk of depletion at the level of the 2DEG, the main feature determining the SGM response is the diameter D of such a disk, and the details of the tip profile are of lesser importance. We therefore adopt the tip profile (7.1) for the numerical simulations, where $D = 2d[\{v_{\mathrm{T}}/(2\pi d^2\varepsilon_{\mathrm{F}})\}^{2/3} - 1]^{1/2}$ is varied. Working in the previously established regime of strong tip strength (maximum tip potential $V_{\mathrm{T}}(\mathbf{r}_{\mathrm{T}}) = v_{\mathrm{T}}/(2\pi d^2) =$

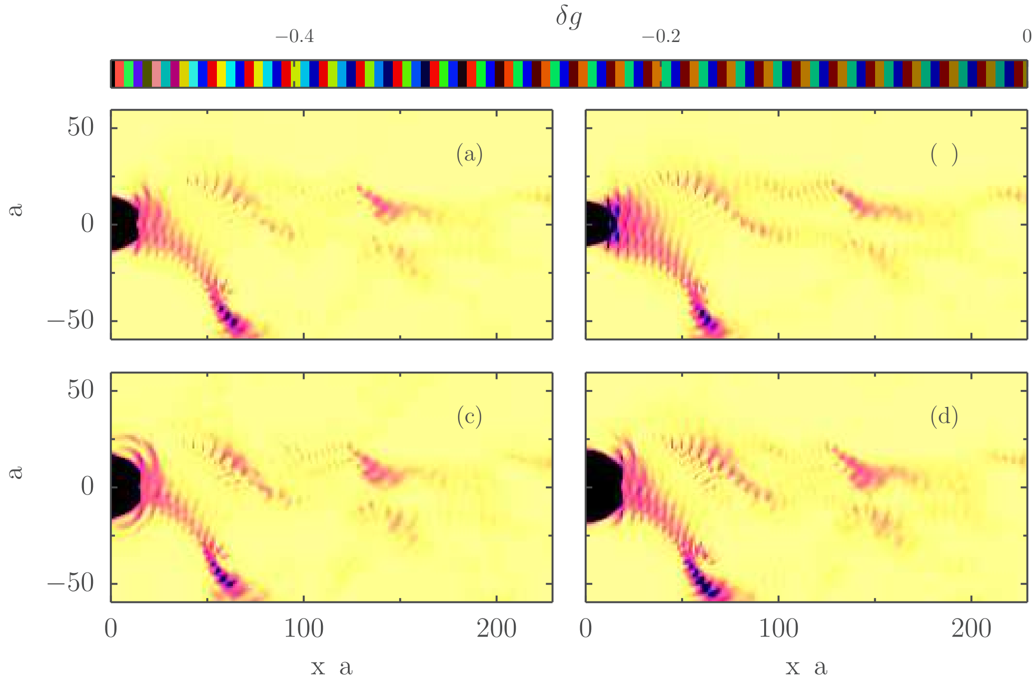

Figure 7.1: SGM response calculated using different tip shapes with the same depletion diameter $D = 20a$ and strength $v_{\mathrm{T}} = 3\varepsilon_{\mathrm{F}} a^2$. While in (a) a Gaussian profile $f(\mathbf{r}) = \frac{1}{2\pi d^2} e^{-\frac{(\mathbf{r}-\mathbf{r}_{\mathrm{T}})^2}{2d^2}}$ is used to model the tip, a hard disc of diameter D has been considered in the panel (b). Panels (c) and (d) show the results obtained using (7.1) and a Lorentzian form $f(\mathbf{r}) = \frac{1}{2\pi d^2}\left[1+\left(\frac{\mathbf{r}-\mathbf{r}_{\mathrm{T}}}{d}\right)^2\right]^{-1}$, respectively. The depletion diameter of the Gaussian and the Lorantzian tips are respectively given by $D = 2\sqrt{2}d\ln\{v_{\mathrm{T}}/(2\pi d^2\varepsilon_{\mathrm{F}})\}$ and $D = 2d[\{v_{\mathrm{T}}/(2\pi d^2\varepsilon_{\mathrm{F}})\} - 1]^{1/2}$.

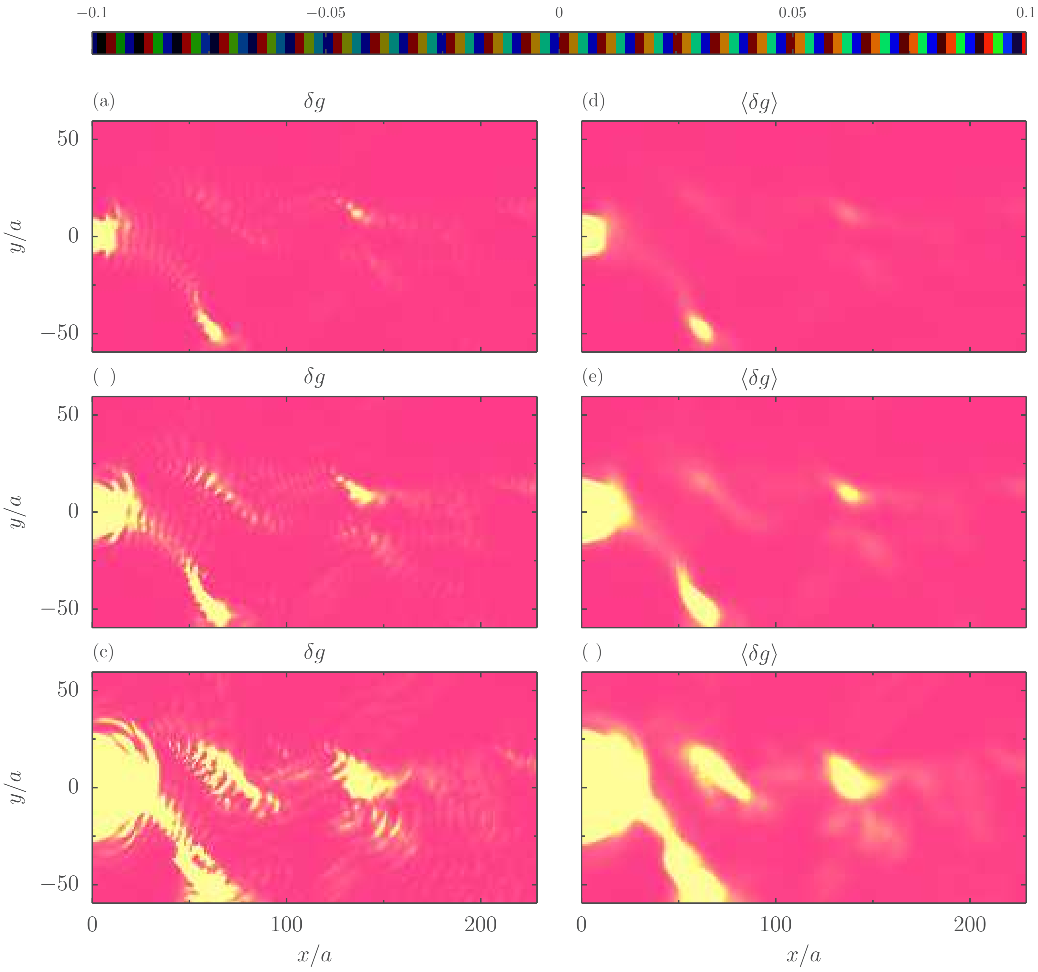

Figure 7.2: SGM response calculated using the tip shape (7.1) for fixed tip potential height $v_{\mathrm{T}}/(2\pi d^2) = 2\varepsilon_{\mathrm{F}}$ and varying depletion disk size $D = \lambda_{\mathrm{F}}/2$ (a), $D = \lambda_{\mathrm{F}}$ (b), and $D = 2\lambda_{\mathrm{F}}$ (c). Panels (d), (e), and (f) show the averages of the SGM responses over a disc of radius $\lambda_{\mathrm{F}}/2$ for the same tip sizes.

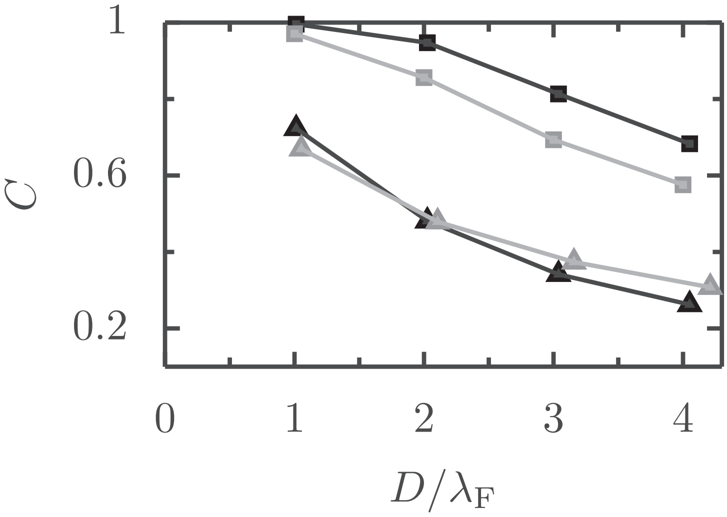

Figure 7.3: The cross correlation factor C (6.23) *vs.* the spatial tip-extension for the smooth extended tip shape (7.1) (grey symbols) and for a hard-disc tip (black symbols), in a disorder-free structure. Squares and triangles represent the correlation factor between the SGM response with the unperturbed PLDOS at the tip center and at the classical tuning points, respectively.

$2\varepsilon_{\mathrm{F}}$) the SGM response $\delta g(\mathbf{r}_{\mathrm{T}})$ for varying d and thus different depletion diameters D is present in Fig. 7.2, where the unperturbed conductance and the disorder configuration is the same as in Fig. 6.7 (second conductance plateau with $\Delta g = 1.3 \times 10^{-4}$).

For $D = \lambda_{\mathrm{F}}/2$ (panel (a)), the SGM scan resembles that of the δ-tip (panel (d) of Fig. 6.7), but with values of $\delta g(\mathbf{r}_{\mathrm{T}})$ that are one order of magnitude larger due to the tip extension. For larger tip extensions, $D = \lambda_{\mathrm{F}}$ (panel b) and $D = 2\lambda_{\mathrm{F}}$ (panel c), the SGM image gets more blurred and some resolution is lost. This blurring effect is more pronounced on the averaged conductance changes, as depicted in the right column panels of Fig. 7.2.

The Fig. 7.3 shows the cross-correlation C between the non-local SGM and the squared unperturbed PLDOS as a function of the depletion diameter D. Grey symbols correspond to the case of a tip shape of the form (7.1), the black ones to the case of a hard wall potential of diameter D. The squares represent cross-correlations of the SGM response with the PLDOS at the tip center, while triangles depict the results obtained when the PLDOS is taken at the classical turning points situated at the edge of the depletion disk. Since the classical turning point is not determined uniquely in the presence of disorder, the data in this inset are for the disorder-free structure. We have checked that including disorder does not change significantly the results when the tip center is taken as the reference point for the PLDOS. For both tip shapes, (7.1) and hard wall, and independently of where the PLDOS is taken, the cross-correlation decreases with increasing depletion diameter D.

If the PLDOS is taken at the classical turning point (triangles) instead of the tip center (squares), the SGM response becomes less correlated with the PLDOS. The classical argument of Ref. [38] that predicts that a large circular hard-wall tip does image the local properties of the unperturbed structures by reflecting back the classical trajectories that hit the tip with normal incidence does not appear as a limiting case of our results. One reason could be that our numerics did not reach sufficiently large depletion disks with $D \gg \lambda_{\mathrm{F}}$ to observe such a behavior [72]. However, since our analytics do not predict any simple relationship between the SGM and the PLDOS at the classical turning point, another mathematical relation between the two quantities cannot be excluded from our study.

Chapter 8

Link between SGM response and the Hilbert transform of the LDOS in 1D and 2D

In the introduction we have mentioned the theoretical work [48] stating that the linear term of the SGM response in the perturbative regime and the LDOS are related by a Kronig-Kramers relationship. Here we discuss in more detail this correspondence and show that it is only valid for one-dimensional scatterers. A numerical check that illustrates the breakdown of such a relation in 2D is provided.

8.1 Derivation of the SGM response for a 1D scattering problem

In Ref. [48] Pala and coworkers found that the first order perturbation theory of the SGM response is proportional to the real part of the diagonal Green function, which is simply the Hilbert transform of the LDOS. But their derivation was based on a one dimensional setup. Our purpose in this chapter is to test the validity of such a correspondence in two dimensions.

We will first derive the underlying correspondence relationship using a procedure presented by Gasparian, Christen and Büttiker in 1996 [56], before the development of the SGM technique.

Let us consider a one-dimensional scattering potential located in the region $x_1 < x < x_2$ and ideal 1D leads attached at positions x_1 and x_2 . The scattering properties are described by the 2×2 scattering matrix S, whose matrix elements can be given in terms of the Green function using the

Fisher-Lee equation [18] :

$$S_{ll'} = -\delta_{ll'} + i\hbar\sqrt{v_l v_{l'}}\mathcal{G}^{(0)}(x_l, x_{l'}), \tag{8.1}$$

where v_l is the speed of the carriers coming from the one dimensional lead l and $\mathcal{G}^{(0)}(x_l, x_{l'})$ is the unperturbed Green function between positions x_l and $x_{l'}$ at the boundaries of the system.

The transmission across the potential barrier in the absence of any perturbation is simply

$$T^{(0)} = |S_{12}|^2. \tag{8.2}$$

Now we would like to calculate the correction to the transmission $T^{(0)}$ in first order in a perturbation $\delta u(x) = \delta u_0 \delta(x - x_0)$.

To do so we evaluate the functional derivative of the transmission T with respect to the perturbation potential δu

$$\frac{\delta T}{\delta u_0} = S_{12}^* \frac{\delta S_{12}}{\delta u_0} + S_{12} \frac{\delta S_{12}^*}{\delta u_0}. \tag{8.3}$$

According to (8.1) we have

$$\frac{\delta S_{12}}{\delta u_0} = i\hbar\sqrt{v_1 v_2} \frac{\delta \mathcal{G}(x_1, x_2)}{\delta u_0}. \tag{8.4}$$

Writing down the Dyson equation up to the first order in $\delta u(x) = \delta u_0 \delta(x - x_0)$

$$\mathcal{G}(x_1, x_2) = \mathcal{G}^{(0)}(x_1, x_2) + \int \mathcal{G}^{(0)}(x_1, x'')\delta u(x'')\mathcal{G}^{(0)}(x'', x_2)\mathrm{d}x'', \tag{8.5}$$

we find

$$\frac{\delta \mathcal{G}(x_1, x_2)}{\delta u_0} = \mathcal{G}^{(0)}(x_1, x_0)\mathcal{G}^{(0)}(x_0, x_2), \tag{8.6}$$

therefore

$$\frac{\delta S_{12}}{\delta u_0} = i\hbar\sqrt{v_1 v_2}\mathcal{G}^{(0)}(x_1, x_0)\mathcal{G}^{(0)}(x_0, x_2). \tag{8.7}$$

Plugging (8.7) in (8.3) one finds

$$\frac{\delta T}{\delta u_0} = \hbar^2 v_1 v_2 \mathcal{G}^{(0)*}(x_1, x_2)\mathcal{G}^{(0)}(x_1, x_0)\mathcal{G}^{(0)}(x_0, x_2) + h.c., \tag{8.8}$$

where h.c. extends for the hermitian conjugate operation.

According to Aronov's formula [73]

$$\mathcal{G}^{(0)}(x_1, x)\mathcal{G}^{(0)}(x, x_2) = \mathcal{G}^{(0)}(x_1, x_2)\mathcal{G}^{(0)}(x, x). \tag{8.9}$$

Thus the variation of the transmission T is

$$\frac{\delta T}{\delta u_0} = \hbar^2 v_1 v_2 |\mathcal{G}^{(0)}(x_1, x_2)|^2 (\mathcal{G}^{(0)}(x_0, x_0) + \mathcal{G}^{(0)*}(x_0, x_0)), \tag{8.10}$$

and finally the first order correction due to the potential $\delta u(x)$ is

$$\boxed{\frac{\delta T}{\delta u_0} = 2T^{(0)} \mathrm{Re}(\mathcal{G}^{(0)}(x_0, x_0))} \tag{8.11}$$

with $T^{(0)}$ the transmission amplitude in the absence of the perturbation $\delta u(x)$. This is the formula also obtained by Pala and coworkers in [48], but their extension of such a correspondence relation into higher dimensions was not justified. We now try to understand the difference between the one and two-dimensional cases in view of the previous result as well as the one obtained in Ref. [11], which have been presented in Chapter 3.

The first order perturbation theory [11] has been recalled in the equation (11.9) in Chapter 3. So it does not seem to be related to the Hilbert transform of LDOS in contrast to the one dimensional first order perturbation theory (8.11). The reason for that is simple. Let us start from the Lipmann-Schwinger equation (4.3) of the Chapter 3 that we write here up to the first order in the tip strength as

$$\psi_{l\varepsilon a}(\mathbf{r}_\mathrm{T}) = \psi^{(0)}_{l\varepsilon a}(\mathbf{r}_\mathrm{T}) + v_\mathrm{T} \mathcal{G}^{(0)}(\mathbf{r}_\mathrm{T}, \mathbf{r}_\mathrm{T}, \varepsilon) \psi^{(0)}_{l\varepsilon a}(\mathbf{r}_\mathrm{T}). \tag{8.12}$$

We now take the absolute square of both sides of (8.12) and omit the terms in v_T^2, leading to

$$|\psi_{l\varepsilon a}(\mathbf{r}_\mathrm{T})|^2 = |\psi^{(0)}_{l\varepsilon a}(\mathbf{r}_\mathrm{T})|^2 + 2v_\mathrm{T} \mathrm{Re}(\mathcal{G}^{(0)}(\mathbf{r}_\mathrm{T}, \mathbf{r}_\mathrm{T}, \varepsilon)) |\psi^{(0)}_{l\varepsilon a}(\mathbf{r}_\mathrm{T})|^2. \tag{8.13}$$

Summing over a leads to the relation

$$\boxed{\rho_{l\varepsilon}(\mathbf{r}_\mathrm{T}) - \rho^{(0)}_{l\varepsilon}(\mathbf{r}_\mathrm{T}) = 2v_\mathrm{T} \rho^{(0)}_{l\varepsilon}(\mathbf{r}_\mathrm{T}) \mathrm{Re}(\mathcal{G}^{(0)}(\mathbf{r}_\mathrm{T}, \mathbf{r}_\mathrm{T}, \varepsilon))} \tag{8.14}$$

with $\rho_{l\varepsilon}$ the PLDOS coming from lead l in the presence of the tip and $\rho^{(0)}_{l\varepsilon}$ the unperturbed PLDOS injected from the lead l. Notice that the same relation holds for the full LDOS. This relation is correct for any dimension. Now for a one dimensional scattering problem the ρ_l's are directly related to the transmission amplitudes, therefore the first order conductance correction obeys the same relation and reads

$$\boxed{\delta g = 2v_\mathrm{T} g^{(0)} \mathrm{Re}(\mathcal{G}^{(0)}(\mathbf{r}_\mathrm{T}, \mathbf{r}_\mathrm{T}, \varepsilon))} \tag{8.15}$$

This is the reason why in 1D the Hilbert transform appears in first order perturbation theory while it is absent in the two dimensional case. However the second term of the perturbation theory [11] contains a term which is proportional to the Hilbert transform of the LDOS (which is equal to the real part of the diagonal Green function) as mentioned in Sec. 6.3 of Chapter 6.

8.2 Numerical test

To illustrate the non correspondence between the SGM response and the Hilbert transform of the LDOS in 2D we have considered the ring geometry (see Fig. 4.1) used in chapter 6. We adopt here the same parameters.

The aim is to numerically calculate the SGM response and compare it with the Hilbert transform of the LDOS (11.17) as well as the first order perturbation theory of [11].

As illustrated in panel (a) of Fig. 8.1, the full SGM response to a delta tip, the unperturbed Green function and scattering wave-functions are numerically calculated using Kwant. Since we are interested in the linear term of the conductance corrections we have chosen a very weak tip strength $v_{\mathrm{T}} = \varepsilon_{\mathrm{F}} a^2/30$ where ε_{F} is the Fermi energy of the electrons, chosen here to be equal to 50 meV and a the grid spacing of the tight-binding network.

We observe that the analytical formula (11.9) of the first order perturbation theory provided by [11] and plotted in the panel (c) of Fig. 8.1 does reproduce quite well the fully numerically calculated SGM response in panel (a) of the same figure. However the formula (11.17) provided by [48], and plotted in panel (b) does not. It is important to mention here that the analytical formula of the first order perturbation theory (11.9) is evaluated by using the scattering matrix and the wave functions of the system provided by Kwant.

Although some of the structures seen in the LDOS plotted in panel (d) seem to be present in all the other maps, only the first order perturbation theory result [11] plotted in (c) provides a good agreement with the numerically calculated SGM response.

Furthermore, Pala and coworkers have presented numerical simulations [48] showing that in cases where the wave functions present a scarring behavior along periodic orbits [74], the SGM is well correlated with the LDOS.

From the numerical results presented in Fig. 8.1 we can conclude that the SGM response in 2D has no evident relationship with the Hilbert transform of the LDOS. Although a qualitative similarity with conductance measurements is widely reported in the literature [6, 7, 47, 48] the quantitative analysis of the presumed link between the two quantities is still missing in case of systems out of the quantization regime. Thus, more theoretical efforts are needed to understand the underlying correspondence if there is any.

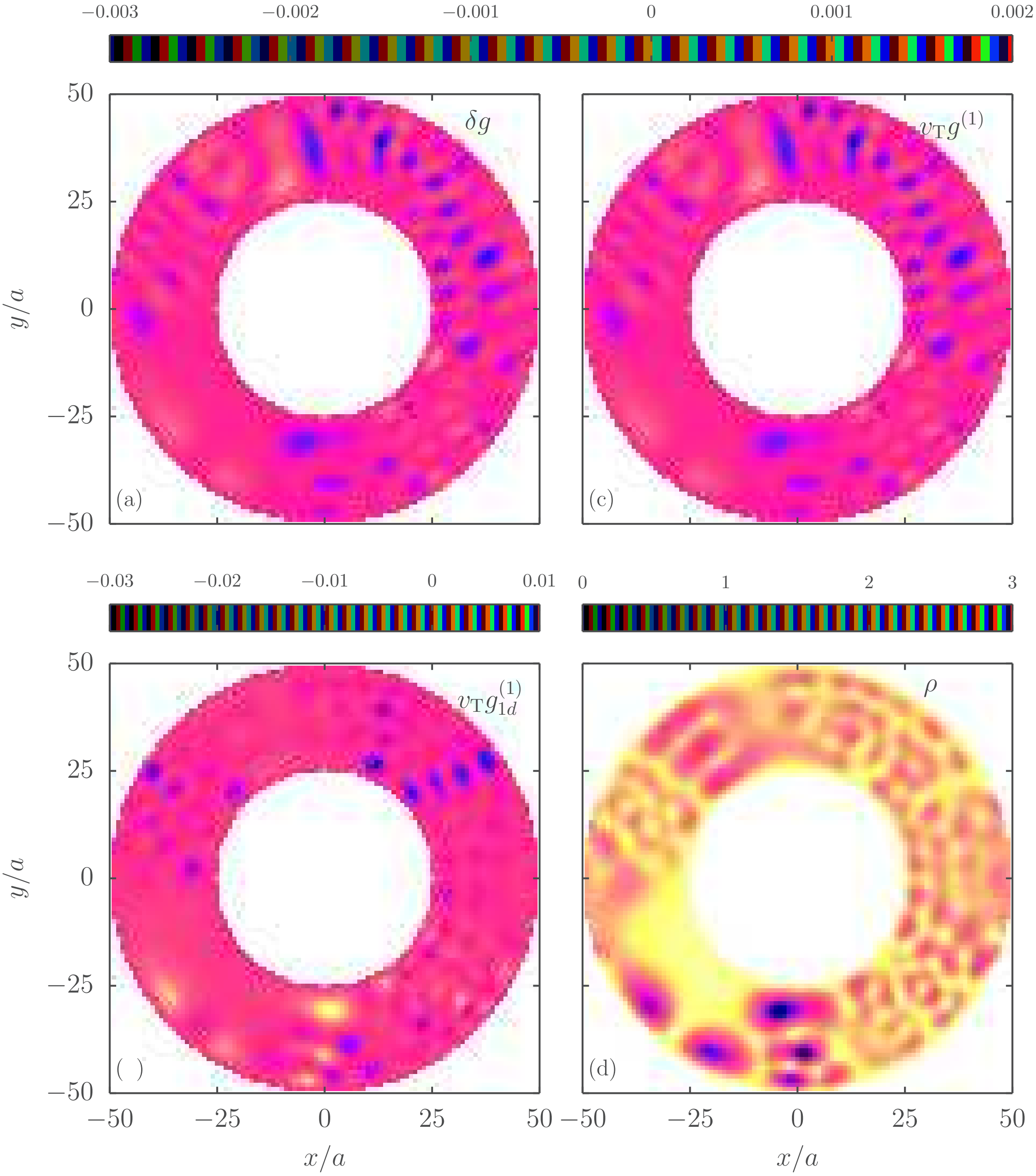

Figure 8.1: (a) The SGM response in the presence of a delta tip with strength $v_{\mathrm{T}} = \varepsilon_{\mathrm{F}}/30$ where $\varepsilon_{\mathrm{F}} = 50meV$. (b) The result of 11.17 which is proportional to the Hilbert transform of the LDOS is shown. In (c) The linear term of the SGM response calculated from the scattering wave-functions [11] is plotted. (d) The total LDOS. Al the data are calculated at the same Fermi energy.

Chapter 9

Energy dependent branches and interference phase shifts

In this chapter we present numerical simulations in the attempt to model physical effects recently observed in the experiment of our ETH colleagues. First, we discuss the branching behavior depending on the Fermi energy. Second, we analyze the temperature dependent phase shifts of the SGM signal. By considering a realistic QPC in the presence of smooth disorder, we are able to reproduce the experimentally observed effects. We provide in this chapter a mechanism that may be at the origin of this behavior, and we present in Appendix D complementary information about the energy dependent SGM branches.

9.1 Energy dependent branches

The aim of this section is to present numerical simulations of electron branches in a disordered 2DEG, and see how their location is affected by changing the Fermi energy of the electrons.

This study has been motivated by recent experimental work performed at ETH Zürich [Beat Braem et *al*, private communication, 2017]. In this experiment a back gate has been used to modify the carrier density in the 2DEG, allowing for the change of the Fermi energy of the electrons. The stability of the electron branches against the change of Fermi energy has been observed.

In order to understand the origin of the observed behaviour we performed numerical simulations considering the QPC model described below.

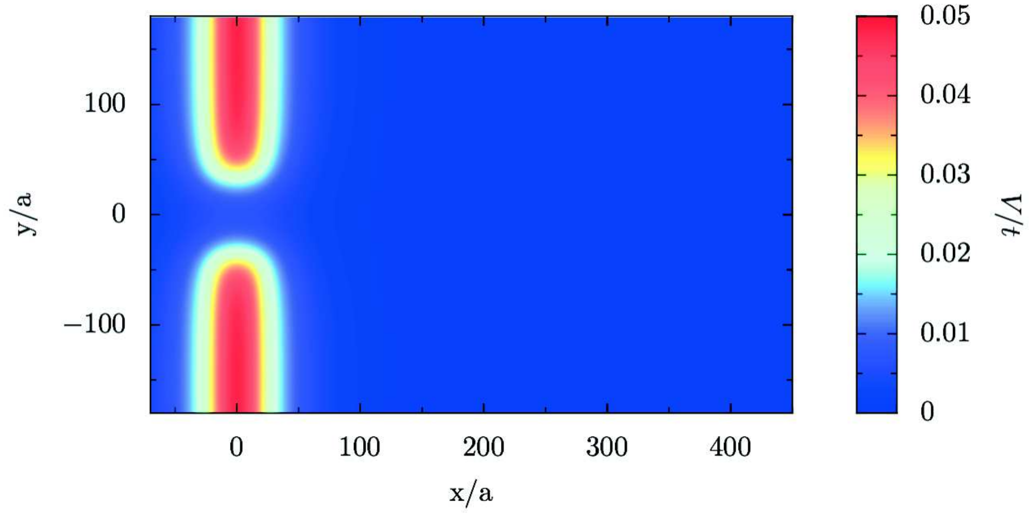

Figure 9.1: The potential generated by the model 9.1 with $V_g = 0.1t$.

9.2 Model for a smooth QPC

The confining potential of the QPC is obtained [75] from the analytical expression of the electrostatic potential created by a metallic plate situated at given distance d from the 2DEG. For a metallic gate horizontally situated between L(left) and R(right) and vertically disposed between B(bottom) and T(top) and situated at a given distance d from the 2DEG, the potential reads [75]

$$V(x,y) = V_g(P(x-L,y-B)+P(x-L,T-y)+P(R-x,y-B)+P(R-x,T-y)) \tag{9.1}$$

where V_g is the potential at which the gate is held and

$$P(u,v) = \frac{1}{2\pi}\arctan\left(\frac{uv}{d\sqrt{u^2+v^2+d^2}}\right). \tag{9.2}$$

Taking $d = 20a$, the potential resulting from two rectangular gates of width $|R-L| = 29a$, and separated by the distance $W = 66a$ is presented in Fig. 9.1.

In the left panel of Fig. 9.2 the SGM response is calculated at different energies for the disorder configuration (1) (see Appendix D). At each Fermi energy, the QPC is tuned to the third plateau of conductance ($g^{(0)} \approx 3$). The tip profile (7.1) has been used. The strength of the tip is varied with the Fermi energy in order to have the same depletion disc diameter. We take $v_{\mathrm{T}} = 10ta^2$ and fix the distance parameter d at $d = 10a$. We observe that the branches barely move when the Fermi energy is changed from $0.4t$ to $0.2t$ while they change drastically between $E_F = 0.2t$ and $E_F = 0.1t$. The same behavior is observed in the PLDOS (right panel of Fig. 9.2).

In Fig. 9.3 the same data as in Fig. 9.2 are presented for the disorder configuration (2) (see Appendix D). In these data the tip parameters are fixed at $v_{\mathrm{T}} = 10ta^2$ and $d = 10a$. We observe the same effect as in Fig. 9.2.

Since the same behavior is present in the unperturbed PLDOS, we think that this effect can be reproduced without calculating the SGM response which is numerically demanding. However, the PLDOS can be easily calculated for more energies to investigate in detail the energy dependence of the branch locations.

In Fig. 9.4 and Fig. 9.5 the PLDOS is calculated for intermediate energies not presented in Fig. 9.2 and Fig. 9.3. We observe that for energies varying from $\varepsilon_{\mathrm{F}} = 0.2t$ to $\varepsilon_{\mathrm{F}} = 0.35t$ the branches are very similar. However, they start to slightly change below $\varepsilon_{\mathrm{F}} = 0.15t$ for both of the two disorder configurations. Other disorder realizations are also investigated. The corresponding data are shown in Fig.D.2 and Fig.D.3 of Appendix D. Further data illustrating such an effect when the Fermi energy is fixed at $\varepsilon_{\mathrm{F}} = 0.2t$ and the strength of the disorder is varied, are shown in Fig.D.4, Fig.D.5 and Fig.D.6 of Appendix (D). We think that the branches should be stable as long as ε_{F} is larger than a critical potential defined by the disorder level, but a quantitative study is needed to rigorously clarify on the above observations.

9.2.1 Interference phase shifts at high temperature

The search for new coherent effects possible to be imaged by the SGM tip is always active in both the experimental and theoretical sides. In a very recent experiment (not published yet), the team of ETH Zürich [Beat. Braem et *al*, private communication (2017)] has observed some interference features that have not been previously revealed in any other SGM experiment. In this experiment interference phase shifts persist at high temperatures.

With the aim of understanding this experimental finding we further performed numerical simulations. We considered the QPC model presented in Sec. 9.2. The QPC is tuned to the third plateau of conductance ($g^{(0)} \approx 3$). The used tip potential is of the form (7.1) with $v_{\mathrm{T}} = 10ta^2$ and $d = 10a$.

Assuming that the observed phase shifts are due to some hard impurities distributed in the neighborhood of the QPC, we intentionally placed two hard impurities in the direction of flow. In the left panel of Fig. 9.6 the SGM conductance is numerically calculated. The narrow branches that are clearly seen in the PLDOS shown in the right panel, are due to the hard impurities. These narrow branches are not present if no hard scatterers are

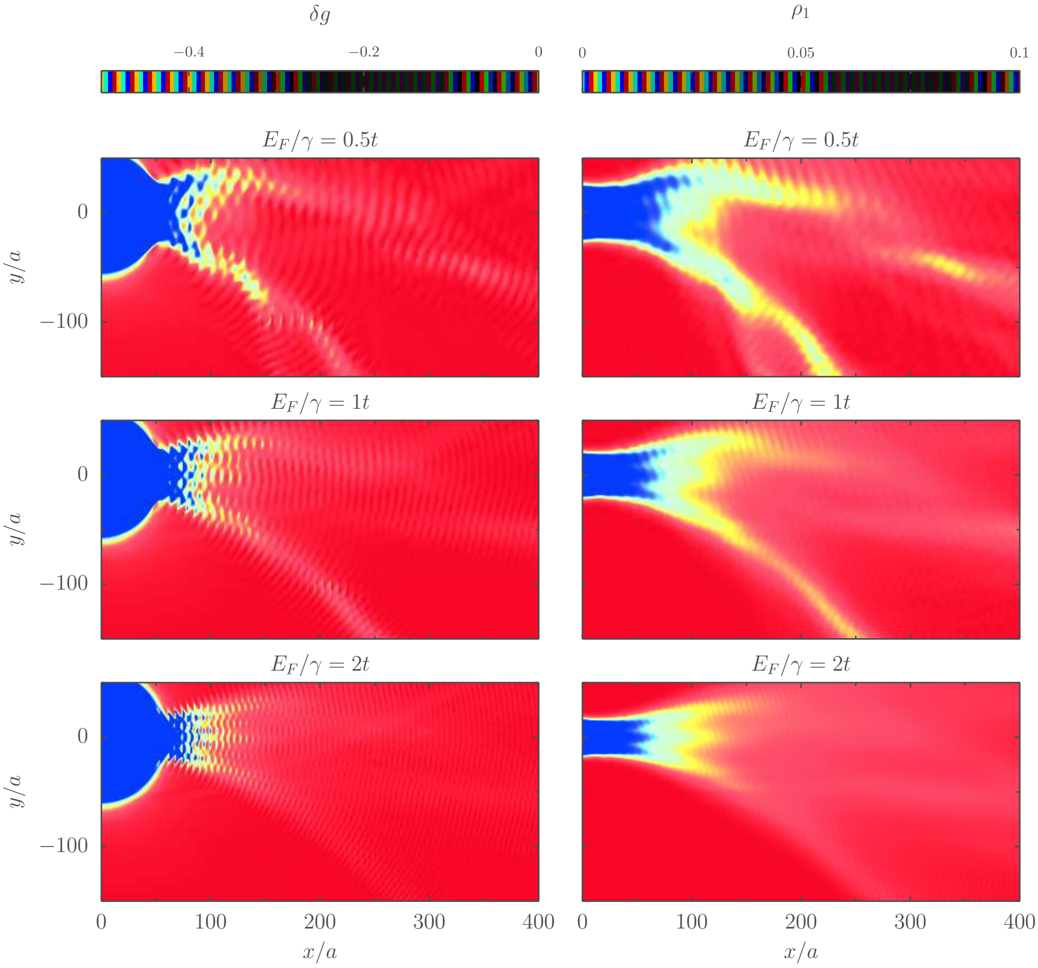

Figure 9.2: In the left column the SGM response is shown at different Fermi energies for disorder configuration (1) (see appendix D). The tip potential is adjusted with the Fermi energy such that the depletion disc is the same in all the maps, we have taken $v_{\mathrm{T}} = 10ta^2$ and $d = 10a$. In the right column the PLDOS is shown for the same disorder configuration. The disorder strength γ is fixed at $\gamma = 0.2$.

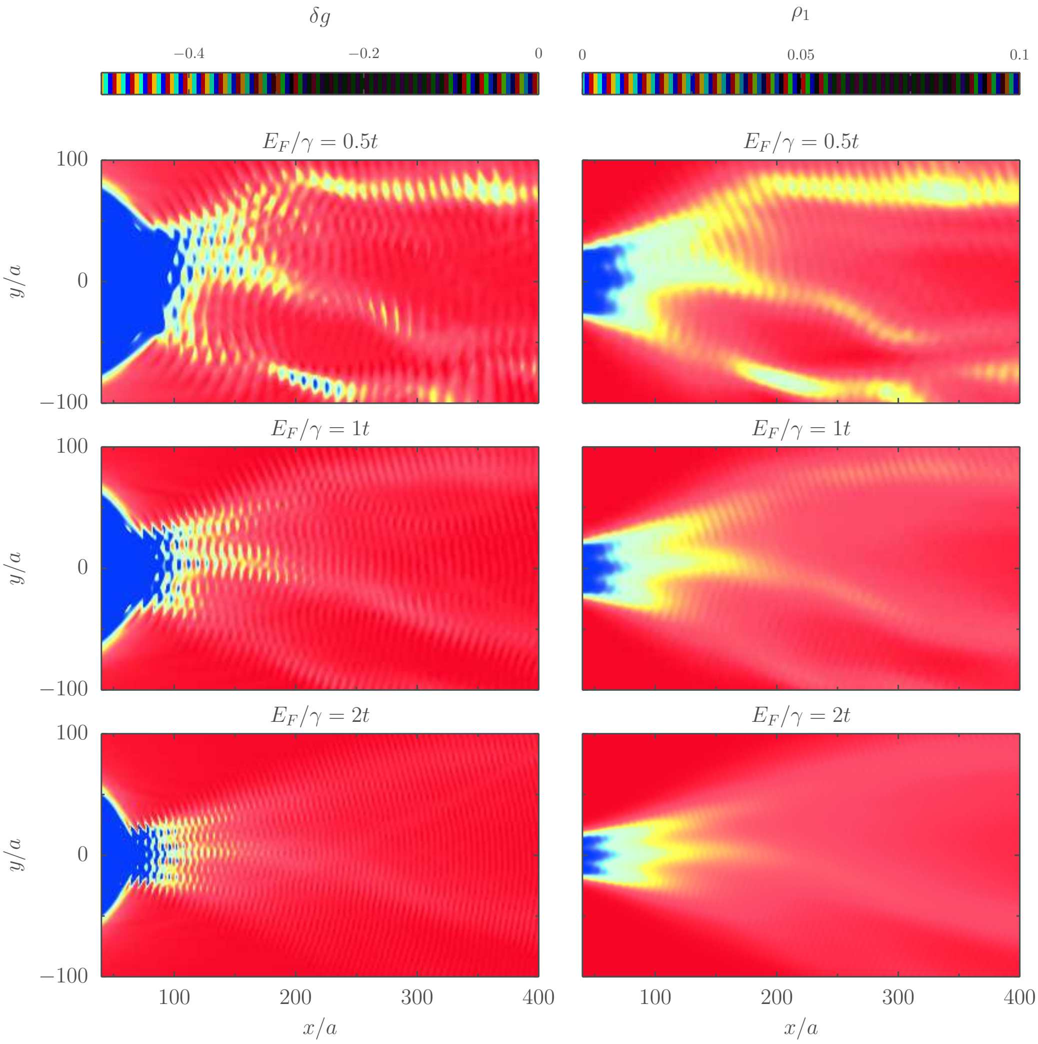

Figure 9.3: The same data as in Fig. 9.2 but for the disorder configuration (2) (see appendix D). The disorder strength γ is fixed at $\gamma = 0.2$ and the tip parameters are not adjusted but fixed at $v_{\mathrm{T}} = 10ta^2$ and $d = 10a$.

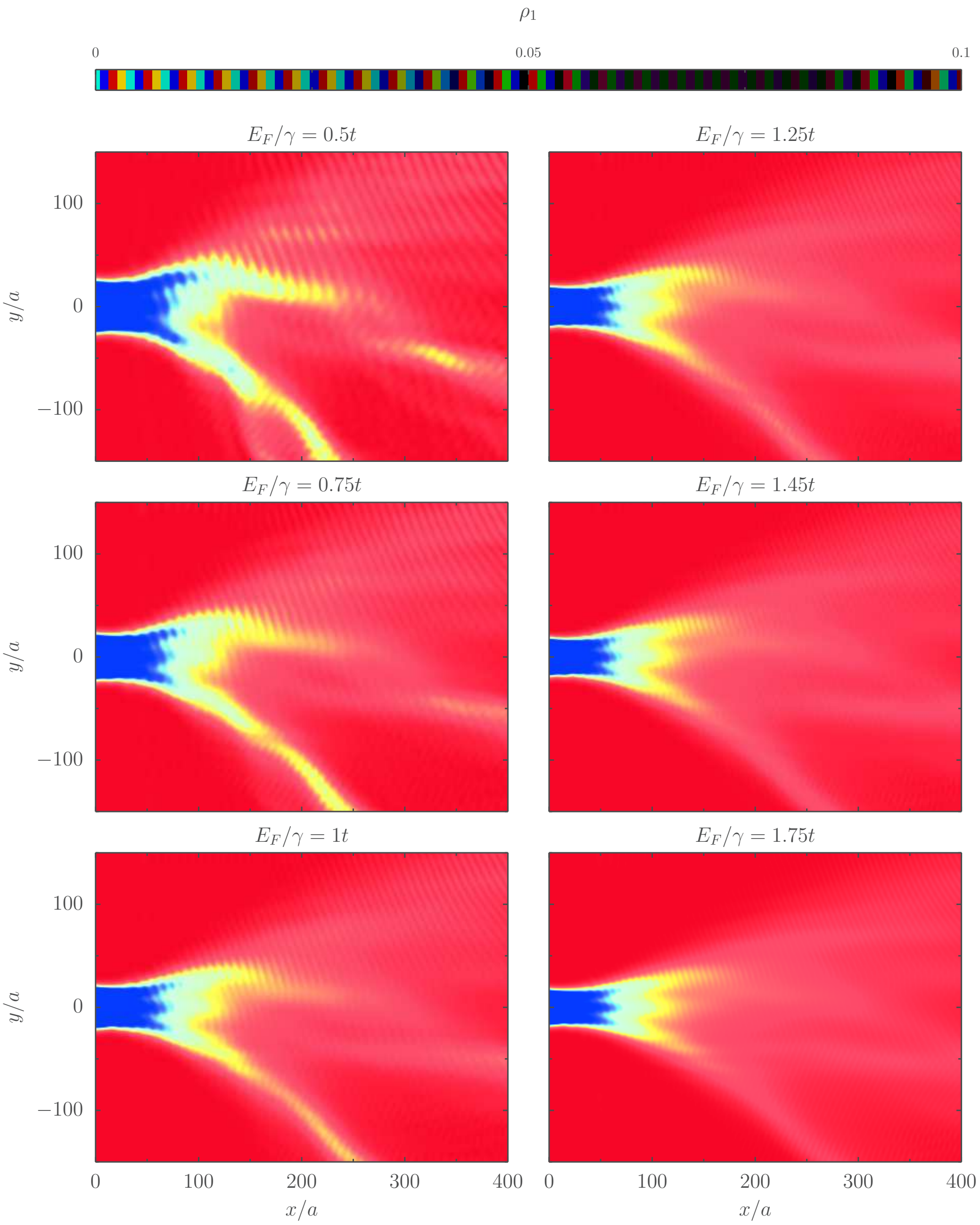

Figure 9.4: PLDOS at different energies for configuration 1. The disorder strength γ is fixed at $\gamma = 0.2$.

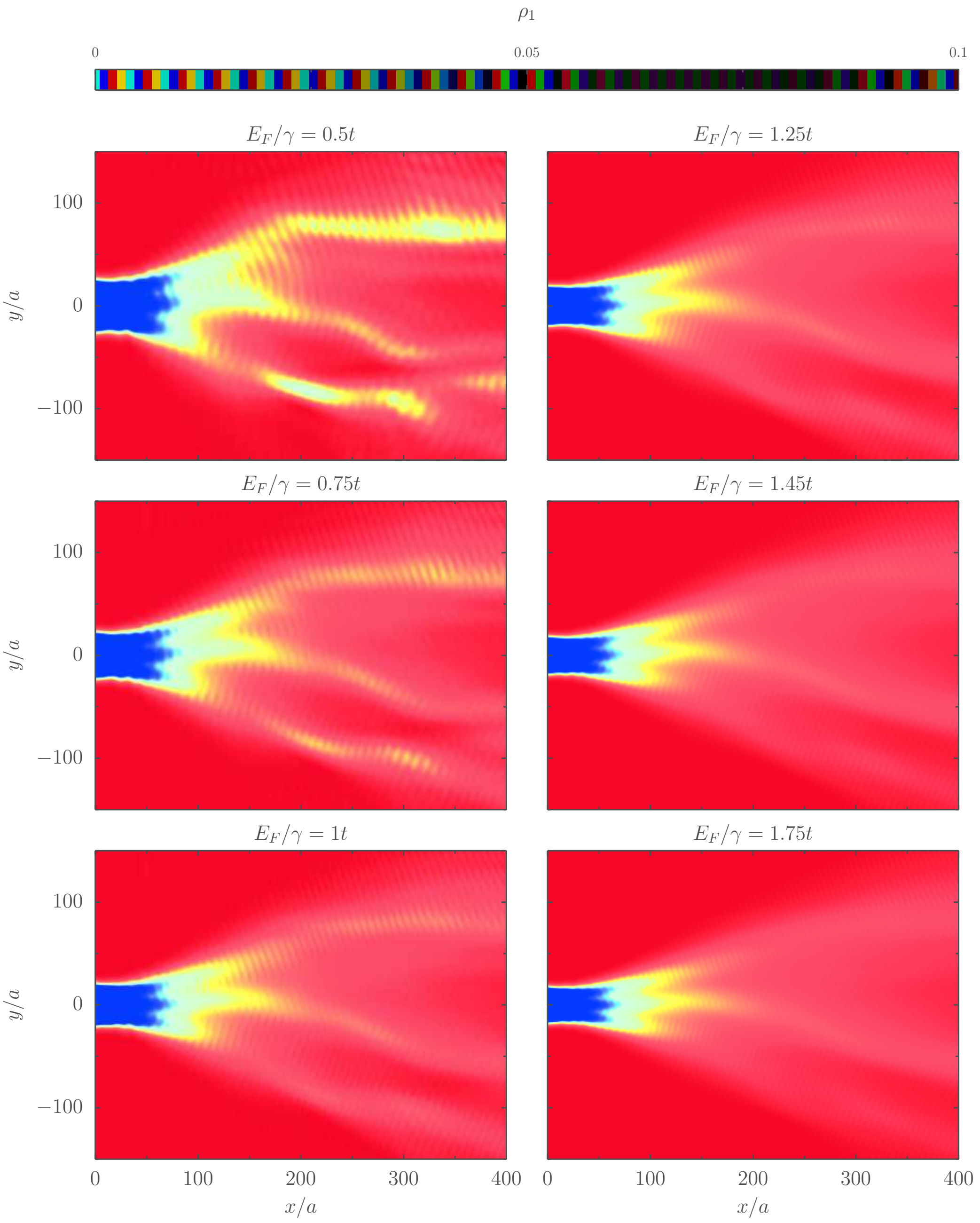

Figure 9.5: PLDOS at different energies for configuration (2). The disorder strength γ is fixed at $\gamma = 0.2$.

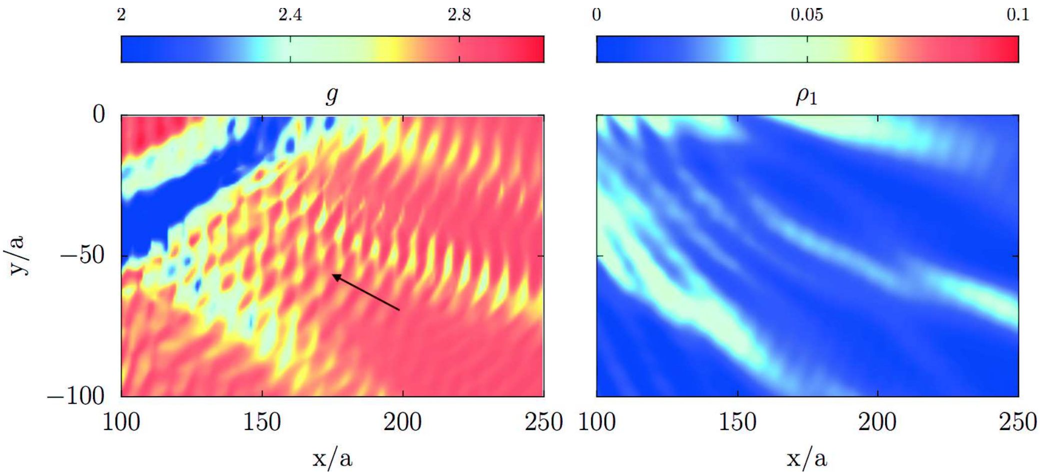

Figure 9.6: In the left panel the SGM response in the presence of hard impurities is shown. The QPC situated at $(x = 0, y = 0)$ is tuned to the third conductance plateau. In the right panel the corresponding PLDOS is presented.

considered.

To investigate the persistence of the phase shifts (see the black arrow in Fig. 9.6) at high temperature we calculated the SGM response at different temperatures. To include temperature, we used the finite temperature Landauer formula (1.41). We calculated the transmission at different energies, and took the average with weights defined by the Fermi-Dirac distributions. The results are shown in Fig. 9.7.

The mechanism we propose to explain this observation is as follows. In the presence of hard impurities the unperturbed branching pattern can be strongly modified and narrow branches can develop (see the PLDOS in the right panel of Fig. 9.6). In this situation two trajectories originating from two adjacent branches can interfere giving rise to the observed phase shifts. Since these interferences are yielded by such trajectories they can persist at higher temperatures as long as the thermal length is bigger than the length difference between the involved trajectories.

In conclusion, our numerical simulations of the SGM and the PLDOS in a realistic QPC, show that the electron branches due to the surrounding disorder are very robust against the change of Fermi energy as long as the ratio between the latter and the disorder strength is bigger than a critical value but a quantitative argument is missing. The phase-shifts observed in the experimental data of our colleagues from ETH Zürich have been successfully reproduced by incorporating hard impurities in our numerical simulations.

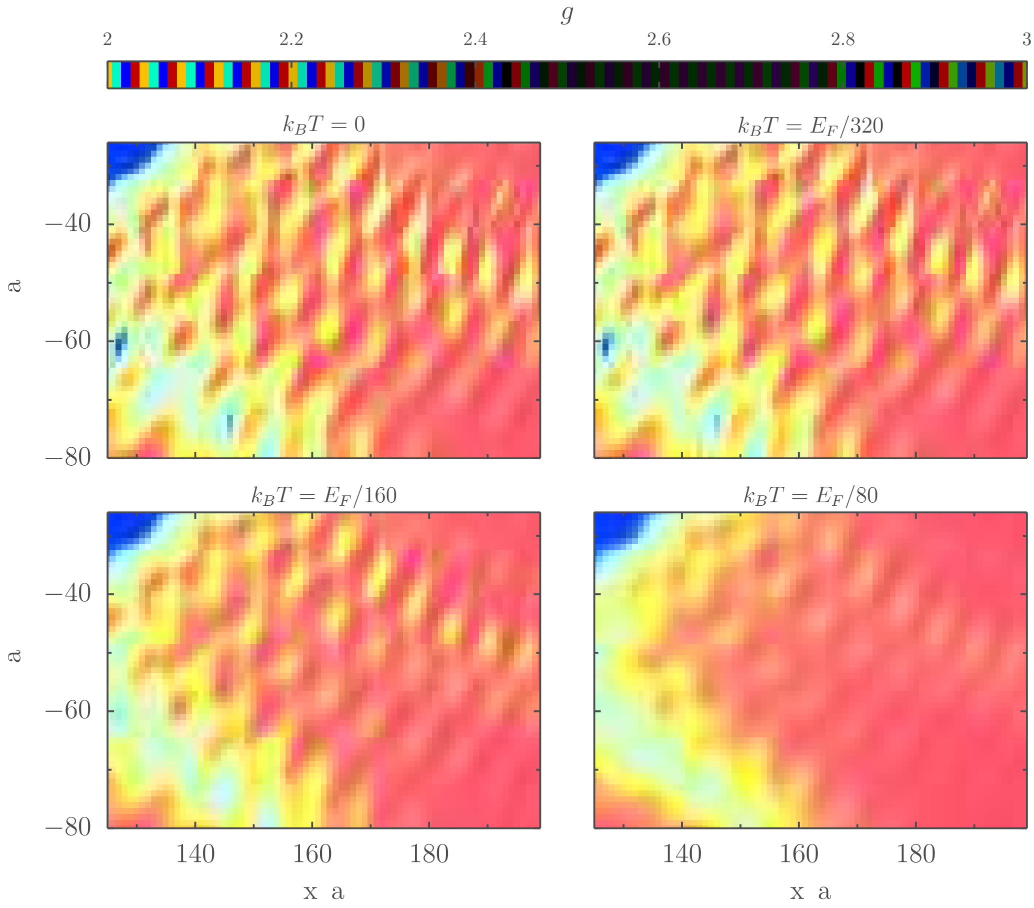

Figure 9.7: The SGM response in the presence of hard impurities at different temperatures.

Chapter 10

Conclusions and perspectives

10.1 Extraction of PLDOS from SGM

With the aim of extracting information about local electronic properties in phase-coherent devices from SGM measurements, we have investigated the correspondence between the SGM response in the vicinity of a QPC and the unperturbed PLDOS.

Only on the first conductance step, the PLDOS could be shown to provide an upper bound for the magnitude of the first-order SGM correction. We have shown analytically that the unperturbed PLDOS squared is unambiguously related to the second-order conductance correction induced by a local tip, provided that the system is time-reversal symmetric and the QPC is tuned to perfect transmission where the conductance is a multiple of $2e^2/h$. The second-order correction dominates the SGM response on a perfect conductance plateau if the tip strength is not too strong. If the QPC transmission is imperfect, the exact correspondence between the SGM and the PLDOS is broken, and the departures are quantified with a perturbative approach. It does not depend on fine details of the setup, but rather on the scale of the unperturbed conductance's deviation Δg from the perfectly quantized conductance. .

We have demonstrated that a correspondence between the locally averaged second-order SGM response and the PLDOS survives for imperfect transmission obtained when the highest propagating eigenchannel is not completely open. Numerical simulations within a recursive Green function approach have confirmed our analytical findings and shown that they also hold in the case of disordered systems. We think that a moderate temperature would play the same role as the local averaging and helps to reestablish the SGM-PLDOS correspondence even in the case of non perfect unit transmission. Moreover, we found that in the case of a local tip, and sufficiently small Δg, the full SGM response is related to the PLDOS once the tip is strong enough such that the second-order conductance correction dominates.

In the case of non-local tips, where the depletion disk created by the tip exceeds half the Fermi wavelength, the correspondence between the SGM response and the PLDOS established for weak local tips degrades with increasing depletion disk radius.

10.2 Saturation of the SGM response for strong delta tips

We have presented the analytical expression of the full SGM conductance beyond perturbation theory under the assumption of having a delta like tip. The simplification of the Lippmann-Schwinger and Dyson equations has allowed us to express the scattering wave-function in the presence of the $\delta-$tip in terms of the unperturbed scattering wave-function. Therefore, the energy integrals involved in the conductance calculations turned out to be tractable. The result shows that when the strength of the tip is much bigger than the Fermi energy the conductance saturates at values given by the unperturbed Green function. We have checked this behavior by means of numerical simulations.

If the tip is not in the form of a $\delta-$ function, we have shown in Chapter 5 that an iterative method can be used to obtain the SGM response in the presence of an arbitrary tip potential.

10.3 Hilbert transform of the LDOS and SGM in 2D

In addition to the perturbation theory [11, 15] presented in Chapter 3, a somewhat different perturbative approach [6] has related the the SGM response to the Hilbert transform of the LDOS. However, in Ref. [6] a one-dimensional chain has been assumed to obtain the involved correspondence relation between SGM and LDOS.

In order to understand the difference between the two results we investigated in Chapter 8 the circumstances under which the interpretation of the SGM signal as a Hilbert transform of the LDOS is possible. We have shown that this relationship is characteristic of 1D scattering problems. Since there is no analytical evidence of this interpretation in higher dimension we have performed numerical simulations to test whether it holds in 2D or not. Our numerical simulations show that while the analytical expression provided by Ref. [11, 15] reproduces the SGM signal, the expression of the conductance given by the Hilbert transform of the LDOS is different from the SGM response. Meaning that the interpretation provided by [6] does not hold for 2-dimensional scattering problems.

10.4 Perspectives

10.4.1 Numerical implementation of the Green function method for the conductance in the presence of a moving scatterer

In Chapter 5 we have presented a method allowing us to find the analytical expression for the conductance of a finite moving scatterer. The efficiency of such a method for short range potentials is obvious. However, if the potential is long-range, a comparison with the traditional way of computing the conductance by iterating over the positions of the scatterer has to be done.

10.4.2 Role of temperature in the SGM-PLDOS correspondence

In Chapter 6, we have highlighted that a small temperature could enhance the SGM-PLDOS correspondence in case of not unit transmissions, by averaging out the $\lambda_F/2$ oscillations of the SGM response, like the local averaging presented in Sub-section. 6.4.1. A quantitative study of the role of the temperature in the SGM-PLDOS correspondence has yet to be established.

10.4.3 Signatures of spin-orbit coupling in electron branching flow

In Chapter 2, we have mentioned the numerical simulations of Ref. [10] showing that in the presence of SOC interaction the SGM response of a QPC surrounded by a disorder-free 2DEG, is strongly modified due to the mode mixing induced by the $\sigma_y k_x$ term of the Rashba Hamiltonian (2.2). Additional features have been shown to appear as a signature of the SOC. In order to investigate whether this signature can be observed in real experiments or not, we performed KWANT simulations of the SGM response in the presence of disorder, with and without SOC. We adopted the same QPC model and the same physical parameters as in Ref. [10].

As shown in Fig. 10.1, our preliminary results do not show such strong features. A perspective line of work that we would like to undertake is the understanding of why the additional lobes observed in the disorder-free simulations do not appear here.

10.5 Final conclusions

In this thesis we have theoretically investigated the SGM technique in order to present a rigorous and quantitative analysis of the underlying data. A crucial ingredient that allows us to have link between the SGM and the unperturbed PLDOS, is the locality of the used tip. However, most SGM experiments are performed in high mobility 2DEGs in which the Fermi wavelength is smaller than the depletion disk under the scanning tip. In this case, the relationship between the SGM response and the PLDOS squared degrades and beyond a large enough radius, it cannot be directly used to unambiguously extract local electronic properties. For experiments in the weakly invasive regime, the resolution of the SGM response is also limited by the width of the tip potential [65]. One way to approach the regime where the direct link is valid would be to use systems with lower Fermi energy and thus larger Fermi wavelength.

In a very recent SGM experiment [76] performed using ultracold atom gases, a tightly focused laser beam played the role of the tip and could be scanned in the neighborhood of a QPC attached to two atom reservoirs. In this case a resolution better than 10nm with a tip size well below λ_{F} was obtained. In this regime, we expect that the relationship established between the SGM response and the PLDOS is applicable.

We think that the idea of using 2DEGs with lower Fermi energies is an important direction of research to be taken into account in the experimental side in order to achieve the suitable regime in which the local electronic properties are accessible by conductance measurements.

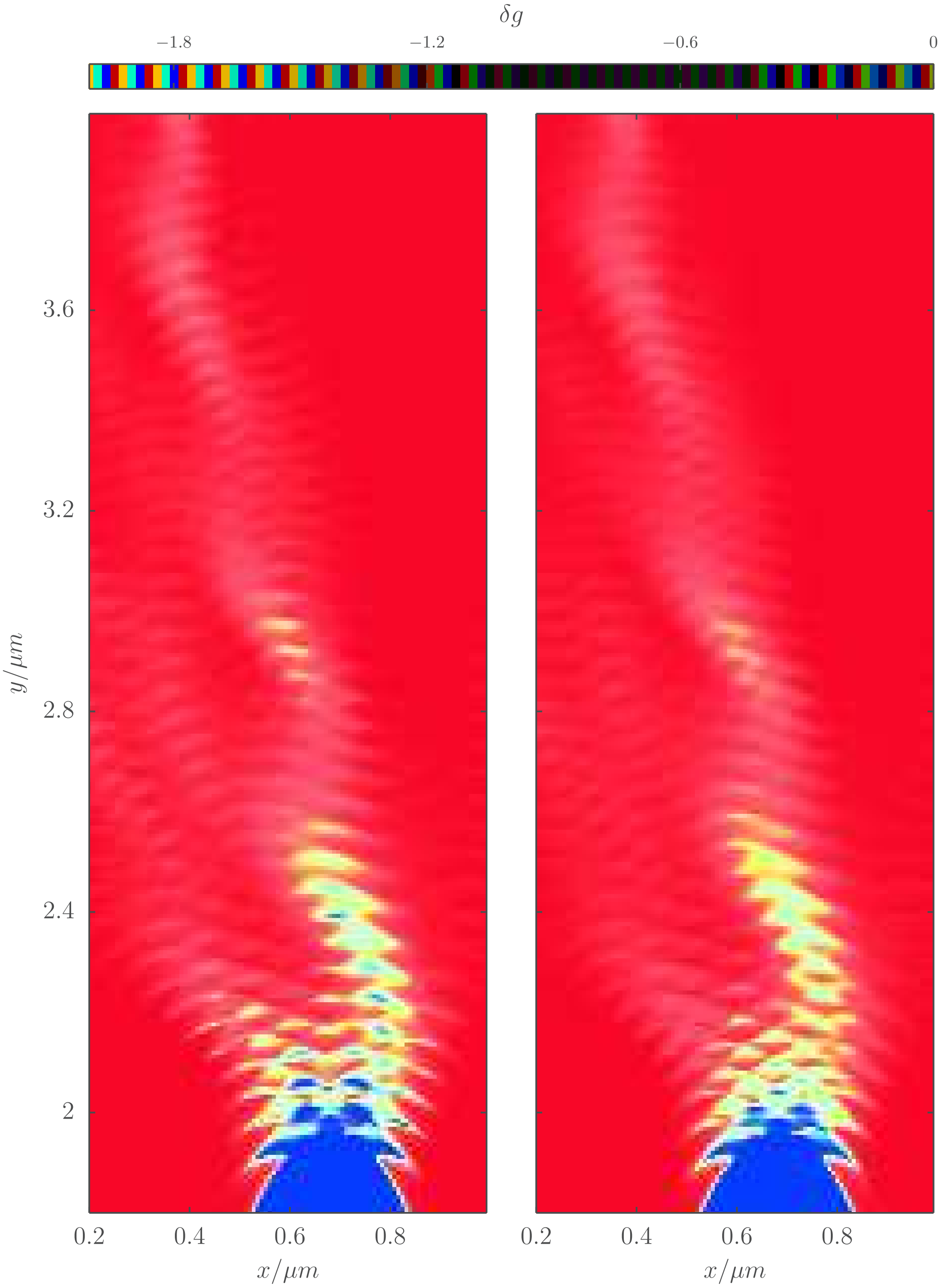

Figure 10.1: The SGM response is numerically calculated using KWANT, in the presence of smooth disorder. In the left panel the SOC is not included. In the right panel, SOC is considered. The QPC, located at the bottom of each plot is tuned to the second plateau $g^{(0)} \approx 2$.

Chapter 11

Résumé de la thèse

11.1 Introduction

Depuis son développement il y a deux décennies [34], la microscopie à grille locale (Scanning gate microscopy; SGM) a révélée des phénomènes fascinants de transport quantique [4, 5] et a été considérée comme une technique très prometteuse [77] pour sonder les propriétés locales des électrons dans une nanostructure donnée.

Dans cette technique la pointe d'un microscope à force atomique (atomic force microscope; AFM) est utilisée comme grille locale qui diffuse les électrons d'un gaz bi-dimensionnel créé dans une hétérostructure à base de semi-conducteurs et modifie ainsi la conductance que l'on mesure en fonction de la position de la pointe, ce qui rajoute une résolution spatiale à la mesure (voir FIG. 1).

La possibilité de travailler à très basse température ($T < 1°$K) et la précision subnanométrique du positionnement de la pointe permettent de travailler dans le régime de transport quantique où le caractère ondulatoire de la propagation électronique est sondé. La méthode SGM est donc un outil pour étudier les propriétés de transport quantique dans des gaz bi-dimensionnels nanostructurés.

La technique SGM a été utilisée pour étudier différents systèmes mésoscopiques, parmi lesquels des anneaux Aharanov - Bohm [46], les nanotubes de carbone [49] et d'autres systèmes fabriqués à base de graphène [50, 51]. Dans cette thèse une attention particulière est donnée au contact quantique (quantum point contact; QPC) qui est crée dans un gaz d'électrons bi-dimensionnel par deux grilles métalliques (voir FIG. 1). Le changement du potentiel appliqué sur ces grilles permet de contrôler le nombre de canaux ouverts dans le contact. Dû au fait que chaque canal ouvert conduit un quantum de conductance [2, 24], lorsqu'on varie la tension de grille, la conductance à travers l'échantillon présente des plateaux à valeurs quantifiées.

Les premières expériences SGM à proximité de QPC ont montré des franges d'interférences avec une période d'une demi longueur d'onde électronique. Cela a permis de conclure qu'il s'agissait d'une observation des propriétés dues au transport cohérent des électrons [4]. La présence de branches dans les images SGM a été interprétée comme étant reliée [5] à l'écoulement des électrons dans le paysage du potentiel désordonné créé par des dopants ionisés situés à une certaine distance du gaz d'électrons.

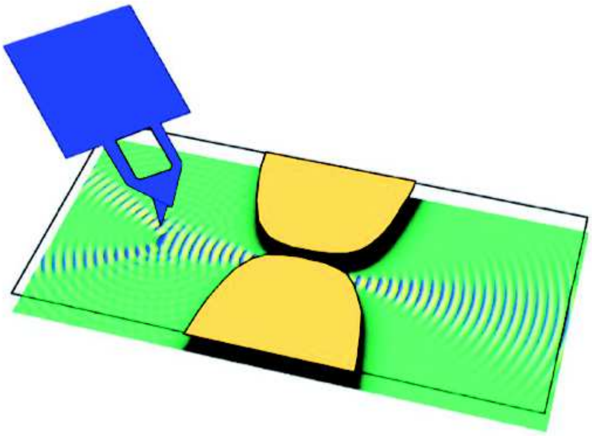

Figure 11.1: Présentation schématique de la microscopie à grille locale. Les ondes électroniques traversant une construction créée par deux grilles métalliques (en jaune) dans un gaz bi-dimensionnel (en vert) sont localement perturbées par la pointe AFM (en violet). L'image est prise de la référence [4].

La possibilité d'observer l'écoulement des électrons dans le régime de transport quantique, évoquée par les expérimentateurs [4, 5], serait une percée importante dans l'étude des phénomènes de transport quantique. Cependant, l'interprétation des données SGM est restée seulement qualitative. De plus, la relation d'incertitude de Heisenberg pose des limitations à la possibilité d'observer l'écoulement de particules quantiques.

Dans le but de comprendre ce qui est mesuré par les expériences SGM, une théorie analytique a été développée dans l'équipe mésoscopique de l'IPCMS, traitant la pointe SGM comme une perturbation du système [11, 15]. Les changements de la conductance dus à la pointe AFM ont été exprimés en fonction des matrices de transmission et de réflexion de la nanostructure non-perturbée ainsi que les éléments de matrices du potentiel créé par la pointe entre les états de diffusion incidents des électrodes opposées. En général, cette expression analytique de la conductance ne présente pas de relation simple avec les propriétés électroniques locales. C'est seulement dans la situation très particulière d'un QPC avec symétrie spatiale, en régime de conductance parfaitement quantifiée qu'il a été constaté que la réponse SGM pour une pointe locale et faiblement invasive était proportionnelle au carré de densité locale partielle (PLDOS [1]) [15], ce qui permet de remonter à cette quantité électronique (et dans certaines situations au courant local). Pourtant, une situation réaliste ne remplit pas les conditions pour lesquelles cette relation a été établie.

Les travaux de cette thèse établissent la théorie de la relation entre la réponse SGM et les propriétés électroniques locales pour des situations réalistes, expérimentalement envisageables. Un intérêt particulier est porté à la possibilité d'extraire des propriétés électroniques locales à partir d'une mesure SGM au-delà des limites du résultat rigoureux des travaux précédents. En plus, une partie de cette thèse est dédiée aux développements d'approches théoriques permettant de calculer la réponse SGM au delà de la théorie de perturbation. Pour optimiser le calcul numérique de la réponse SGM une méthode basée sur les fonctions de Green est proposée.

Finalement, dans un chapitre de cette thèse une clarification théorique est apportée vis-à-vis une interprétation alternative proposée par nos collègues dans Ref. [48]. En effet dans cette interprétation la réponse SGM a été liée à la transformation de Hilbert de la densité locale. Dans un tel chapitre nous avons montrés que cette dernière relation de correspondance n'est valide que pour des problèmes de diffusion unidirectionnels.

11.2 Théorie de perturbation

Dans le but de comprendre ce qui est mesuré lors d'une expérience SGM, l'obtention d'une formule analytique pour la conductance serait un avantage fabuleux. Néanmoins, la résolution de l'équation de Schrödinger en présence d'un potentiel d'une forme donnée n'est possible que dans des cas très limités.

Pour avoir une relation entre la réponse SGM et les propriétés locales, une théorie de perturbation à été élaborée [11, 15]. Le point de départ d'une telle théorie est l'équation de Lippmann-Schwinger qui relie la fonction de diffusion (la fonction d'onde en présence d'un potentiel diffuseur avec comme condition limite un flux incident) en présence de la pointe aux fonctions

---

[1] La PLDOS correspond à la densité locale d'états de diffusion incidents d'un seul réservoir.

de diffusion en son absence. Cette équation est l'analogue de l'équation de Dyson qui en son tour donne une relation entre les fonctions de Green en présence et en absence de la pointe.

L'équation de Lippmann-Schwinger en présence d'une pointe SGM de potentiel $V_{\mathrm{T}}(\mathbf{r})$ s'écrit en premier ordre de V_{T} comme suit

$$\Psi^{(1)}_{l,\varepsilon,a}(\mathbf{r}) = \int \mathrm{d}\bar{\mathbf{r}}\ \mathcal{G}^{(0)}(\mathbf{r},\bar{\mathbf{r}},\varepsilon) V_{\mathrm{T}}(\bar{\mathbf{r}}) \Psi^{(0)}_{l,\varepsilon,a}(\bar{\mathbf{r}})\ , \tag{11.1}$$

ou $\Psi^{(0)}_{l,\varepsilon,a}$ représente la fonction de diffusion en absence de la pointe associée au mode a et l'énergie ε pour une incidence d'un réservoir l, et $\mathcal{G}^{(0)}$ est la fonction de Green non-perturbée. La densité de courant associée à un tel état de diffusion est donnée par

$$\delta^{(1)} J_{l\varepsilon a} = \frac{e\hbar}{M_e} \mathrm{Im}(\Psi^{(0)*}_{l\varepsilon a}(\mathbf{r})\partial_x \Psi^{(1)}_{l\varepsilon a}(\mathbf{r}) - \Psi^{(1)}_{l\varepsilon a}(\mathbf{r})\partial_x \Psi^{(0)*}_{l\varepsilon a}(\mathbf{r})). \tag{11.2}$$

Le comportement asymptotique des fonctions de diffusion est crucial pour calculer la conductance, il est donné par

$$\Psi^{(0)}_{l,\varepsilon,a}(\mathbf{r}) = \begin{cases} \delta_{l,1}\varphi^{(-)}_{l,\varepsilon,a}(\mathbf{r}) + \sum_{b=1}^{N} (S^{1,l})_{ba}\, \varphi^{(+)}_{1,\varepsilon,b}(\mathbf{r}), & x \ll -L/2 \\ \delta_{l,2}\varphi^{(-)}_{l,\varepsilon,a}(\mathbf{r}) + \sum_{b=1}^{N} (S^{2,l})_{ba}\, \varphi^{(+)}_{2,\varepsilon,b}(\mathbf{r}), & x \gg L/2 \end{cases} \tag{11.3}$$

où $S^{l,l'}$ sont les sous-matrices de la matrice de diffusion S. Lorsque l est diffèrent de l', $S^{l,l'}$ est la matrice de transmission pour une incidence du réservoir l. Si $l = l'$, il s'agit alors d'une réflexion vers le réservoir d'incidence. Les fonctions d'onde $\varphi^{(\pm)}$ sont celles des réservoirs, elles sont données par

$$\varphi^{(\pm)}_{1\varepsilon a}(\mathbf{r}) = \frac{c}{\sqrt{k_a}} \phi_a(y) e^{\pm i k_a x}, \tag{11.4}$$

pour le réservoir de gauche (situé dans la zone $x < 0$) et

$$\varphi^{(\pm)}_{2\varepsilon a}(\mathbf{r}) = \frac{c}{\sqrt{k_a}} \phi_a(y) e^{\mp i k_a x}, \tag{11.5}$$

pour le réservoir de droite (situé dans la zone $x > 0$). Le nombre k_a est le module du vecteur d'onde longitudinal du mode a et $\phi_a(y)$ est la fonction d'onde dans la direction transversale. La constante $c = \sqrt{\frac{M_e}{2\pi\hbar^2}}$ avec M_e la masse effective de l'électron dans le gaz considéré est choisi de sorte à ce que chaque mode transversal conduit une densité de courant valant $s\frac{e}{h}$, avec $s = +$ pour les modes se propageant vers la droite et $s = -$ pour ceux qui se propagent vers la gauche. En supposant que l'incidence est du réservoir de gauche $l = 1$, la densité de courant mène à la forme suivante du changement du courant total à l'énergie ε par l'effet de la pointe

$$I^{(1)}_{1,\varepsilon} = \frac{e}{\hbar}\,\mathrm{Im}(\mathrm{Tr}\left\{t^{\dagger}t\ \mathcal{V}^{11} + t^{\dagger}r'\ \mathcal{V}^{21}\right\}), \tag{11.6}$$

avec

$$\mathcal{V}^{\bar{l},l}_{\bar{a}a} = \int \Psi^{(0)*}_{\bar{l},\varepsilon,\bar{a}}(\bar{\mathbf{r}}) V_{\mathrm{T}}(\bar{\mathbf{r}}) \Psi^{(0)}_{l,\varepsilon,a}(\bar{\mathbf{r}}) \mathrm{d}\bar{\mathbf{r}}, \tag{11.7}$$

l'élément de matrice du potentiel de la pointe entre deux états de diffusion. La trace dans (11.6) est a prendre sur les modes propageant.

Dans le régime de la réponse linéaire à température nulle, la conductance est obtenue en différenciant le courant total par rapport au voltage appliqué, ce qui donne

$$G^{(1)} = 2eI^{(1)}_{1,\varepsilon_{\mathrm{F}}}, \tag{11.8}$$

avec $\Delta\mu$ la différence de potentiel chimique entre les deux réservoirs. A température nulle le courant total se résume en sa valeur à l'énergie de Fermi ε_{F}. Cela mène à la correction de conductance adimensionnée (i.e en unités de $\frac{2e^2}{h}$), en premier ordre au potentiel de la pointe [11, 15]

$$g^{(1)} = 4\pi \mathrm{Im}\left\{\mathrm{Tr}\left[t^{\dagger}r'\ \mathcal{V}^{21}\right]\right\}. \tag{11.9}$$

La formule (11.9) fournit une expression analytique de la correction au premier ordre de la théorie de perturbation. Néanmoins, cette conductance est nulle pour un système dont les canaux sont soit complètement ouverts, soit totalement fermés ce qui est le cas pour un plateau d'un QPC. Dans ce cas le calcul de la correction dominante doit être fait pour le second ordre de la théorie de perturbation. Pour cela nous devons écrire l'équation de Lippmann-Schwinger au second ordre au potentiel de la pointe. Ce qui revient à écrire

$$\Psi^{(2)}_{l,\varepsilon,a}(\mathbf{r}) = \int \mathrm{d}\bar{\mathbf{r}}\ \mathcal{G}^{(0)}(\mathbf{r},\bar{\mathbf{r}},\varepsilon) V_{\mathrm{T}}(\bar{\mathbf{r}}) \Psi^{(1)}_{l,\varepsilon,a}(\bar{\mathbf{r}}), \tag{11.10}$$

où $\Psi^{(1)}_{l,\varepsilon,a}(\bar{\mathbf{r}})$ est donnée par (11.10). En passant par les mêmes étapes que pour le calcul du premier ordre nous aboutissons aux deux contributions du deuxième ordre

$$g^{(2)\alpha} = 4\pi v_{\mathrm{T}} \mathrm{Im}\left\{\mathrm{Tr}\left[t^{\dagger}t\ \mathcal{W}^{11} + t^{\dagger}r'\ \mathcal{W}^{21}\right]\right\}, \tag{11.11}$$

et

$$g^{(2)\beta} = 4\pi^2 \mathrm{Tr}\left\{\mathrm{Re}[\mathcal{V}^{11}t^{\dagger}t\mathcal{V}^{11} + 2\mathcal{V}^{11}t^{\dagger}r'\mathcal{V}^{21} + \mathcal{V}^{12}r'^{\dagger}r'\mathcal{V}^{21}]\right\}. \tag{11.12}$$

où nous avons introduit la matrice $\mathcal{W}$ dont les éléments de matrice sont donnés par

$$\mathcal{W}^{\bar{l}1}_{\bar{a}a} = \sum_{\bar{\bar{l}}=1}^{2} \int_{\varepsilon_1^{(\mathrm{t})}}^{\infty} \frac{\mathrm{d}\bar{\bar{\varepsilon}}}{\varepsilon^{+} - \bar{\bar{\varepsilon}}} \sum_{\bar{\bar{a}}} [V_{\mathrm{T}}]^{\bar{l},\bar{\bar{l}}}_{\bar{a}\bar{\bar{a}}}\,(\varepsilon, \bar{\bar{\varepsilon}})\, [V_{\mathrm{T}}]^{\bar{\bar{l}}1}_{\bar{\bar{a}}a}\,(\bar{\bar{\varepsilon}}, \varepsilon),$$

avec $[V_{\mathrm{T}}]^{\bar{l},\bar{\bar{l}}}_{\bar{a}\bar{\bar{a}}}\,(\varepsilon, \bar{\bar{\varepsilon}})$ l'élément de matrice du potentiel de la pointe entre deux états de diffusion à deux énergies différentes ε et $\bar{\bar{\varepsilon}}$. Il est important de noter que si nous considérons une pointe locale l'obtention de la contribution totale englobant tout les termes d'ordres supérieurs est possible. Dans une telle circonstance nous avons montré (Chapitre 4) que la conductance SGM subit une saturation à des potentiels très forts i.e beaucoup plus grand que l'énergie de Fermi des électrons.

11.3 Extraction de la PLDOS sur une marche de conductance pour une pointe locale

Pour relier la correction de premier ordre de la théorie de perturbation [11] pour la conductance en présence de la pointe aux propriétés électroniques locales nous avons exploité [69] la forme asymptotique des fonctions propres de diffusion. Pour un QPC non désordonné celle-ci reste valable à toute position dans le système sauf à l'intérieur du contact. Dans ce cas, nous avons trouvé [69] que si le QPC est réglé sur une marche de conductance, alors la correction du premier ordre due au potentiel de la pointe est proportionnelle à la PLDOS à une modulation sinusoïdale près, qui est due à des oscillations Fabry-Perot entre la pointe SGM et le QPC

$$g^{(1)}(\mathbf{r}_{\mathrm{T}}) = 2\mathcal{R}_1 \sin[2\alpha_{1,\varepsilon_{\mathrm{F}},1}(\mathbf{r}_{\mathrm{T}})]\rho_{1\varepsilon_{\mathrm{F}}}(\mathbf{r}_{\mathrm{T}})\,, \tag{11.13}$$

avec

$$\rho_{1\varepsilon}(\mathbf{r}) = 2\pi \sum_{a=1}^{N} |\Psi^{(0)}_{1,\varepsilon,a}(\mathbf{r})|^2\,, \tag{11.14}$$

$\mathcal{R}_1$ est le coefficient de réflexion du QPC, $\alpha_{1,\varepsilon_{\mathrm{F}},1}$ est la phase de la fonction de diffusion et N le nombre de canaux ouverts à l'énergie ε. Dans le cas d'un QPC entouré d'un gaz d'électron désordonné, la relation précédente ne s'applique pas dans la région où le désordre est présent. Néanmoins, nous avons montré numériquement que pour un désordre faible, de sorte à ne permettre que des processus de diffusion à petit angle, l'écoulement des électrons peut être caractérisé par des oscillations régulières similaires

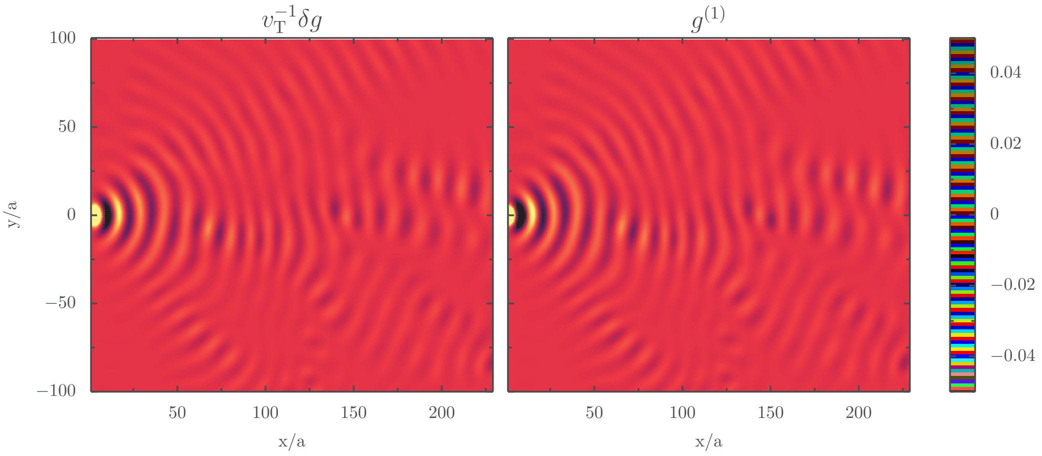

Figure 11.2: Panel de gauche : la réponse SGM est numériquement calculée pour une pointe locale de potentiel ($v_{\rm T} = \varepsilon_{\rm F} a^2/4$) sur la première marche de conductance. Panel de droite : la forme analytique de $g^{(1)}$ est évaluée. Le QPC est situé au coté gauche de chaque image.

à celles que nous observons en absence de désordre [70]. Cela est illustré dans la Fig. 11.2. Dans le panel de gauche de cette figure la réponse SGM est calculée à la première marche de conductance pour un faible potentiel de pointe $v_{\rm T} = \varepsilon_{\rm F} a^2/4$. Dans le panel de droite le membre droite de l'Eq. (11.13) est évalué en utilisant Kwant. Cela montre bien que l'Eq. (11.13) est valide pas seulement pour un système non-désordonné mais aussi pour un système présentant un désordre faible.

11.4 Extraction de la PLDOS sur un plateau de conductance pour une pointe locale

Si le QPC a une transmission parfaitement quantifiée, le terme de premier ordre discuté dans la section précédente s'avère être nul. Par conséquent la correction de second ordre doit être considéré. Il a été montré que ce deuxième terme est exactement proportionnel au carré de la PLDOS pour un système parfaitement symétrique et invariant par renversement du temps [15].

Considérant une pointe locale et admettant une transmission parfaite il est possible de montrer que la correction au second ordre $g^{(2)}$ se réduit a

$$g^{(2)} = -4\pi^2 \mathrm{Tr}\left\{\mathrm{Re}[t^\dagger t \mathcal{V}^{12}\mathcal{V}^{21}]\right\}. \tag{11.15}$$

En tenant compte du fait que, pour un système invariant par renversement de temps, les fonctions propres de diffusion provenant des deux réservoirs sont le complexe conjugué l'une de l'autre, nous avons démontré que la correspondance énoncée dans [15] pour une géométrie symétrique haut-bas gauche-droite reste valable même en absence d'une telle symétrie spatiale [69], et ainsi généralisé la correspondance entre $g^{(2)}$ et la PLDOS $\rho_{1\varepsilon_\mathrm{F}}$

$$g^{(2)}(\mathbf{r}_\mathrm{T}) = -\rho^2_{1\varepsilon_\mathrm{F}}(\mathbf{r}_\mathrm{T}), \tag{11.16}$$

pour $\mathbf{r}_\mathrm{T}$ à droite du QPC.

Comme illustration de cette relation de correspondance nous présentons dans la Fig. 11.3 l'opposé de la correction du deuxième ordre pour les deux premiers plateaux (a) pour le premier (d) pour le deuxième et la PLDOS (b) pour le premier plateau et (e) pour le deuxième. La différence entre les deux quantités est de l'ordre de 10^{-4}, elle est montrée dans la ligne de bas de la figure.

Dans le cas réaliste d'une transmission qui n'est pas parfaitement quantifiée, nous avons utilisé une théorie de perturbation par rapport à un petit coefficient de réflexion pour évaluer le rapport entre la correction dominante de la conductance et le carré de la PLDOS [69]. Nous avons trouvé que la relation se dégrade proportionnellement à la racine carré de la déviation de la conductance par rapport à la valeur quantifiée. Ceci signifie que la correspondance entre la réponse SGM et la PLDOS est très sensible à la déviation par rapport à la transmission parfaite. Ce résultat a été vérifié numériquement [69].

Sachant que les déviations de la relation parfaite montrent des oscillations spatiales de période correspondant à une demi longueur d'onde électronique, nous avons constaté que la PLDOS moyennée sur un disque avec la taille d'une longueur d'onde de Fermi autour de la position de la pointe est directement reliée à la moyenne du changement de conductance sur le même disque. Pour démontrer ce phénomène nous avons procédé à des simulations numériques utilisant le logiciel KWANT [30]. Ce résultat important nous permet de prédire que la PLDOS peut être extraite de la réponse SGM avec une résolution spatiale réduite dans la situation réaliste de quantification non parfaite de la conductance.

11.5 Liaison entre la réponse SGM et la PLDOS pour une pointe non locale

Dans la section ci-dessus la pointe a été considérée comme étant locale. Bien que des expériences très récentes [76] ont pu être réalisées dans des

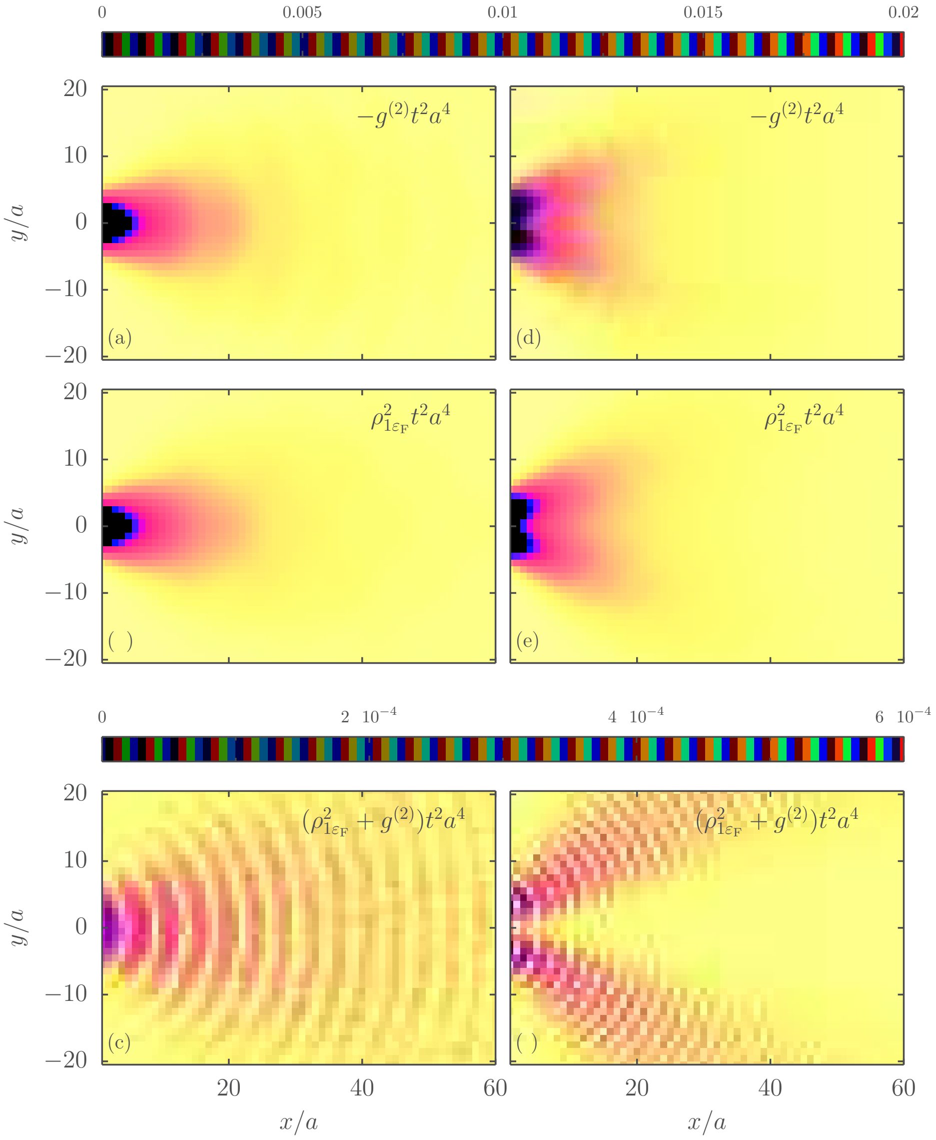

Figure 11.3: Ligne de haut : $-g^{(2)}$ est calculée en changeant la position de la pointe sur le coté droite d'un QPC pour le premier (a) et le deuxième (d) plateau. Ligne du centre: le carré de la PLDOS dans la même région que précédemment pour le premier (b) et le deuxième (e) plateau. Ligne de bas: la différence entre les deux premières lignes.

gaz d'atomes ultra-froids avec une perturbation produite par un rayon laser suffisamment focalisé et dans des conditions d'application de la théorie de perturbation [11], la quasi totalité des expériences SGM ne sont pas situées dans le régime d'une pointe locale et peu invasive. Nous avons alors pris en compte l'élargissement spatial de la pointe AFM, et mené à bien des simulations numériques de la réponse SGM. Les résultats numériques montrent que pour des diamètres de la pointe plus grands que la longueur d'onde électronique, la correspondance entre la réponse SGM et la PLDOS est dégradée [69].

11.6 Liaison entre la réponse SGM et la transformé de Hilbert de la densité locale à 1D et 2D

Dans la référence [48] une relation de correspondance différente de celle que nous avons proposés dans les sections précédentes à été proposée. Dans cette référence la réponse SGM pour une pointe locale avec potentiel

$$V_{\mathrm{T}}(\mathbf{r}) = v_{\mathrm{T}}\delta(\mathbf{r}-\mathbf{r}_{\mathrm{T}})$$

à été reliée à la transformé de Hilbert de la densité locale électronique qui est proportionnelle à la partie réelle de la fonction de Green diagonale. Cette correspondance à été rigoureusement démontrée pour un problème de diffusion unidimensionnelle. Nous avons retrouvé ce résultat en suivant la référence [56]. Le résultat s'écrit

$$\delta g = 2v_{\mathrm{T}} g^{(0)} \mathrm{Re}(\mathcal{G}^{(0)}(\mathbf{r}_{\mathrm{T}}, \mathbf{r}_{\mathrm{T}}, \varepsilon)), \tag{11.17}$$

ou $g^{(0)}$ est la conductance non-perturbée du système. D'autre part, nous avons montré qu'il y a un résultat général concernant le changement de la densité locale dê à une pointe locale pouvant s'écrire pour toute dimension en premier ordre au potentiel de la pointe comme suit

$$\rho_{l\varepsilon}(\mathbf{r}_{\mathrm{T}}) - \rho_{l\varepsilon}^{(0)}(\mathbf{r}_{\mathrm{T}}) = 2v_{\mathrm{T}} \rho_{l\varepsilon}^{(0)}(\mathbf{r}_{\mathrm{T}}) \mathrm{Re}(\mathcal{G}^{(0)}(\mathbf{r}_{\mathrm{T}}, \mathbf{r}_{\mathrm{T}}, \varepsilon)), \tag{11.18}$$

Dans le cas d'une seule dimension d'espace les densités unidimensionnelles sont proportionnelles aux transmissions et cela implique que la même relation (11.18) est vérifiée pour la conductance, exactement comme dans l'Eq. (11.17). N'ayant aucune évidence d'une telle correspondance au dimensions supérieures, nous avons numériquement calculé les quantités à comparer pour une géométrie d'anneau et vérifié que la réponse SGM n'est pas liée à la transformation de Hilbert de la densité locale.

11.7 Dépendance des branches électroniques de l'énergie de Fermi

Dans une expérience récente, nos collègues de l'ETH Zurich [Beat Braem et *al*, communication privée, 2017] ont étudié de quelle manière la location des branches dépend de l'énergie de Fermi des électrons. Dans cette expérience une stabilité des branches à été observée dans les images SGM. Dans le cadre de cette thèse nous avons conduit des simulations numériques qui reproduisent les observations expérimentales. En ayant la possibilité de contrôler la force du désordre -ce qui est difficile en expérience-, nous avons pu comprendre que cette stabilité de branche est observable à partir d'un certain rapport entre le niveau du désordre et l'énergie de Fermi.

Dans la Fig. 11.4, nous montrons des simulations numériques de la PLDOS pour différentes valeurs du rapport entre l'énergie de Fermi et le coefficient adimensionné γ permettant de contrôler le niveau du désordre pour une configuration donnée. Nous observons que lorsque le rapport $\varepsilon_{\mathrm{F}}/\gamma$ devient supérieur ou égal à 1 la location des branches est très robuste. Ce comportement que nous avons choisi de montrer à travers la PLDOS est aussi observé en calculant la réponse SGM. Cela à été fait pour différentes configurations de désordre.

11.8 Méthode basée sur les fonctions de Green pour calculer la conductance d'un diffuseur à taille finie

La façon traditionnelle de calculer la conductance d'un diffuseur en fonction de sa position (la pointe SGM par exemple) nécessite le calcul de la matrice S à toute position du diffuseur. La méthode que nous proposons ici est basée sur la résolution de l'équation de Dyson en ajoutant successivement les sites du réseau sous le diffuseur. Après l'ajout de n sites la fonction de Green $\mathcal{G}^{(n)}$ peut s'exprimer en fonction $\mathcal{G}^{(n-1)}$ comme suit

$$\mathcal{G}^{(n)}(\mathbf{r},\mathbf{r}') = \mathcal{G}^{(n-1)}(\mathbf{r},\mathbf{r}') + v_n \beta^{(n-1)} \mathcal{G}^{(n-1)}(\mathbf{r},\mathbf{r}_n) \mathcal{G}^{(n-1)}(\mathbf{r}_n,\mathbf{r}'), \qquad (11.19)$$

avec

$$\beta^{(n-1)} = \frac{1}{1-\mathcal{G}^{(n-1)}(\mathbf{r}_n,\mathbf{r}_n)},$$

et $\mathbf{r}_n$ étant la position du $n$éme site ajouté.

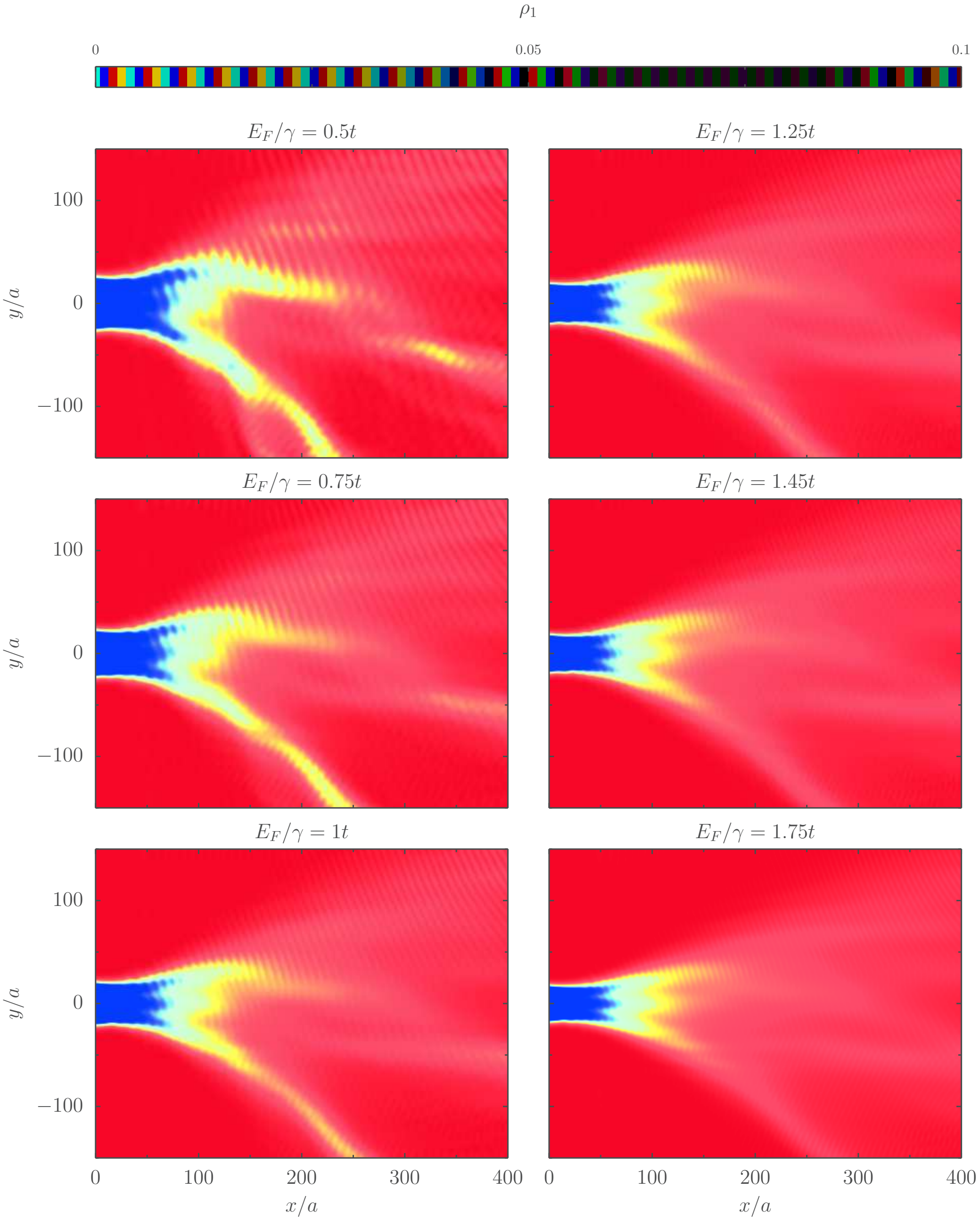

Figure 11.4: PLDOS à des énergies différentes. Le pré-facteur γ du désordre est fixé à $\gamma = 0.2$. Le QPC est positionné au centre gauche de chaque figure.

En introduisant des facteurs Z pouvant être calculés à partir de $\mathcal{G}^{(0)}$, la fonction de Green $\mathcal{G}^{(n)}$ peut être exprimée en fonction de $\mathcal{G}^{(0)}$ comme suit

$$\mathcal{G}^{(n)}(\mathbf{r},\mathbf{r}') = \mathcal{G}^{(0)}(\mathbf{r},\mathbf{r}') + \sum_{k=1}^{n} Z_k^{(n)}(\mathbf{r}')\mathcal{G}^{(0)}(\mathbf{r},\mathbf{r}_k). \tag{11.20}$$

En utilisant cette équation dans l'équation de Lippmann-Schwinger la fonction de diffusion correspondante s'écrit

$$\psi^{(n)}(\mathbf{r}) = \psi^{(0)}(\mathbf{r}) + \sum_{i=1}^{n} Q_{i-1}\Bigg\{ \mathcal{G}^{(0)}(\mathbf{r},\mathbf{r}_i) + \sum_{k=1}^{i-1} Z_k^{(i-1)}(\mathbf{r}_i)\mathcal{G}^{(0)}(\mathbf{r},\mathbf{r}_k)\Bigg\}, \tag{11.21}$$

où les coefficients Q peuvent être construits à partir de la fonction de diffusion non perturbée $\psi^{(0)}$. En suivant une procédure identique à celle permettant d'obtenir les corrections de premier et second ordre en potentiel (voir Sec. 11.2) nous obtenons le changement de la conductance dû au diffuseur comme

$$\delta g = 4\pi \mathrm{Im}\Bigg\{\mathrm{Tr}[t^\dagger t\hat{\mathcal{V}}^{11} + t^\dagger r'\hat{\mathcal{V}}^{21}]\Bigg\} + 4\pi^2 \mathrm{Tr}\Bigg\{\mathrm{Re}[\hat{\mathcal{V}}^{11}t^\dagger t\hat{\mathcal{V}}^{11} + 2\hat{\mathcal{V}}^{11}t^\dagger r'\hat{\mathcal{V}}^{21} + \hat{\mathcal{V}}^{12}r'^\dagger r'\hat{\mathcal{V}}^{21}]\Bigg\}. \tag{11.22}$$

où

$$\hat{\mathcal{V}}^{\bar{l}l}_{\bar{a}a} = \sum_{i=1}^{n} Q_{i-1}\Bigg\{\psi^{(0)*}_{\bar{l}\varepsilon\bar{a}}(\mathbf{r}_i) + \sum_{k=1}^{i-1} Z_k^{(i-1)}(\mathbf{r}_i)\psi^{(0)*}_{\bar{l}\varepsilon\bar{a}}(\mathbf{r}_k)\Bigg\}. \tag{11.23}$$

Pour utiliser la méthode nous proposons l'algorithme suivant

1) Calculer les quantités non perturbées $\mathcal{G}^{(0)}$, $\psi^{(0)}$ et la matricez de diffusion S.

2) Construire les $\mathcal{G}^{(i)}$ et $\psi^{(i)}$ à partir de 1).

3) Construire les coefficients Q and Z à partir de $\mathcal{G}^{(0)}$.

4) Utiliser Eq. (11.22) pour obtenir la conductance à toute position.

11.9 Conclusions et perspectives

Afin de pouvoir extraire les propriétés électroniques locales à travers une nanostructure nous avons étudié la liaison entre la conductance en présence d'une pointe SGM et la densité partielle locale (PLDOS). Pour un QPC opérant dans le régime de quantification de conductance, nous avons montré que la réponse SGM est proportionelle à la PLDOS à une modulation sinusoïdale près lorsque le QPC est réglé sur la première marche de conductance. Dans le cas où le QPC a une transmission entière nous avons généralisé la relation de correspondance entre les deux quantités pour être valable quelque soit le plateau de conductance pour tout système invariant par renversement de temps. Néanmoins, cette correspondance est très sensible à la déviation de la conductance par rapport à ses valeurs entières. Sachant que cette déviation est liée aux oscillions du genre Fabri-Perot présentes dans certains termes des corrections de la conductance, nous avons montré que la relation de correspondance est retrouvée si la PLDOS et la conductance SGM sont moyennées sur une région spatiale d'extension de l'ordre de la longueur d'onde de Fermi. Nous pensons par ailleurs qu'une température modérée pourrait jouer ce rôle de moyennage et alors permettre de retrouver la relation de correspondance. Pour une pointe non locale nous avons montré que la correspondance se dégrade quand l'extension de la pointe est plus grande qu'une demi longueur d'onde électronique.

Dans une partie de cette thèse nous avons étudié la dépendance des branches de l'énergie de Fermi des électrons. Nous avons trouvé que tant que l'énergie de Fermi est plus grande qu'une certaine valeur critique liée au niveau du désordre, les branches sont stables. Une étude quantitative reste à mener pour mieux comprendre ce phénomène. Lors de l'investigation de cette stabilité des branches, nous avons fait des simulations numériques (que nous n'avons pas montré dans ce résumé) pour comprendre l'origine des sauts de phase observés sur les données expérimentales communiqués par nos collègues de l'ETH Zurich. Nos simulations numériques montrent que ces sauts de phase sont dûs aux phénomènes d'interférence entre branches très fines induites par la présence de dures impunités sur la nanostructure étudiée.

D'autre part nous avons étudié la liaison entre la réponse SGM et la transformée de Hilbert de la densité locale. Pour une géométrie unidimensionnelle nous avons trouvé qu'il y a une correspondance entre les deux quantités comme annoncé dans la Ref. [48]. Par contre, pour une géométrie bidimensionnelle nous avons montré qu'une telle correspondance ne peut pas avoir lieu.

Dans le but d'optimiser le calcul de la conductance SGM nous avons proposé une méthode basée sur les fonctions de Green permettant d'obtenir la conductance à toute position de la pointe à partir de la matrice S, les fonctions de diffusion et la fonction de Green de la structure non perturbée; ce qui est avantageux si l'étendu de la pointe est de quelques dizaines de sites du réseau bi-dimensionnel.

Nous avons aussi étudié l'effet du couplage spin orbite sur la réponse SGM. En calculant numériquement la conductance en présence et en absence du couplage pour un QPC ouvrant sur un gaz non-désordonné d'électrons, nous avons retrouvé le résultat obtenu dans [10] montrant que le couplage spin orbite permet une transmission à travers un canal additionnel (qui n'était pas permis en absence de couplage spin orbite) ce qui mène à l'observation d'un écoulement électronique à travers ce dernier. En introduisant le désordre nous nous retrouvons avec un résultat surprenant. En effet nous trouvons que lorsque la structure est désordonnée ces canaux dû au couplage spin orbite ne montrent aucune manifestation apparente. La compréhension d'une telle observation est une tache que nous voulons entretenir dans un futur proche.

Appendix A

Evaluation of the average longitudinal momentum $\mathcal{K}_n$

Here, we calculate the the average longitudinal momentum $\mathcal{K}_n$, which will be used to calculate the conductance of the WNW geometry presented in Chapter 1.

The average longitudinal momentum $\mathcal{K}_n$ is given by

$$\mathcal{K}_n = \frac{w}{\pi} \int_{Q_{n-1}}^{Q_{n+1}} \mathrm{d}q \sqrt{k^2 - q^2}. \tag{A.1}$$

We split $\mathcal{K}_n$ into real (I_n) and imaginary (J_n) parts

$$I_n = \mathrm{Re}[\mathcal{K}_n] = \frac{w}{\pi} \int_{Q_{n-1}}^{k} \mathrm{d}q \sqrt{k^2 - q^2}, \tag{A.2}$$

and

$$J_n = \mathrm{Im}[\mathcal{K}_n] = \frac{w}{\pi} \int_{k}^{Q_{n+1}} \mathrm{d}q \sqrt{k^2 - q^2}. \tag{A.3}$$

To calculate I_n, we perform the following variable change $q = k \sin\theta$, this gives

$$I_n = \frac{w}{\pi} k^2 \int_0^{\cos^{-1} \frac{Q_{n-1}}{k}} \mathrm{d}\theta \sin^2\theta. \tag{A.4}$$

Using the equality $\sin^2\theta = \frac{1}{2}(1 - \cos 2\theta)$, the integral is straightforward, and gives

$$I_n = -\frac{wk^2}{4\pi} \left[\sin[2\cos^{-1} \frac{Q_{n-1}}{k}] - 2\cos^{-1} \frac{Q_{n-1}}{k} \right]. \tag{A.5}$$

For J_n we use the variable change $q = k \cosh a$, leading to

$$J_n = \frac{w}{\pi} k^2 \int_0^{\cosh^{-1} \frac{Q_{n+1}}{k}} \mathrm{d}\theta \sinh^2\theta. \tag{A.6}$$

Using the identity $\sinh^2\theta = \frac{1}{2}(1 - \cosh 2\theta)$, we find

$$J_n = \frac{wk^2}{4\pi}\left[\sinh[2\cosh^{-1}\frac{Q_{n+1}}{k}] - 2\cosh^{-1}\frac{Q_{n+1}}{k}\right]. \tag{A.7}$$

Appendix B

Conductance of the WNW geometry

Here we will show that the formula (1.57) obtained in Ref. [15] is equivalent to that of Ref. [24].

On one hand the denominator of (1.57) can be written as :

$$|D_n|^2 = |K_n + \mathcal{K}_n|^4 + |K_n - \mathcal{K}_n|^4 - 2\mathrm{Re}\{A_n e^{-2iK_nL}\}, \tag{B.1}$$

with

$$A_n = [(K_n + \mathcal{K}_n)(K_n - \mathcal{K}_n)]^2 \tag{B.2}$$

The real part in B.1 can be straightforwardly brought to:

$$\mathrm{Re}\{A_n e^{-2iK_nL}\} = \cos(2K_nL)(|K_n|^2 - |\mathcal{K}_n|^2)^2 - 4K_n^2 J_n^2 + 4\sin(2K_nL)(|K_n|^2 - |\mathcal{K}_n|^2)K_n J_n, \tag{B.3}$$

where $J_n = \mathrm{Im}\{\mathcal{K}_n\}$. Introducing the angle ϕ_n defined by:

$$\tan\phi_n = \frac{2K_nJ_n}{|\mathcal{K}_n|^2 - |K_n|^2}, \tag{B.4}$$

and the quantity

$$V_n = \frac{|K_n + \mathcal{K}_n|^4 + |K_n - \mathcal{K}_n|^4}{4K_n^2J_n^2}, \tag{B.5}$$

it follows that

$$\frac{|D_n|^2}{4K_n^2J_n^2} = \frac{1}{\sin^2\phi_n}(\sin^2\phi_n V_n - 2 + 4\sin^2(K_nL + \phi_n)), \tag{B.6}$$

that is

$$g_n = \frac{4\sin^2\phi_n I_n^2}{J_n^2(V_n\sin^2\phi_n - 2 + 4\sin^2(K_nL + \phi_n))}, \tag{B.7}$$

where $I_n = \mathrm{Re}\{\mathcal{K}_n\}$. Replacing V_n by its expression and noting that

$$\sin^2\phi_n = \frac{4K_n^2J_n^2}{4K_n^2J_n^2 + (|\mathcal{K}_n|^2 - |K_n|^2)^2}, \tag{B.8}$$

g_n can be written as

$$g_n = \frac{16K_n^2I_n^2}{|K_n+\mathcal{K}_n|^4 + |K_n-\mathcal{K}_n|^4 + 2(4K_n^2J_n^2 + (I_n^2+J_n^2-K_n^2)^2)(-1+2\sin^2(\phi_n+K_nL))}. \tag{B.9}$$

Now, using the two following identities

$$|K_n+\mathcal{K}_n|^4 + |K_n-\mathcal{K}_n|^4 = ((I_n-K_n)^2+J_n^2)^2 + ((I_n+K_n)^2+J_n^2)^2, \tag{B.10}$$

and

$$4K_n^2J_n^2 + (I_n^2+J_n^2-K_n^2)^2 = ((I_n-K_n)^2+J_n^2)((I_n+K_n)^2+J_n^2), \tag{B.11}$$

which are easy to check, g_n reduces to:

$$g_n = \frac{4K_n^2I_n^2}{4I_n^2K_n^2 + ((I_n-K_n)^2+J_n^2)((I_n+K_n)^2+J_n^2)\sin^2(\phi_n+K_nL)}, \tag{B.12}$$

for the open channels. For the closed channels it reads

$$g_n = \frac{4\kappa_n^2I_n^2}{4I_n^2\kappa_n^2 + ((I_n-\kappa_n)^2+J_n^2)((I_n+\kappa_n)^2+J_n^2)\sinh^2(\theta_n+\kappa_nL)}, \tag{B.13}$$

with

$$\tan\theta_n = \frac{2\kappa_nJ_n}{\kappa_n^2+I_n^2+J_n^2}, \tag{B.14}$$

and $\kappa_n = i\sqrt{k^2-(\frac{n\pi}{w})^2}$. This corresponds to the conductance formula obtained in [24] for the WNW geometry. Notice that in Ref. [24] the formula was written with typing errors.

Appendix C

Evaluation of the energy integrals involved in the corrections to the current density

When calculating the conductance corrections in Chapter 3, we encounter the following energy integrals:

$$I_1^s(\varepsilon) = \int_{\varepsilon_1^{(t)}}^{\infty} \frac{\mathrm{d}\bar{\varepsilon}}{\varepsilon^+ - \bar{\bar{\varepsilon}}} F(\bar{\bar{\varepsilon}}) e^{si\bar{\bar{k}}x}, \tag{C.1}$$

and

$$I_2^{(s,\sigma)}(\varepsilon) = \int_{\varepsilon_1^{(t)}}^{\infty} \frac{\mathrm{d}\bar{\varepsilon}}{\varepsilon^- - \bar{\varepsilon}} \frac{\mathrm{d}\bar{\bar{\varepsilon}}}{\varepsilon^+ - \bar{\varepsilon}} H(\bar{\varepsilon}, \bar{\bar{\varepsilon}}) e^{i(\sigma\bar{k} + s\bar{\bar{k}})x}, \tag{C.2}$$

where smooth dependence of F and H on the energy variables is assumed.

Changing the energy variables to momenta, the integrals become

$$I_1^s(\varepsilon) = \int_0^{\infty} \frac{-2\bar{\bar{k}}\mathrm{d}\bar{\bar{k}}}{[\bar{\bar{k}} + k + i\bar{\eta}][\bar{\bar{k}} - (k + i\bar{\eta})]} F(\bar{}) e^{si\bar{\bar{k}}x}, \tag{C.3}$$

and

$$I_2^{(s,\sigma)}(\varepsilon) = \int_0^{\infty} \frac{-2\bar{k}\mathrm{d}\bar{k}}{[\bar{k} + k + i\bar{\eta}][\bar{k} - (k - i\bar{\eta})]} \frac{-2\bar{\bar{k}}\mathrm{d}\bar{\bar{k}}}{[\bar{\bar{k}} + k + i\bar{\eta}][\bar{\bar{k}} - (k + i\bar{\eta})]} H(\bar{\varepsilon}, \bar{\bar{\varepsilon}}) e^{i(\sigma\bar{k} + s\bar{\bar{k}})x}. \tag{C.4}$$

To evaluate the energy integral I_1^s we use one of the two quadrants of the complex plane depicted in Fig. C.1. If $s = -1$, it is appropriate to chose Q_u, in order to ensure that (i) the integration along the corresponding quarter vanishes as $|\bar{k}|$ tends to ∞; and (ii) the contribution along the imaginary axis vanishes in the limit of x tending to infinity. In contrast if $s = +$, Q_d should be considered.

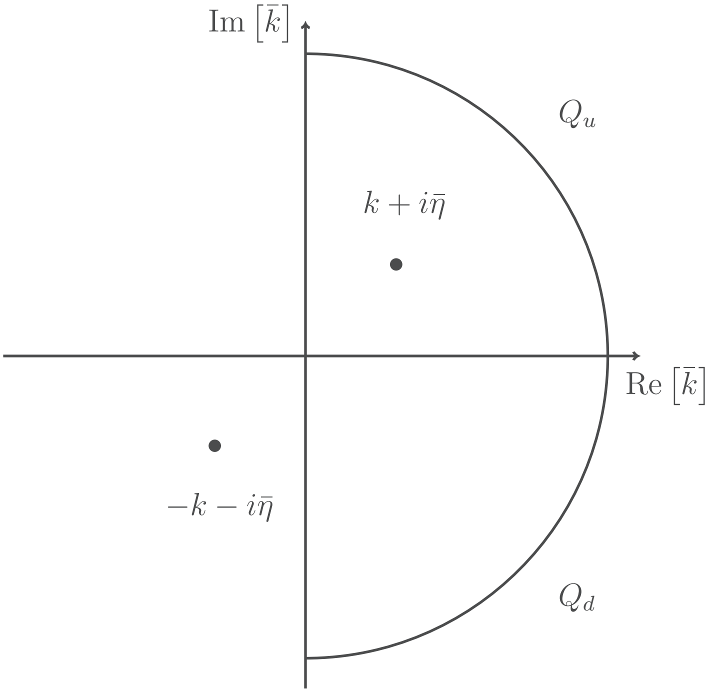

Figure C.1: The complex plane of $\bar{\bar{k}}$ used to calculate I_1, and the $\bar{\bar{k}}$ integral of I_2 is shown. The orientation of the contours is dictated by the real axis orientation. The poles of the integral are represented by the dots.

Since there is no pole in Q_d, we have $I_1^- = 0$, according to the residue theorem. On the other hand the pole $k + i\bar{\eta}$ lies in Q_u, therefore the application of the residue theorem gives

$$I_1^+(\varepsilon) = -2\pi i F(\varepsilon) e^{ikx}. \tag{C.5}$$

Similarly, the σ-integral of I_2 (the $\bar{k}$ integral) vanishes for $\sigma = +$, since there is no pole in Q_u (see Fig. C.2). Therefore, I_2 vanishes if $\sigma = +$ and/or $s = -$. However, if $\sigma = -1$ and $s = 1$ the residue theorem gives

$$I_2^{(+,-)}(\varepsilon) = 4\pi^2 H(\varepsilon, \varepsilon). \tag{C.6}$$

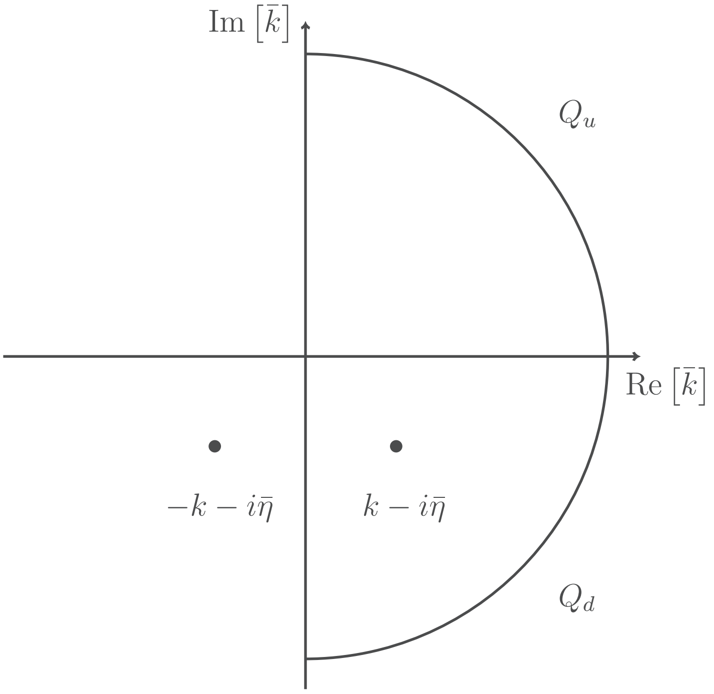

Figure C.2: The complex plane of $\bar{k}$ used to calculate I_2 is shown. The orientation of the contours is dictated by the real axis orientation.

C.1 First order correction to the current density

As we have seen in the main text, the first order correction to the current density of states coming from the left lead is

$$\delta^{(1)} J_{1\varepsilon a}(\mathbf{r}) = 2 \sum_{\bar{l}=1}^{2} \mathrm{Re} \left\{ \int_{\varepsilon_1^{(\mathrm{t})}}^{\infty} \frac{\mathrm{d}\bar{\varepsilon}}{\varepsilon^{+} - \bar{\varepsilon}} \sum_{\bar{a}=1}^{\bar{N}} [j(\mathbf{r})]_{a\bar{a}}^{1,\bar{l}} (\varepsilon, \bar{\varepsilon}) \; [V_{\mathrm{T}}]_{\bar{a}a}^{\bar{l},1} (\bar{\varepsilon}, \varepsilon) \right\} , \quad \text{(C.7)}$$

with

$$[j(\mathbf{r})]_{\bar{a}a}^{11} (\varepsilon, \bar{\varepsilon}) = \frac{e}{2h} \sum_{b=1}^{\hat{N}} \left(\sqrt{\frac{\bar{k}_b}{k_b}} + \sqrt{\frac{k_b}{\bar{k}_b}} \right) t_{ba}^{*} \bar{t}_{b\bar{a}} \exp\left[i(\bar{k}_b - k_b)x \right], \quad \text{(C.8)}$$

and

$$\begin{aligned} [j(\mathbf{r})]_{\bar{a}a}^{12} (\varepsilon, \bar{\varepsilon}) &= \frac{e}{2h} \left(\sqrt{\frac{k_{\bar{a}}}{\bar{k}_{\bar{a}}}} - \sqrt{\frac{\bar{k}_{\bar{a}}}{k_{\bar{a}}}} \right) t_{\bar{a}a}^{*} \exp\left[-i(\bar{k}_{\bar{a}} + k_{\bar{a}})x \right] \\ &+ \frac{e}{2h} \sum_{b=1}^{\hat{N}} \left(\sqrt{\frac{\bar{k}_b}{k_b}} + \sqrt{\frac{k_b}{\bar{k}_b}} \right) t_{ba}^{*} \bar{r}'_{b\bar{a}} \exp\left[i(\bar{k}_b - k_b)x \right]. \quad \text{(C.9)} \end{aligned}$$

In (C.7), if $\bar{l} = 2$ the energy integral of the first term of $[j(\mathbf{r})]_{\bar{a}a}^{12}$ is of type (C.1) with $s = -$, therefore the resulting energy integral is 0. The remaining terms are of type I_1^{+}. Using Eq. (C.5), the resulting energy integrals are

$$-2\pi i \frac{e}{h} (t^{\dagger} t \mathcal{V}^{11})_{aa}, \quad \text{(C.10)}$$

for $\bar{l} = 1$, and

$$-2\pi i \frac{e}{h} (t^{\dagger} r' \mathcal{V}^{21})_{aa}, \quad \text{(C.11)}$$

for $\bar{l} = 2$.

C.2 Second order correction to the current density

In the main text, we have shown how can the α-type of the second order correction to the current density be obtained from the result of calculation of the first order current density correction. Here, we calculate the β-like correction, given by Eq. (3.25).

The matrix elements of $[j_{1/2}]$ are straightforwardly obtained by plugging the scattering wave-functions (11.3) in Eq. (3.26), they read

$$\begin{aligned}
[j_{1/2}]^{11}_{a\bar{a}}(\varepsilon,\bar{\varepsilon}) &= \frac{e}{2h}\sum_{b=1}^{\hat{N}}\sqrt{\frac{\bar{k}_b}{k_b}}\; t^{*}_{ba}\bar{t}_{b\bar{a}}\; e^{i(\bar{k}_b-k_b)x}\,, \\
[j_{1/2}]^{12}_{a\bar{a}}(\varepsilon,\bar{\varepsilon}) &= \frac{e}{2h}\left\{-\sqrt{\frac{\bar{k}_{\bar{a}}}{k_{\bar{a}}}}\; t^{*}_{\bar{a}a}\; e^{-i(\bar{k}_{\bar{a}}+k_{\bar{a}})x}+\sum_{b=1}^{\hat{N}}\sqrt{\frac{\bar{k}_b}{k_b}}\; t^{*}_{ba}\bar{r}'_{b\bar{a}}\; e^{i(\bar{k}_b-k_b^{-})x}\right\}, \\
[j_{1/2}]^{21}_{a\bar{a}}(\varepsilon,\bar{\varepsilon}) &= \frac{e}{2h}\left\{\sqrt{\frac{\bar{k}_a}{k_a}}\; \bar{t}^{*}_{a\bar{a}}\; e^{i(\bar{k}_a+k_a)x}+\sum_{b=1}^{\hat{N}}\sqrt{\frac{\bar{k}_b}{k_b}}\; r'^{*}_{ba}\bar{t}_{b\bar{a}}\; e^{i(\bar{k}_b-k_b)x}\right\}, \\
[j_{1/2}]^{22}_{a\bar{a}}(\varepsilon,\bar{\varepsilon}) &= \frac{e}{2h}\left\{-\delta_{a\bar{a}}\sqrt{\frac{\bar{k}_a}{k_a}}\; e^{-i(\bar{k}_{\bar{a}}-k_a)x}+\sqrt{\frac{\bar{k}_a}{k_a}}\; \bar{r}'_{a\bar{a}}e^{i(\bar{k}_a+k_a)x}\right. \\
&\qquad \left.-\sqrt{\frac{\bar{k}_{\bar{a}}}{k_a}}\; r'^{*}_{\bar{a}a}\; e^{-i(\bar{k}_{\bar{a}}+k_{\bar{a}})x}+\sum_{b=1}^{\hat{N}}\sqrt{\frac{\bar{k}_b}{k_b}}\; r'^{*}_{ba}\bar{r}'_{b\bar{a}}\; e^{i(\bar{k}_b-k_b)x}\right\}.
\end{aligned} \tag{C.12}$$

The first terms of $[j_{1/2}]^{12}$ and $[j_{1/2}]^{21}$ leads respectively to energy integrals of types $I_2^{(-,+)}$ and $I_2^{(+,+)}$, and therefore vanish according to (C.6), stating that only integrals of type $I_2^{(+,-)}$ are non zero. Similarly, the first three terms of $[j_{1/2}]^{22}$ leads to vanishing energy integrals, respectively of types $I_2^{(-,+)}$, $I_2^{(+,+)}$ and $I_2^{(-,+)}$. By consequence, only the last terms of $[j_{1/2}]^{12}$, $[j_{1/2}]^{21}$ and $[j_{1/2}]^{22}$ in addition to $[j_{1/2}]^{11}$ have to be considered. The energy integrals due to these terms are obtained using (C.6). They reds respectively,

$$4\pi^2\frac{e}{2h}(\mathcal{V}^{11}t^{\dagger}t\mathcal{V}^{11})_{aa}, \tag{C.13}$$

$$4\pi^2\frac{e}{2h}(\mathcal{V}^{11}t^{\dagger}r'\mathcal{V}^{21})_{aa}, \tag{C.14}$$

$$4\pi^2\frac{e}{2h}(\mathcal{V}^{12}t^{\dagger}t\mathcal{V}^{11})_{aa}, \tag{C.15}$$

and

$$4\pi^2\frac{e}{2h}(\mathcal{V}^{12}t^{\dagger}t\mathcal{V}^{21})_{aa}. \tag{C.16}$$

The resulting correction to the current density reads

$$\delta^{(2)} J^{\beta}_{1\varepsilon a} = 4\pi^2 \frac{e}{h} \mathrm{Re}(\mathcal{V}^{11} t^{\dagger} t \mathcal{V}^{11} + 2\mathcal{V}^{11} t^{\dagger} r' \mathcal{V}^{21} + \mathcal{V}^{12} t^{\dagger} t \mathcal{V}^{21})_{aa}, \tag{C.17}$$

where we have used the fact that $(\mathcal{V}^{11} t^{\dagger} r' \mathcal{V}^{21})_{aa}$ and $(\mathcal{V}^{12} t^{\dagger} t \mathcal{V}^{11})_{aa}$ have the same real part.

Appendix D

Energy dependent branches

Here we complement the discussion of Chapter 9 by presenting further numerical data of the energy dependent branching flow.

Here, either the Fermi energy ε_{F} or the disorder strength γ are changed, and different disorder configurations are used (see Fig. D.1).

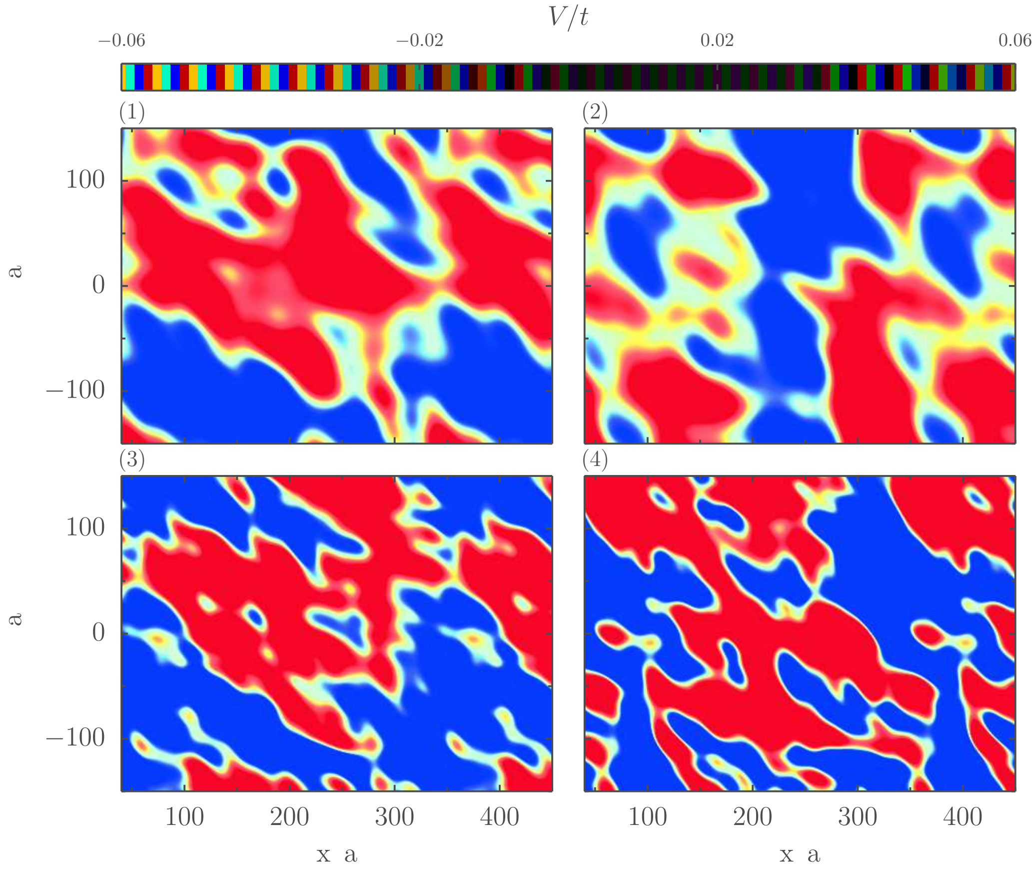

Figure D.1: Four disorder configurations are generated using the method presented in 1.13.2. The corresponding elastic mean free paths are given in Appendix E.

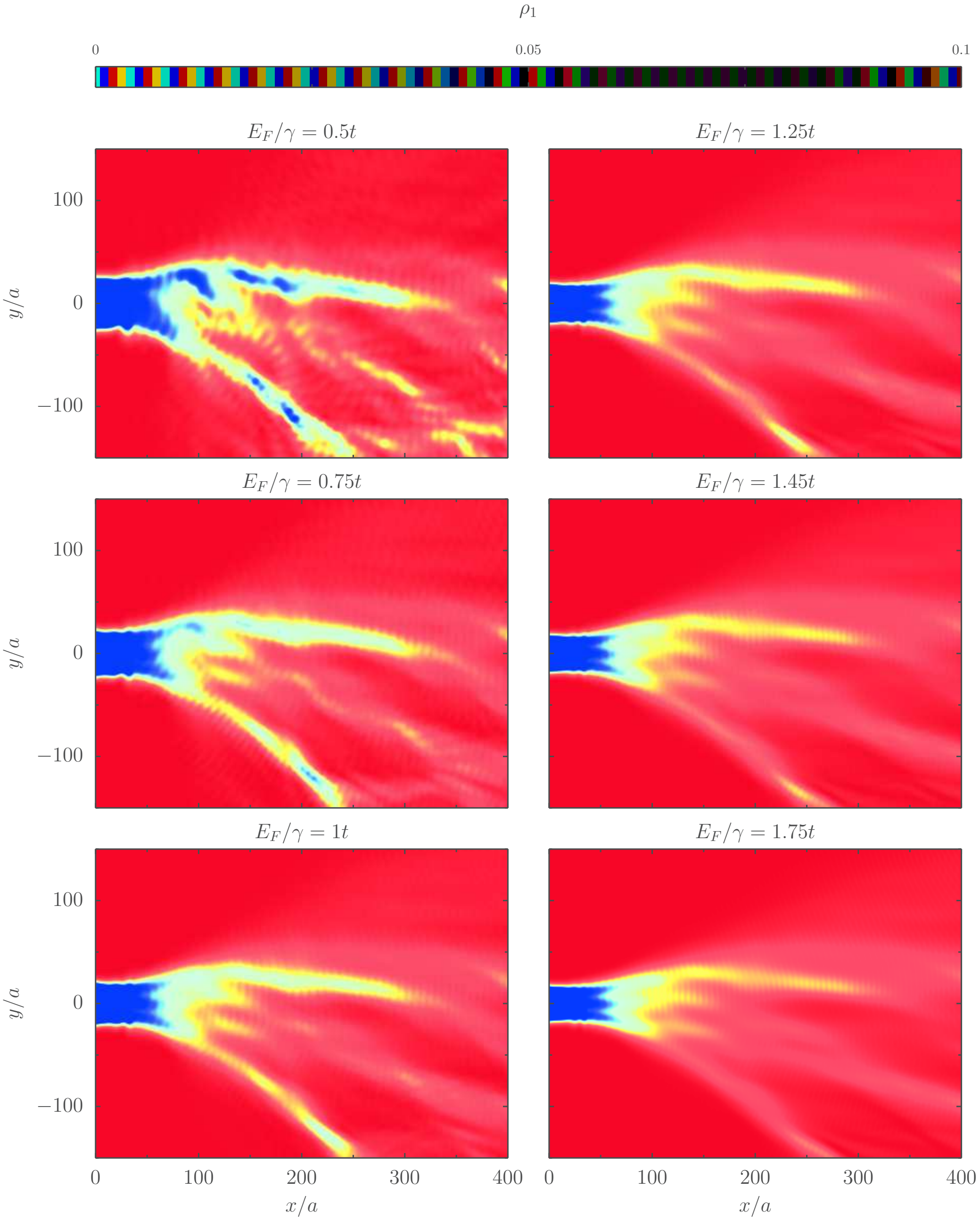

Figure D.2: PLDOS at different energies for configuration 3. The disorder strength γ is fixed at $\gamma = 0.2$.

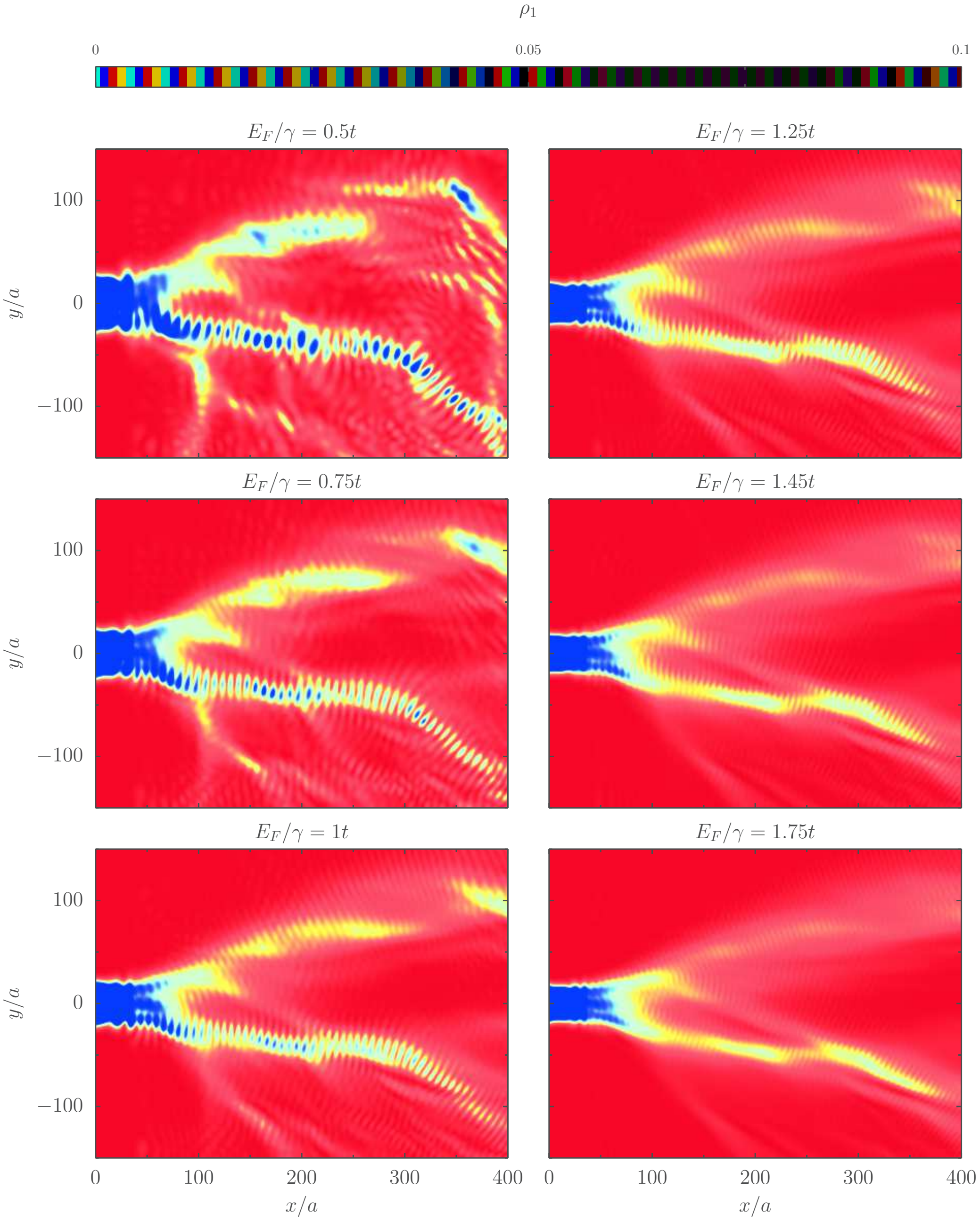

Figure D.3: PLDOS at different energies for configuration 4. The disorder strength γ is held at $\gamma = 0.2$.

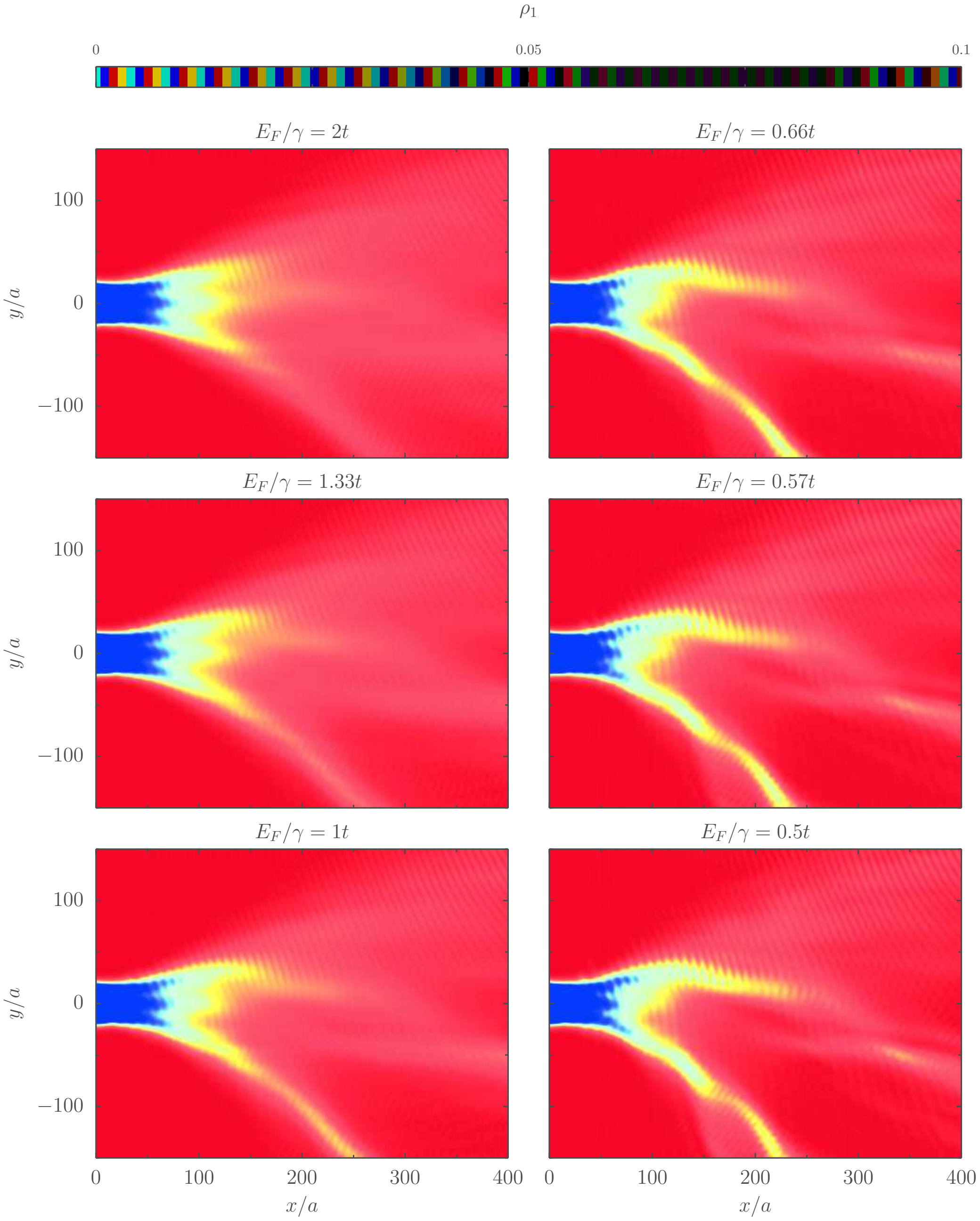

Figure D.4: PLDOS at different disorder strengths for configuration 1. The Fermi energy is held at $\varepsilon_F = 0.2$.

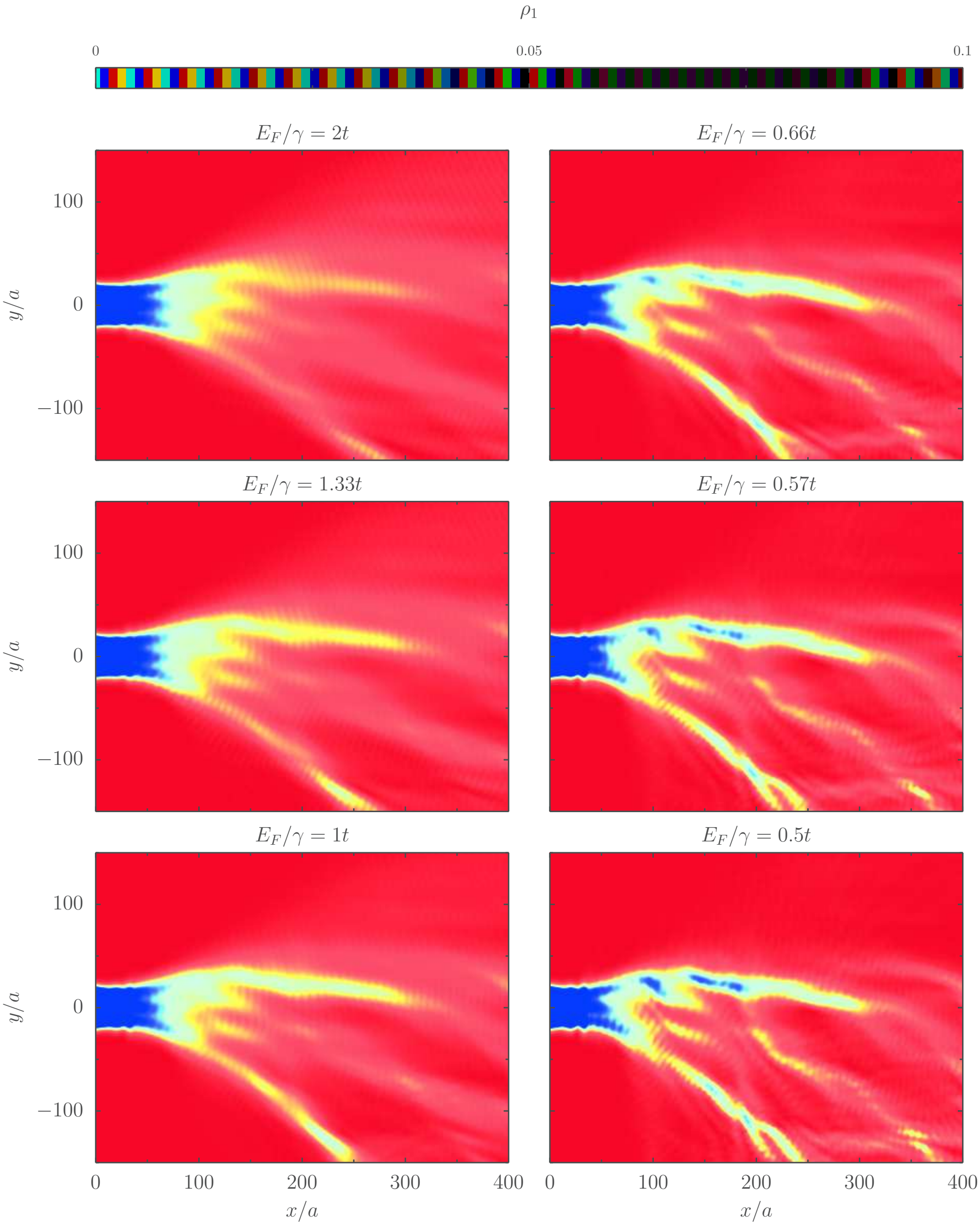

Figure D.5: The same data as in Fig. D.4 for configuration (3).

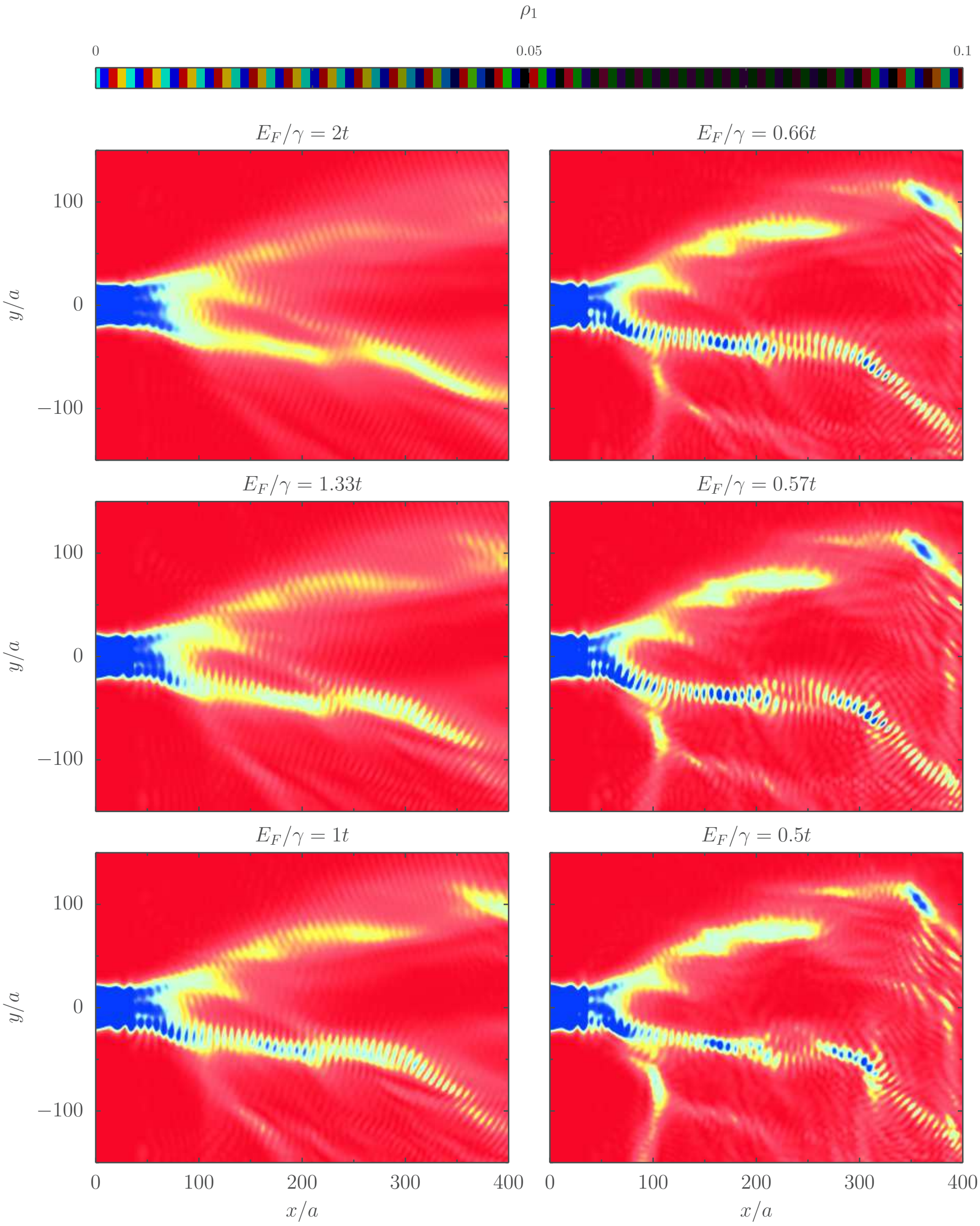

Figure D.6: The same data as in Fig. D.4 for configuration (4).

Appendix E

Characteristics of the disorder realizations used in Chapter 9

Here, we give the elastic mean free paths for the disorder configurations used in Chapter 9. These values are obtained using the Fermi golden rule (1.82). The corresponding transport mean free paths l_T are two orders of magnitude bigger.

According to (1.82), the elastic mean free path l and therefore, the transport mean free path scale with the disorder strength such that $l \propto 1/\gamma^2$ and $l_T \propto 1/\gamma^2$.

In the following tables, the elastic mean free paths are given for the four disorder configurations (see Fig. D.1) at different Fermi energies.

Table E.1: The elastic mean free paths l for configuration (1) are given for $\gamma = 1$ and varied ε_F.

ε_F/t	l/a
0.1	172.56
0.15	211.34
0.2	244.04
0.25	272.84
0.3	298.88
0.35	322.83
0.4	345.12

Table E.2: The elastic mean free paths l for configuration (2) are given for $\gamma = 1$ and varied ε_F.

ε_F/t	l/a
0.1	148.33
0.15	181.67
0.2	209.78
0.25	234.54
0.3	256.92
0.35	277.51
0.4	296.67

Table E.3: The elastic mean free path l for configuration (3) are given for $\gamma = 1$ and varied ε_F.

ε_F/t	l/a
0.1	103.31
0.15	126.54
0.2	146.11
0.25	163.36
0.3	178.95
0.35	193.24
0.4	206.64

Table E.4: The elastic mean free path l for configuration (4) are given for $\gamma = 1$ and varied ε_F.

ε_F/t	l/a
0.1	47.28
0.15	57.91
0.2	66.87
0.25	74.76
0.3	81.90
0.35	88.46
0.4	94.57

References

[1] T. Ihn. *Semiconductor Nanostructures, Quantum States and Electronic Transport*. OXFORD University press, New York, 2010.

[2] B. J. van Wees, H. van Houten, C. W. J. Beenakker, J. G. Williamson, L. P. Kouwenhoven, D. van der Marel, and C. T. Foxon. Quantized conductance of point contacts in a two-dimensional electron gas. *Phys. Rev. Lett.*, 60:848–850, Feb 1988.

[3] Yuli V. Nazarov and Yaroslav M. Blanter. *Quantum transport introduction to Nanoscience*. Cambridge university Press, New York, 2009.

[4] M. A. Topinka, B. J. LeRoy, S. E. J. Shaw, E. J. Heller, R. M. Westervelt, K. D. Maranowski, and A. C. Gossard. Imaging coherent electron flow from a quantum point contact. *Science*, 289(5488):2323–2326, 2000.

[5] M. A. Topinka, B. J. LeRoy, R. M. Westervelt, S. E. J. Shaw, R. Fleischmann, E. J. Heller, K. D. Maranowski, and A. C. Gossard. Coherent branched flow in a two-dimensional electron gas. *Nature*, 410:183, 2001.

[6] M. G. Pala, S. Baltazar, F. Martins, B. Hackens, H. Sellier, T. Ouisse, V. Bayot, and S. Huant. Scanning gate microscopy of quantum rings: effects of an external magnetic field and of charged defects. *Nanotechnology*, 20:264021, 2009.

[7] Damien Cabosart. *Coherent transport and scanning gate microscopy in graphene devices*. PhD thesis, Université catholique de Louvain, 2016.

[8] R. Steinacher, A. A. Kozikov, C. Rössler, C. Reichl, W. Wegscheider, K. Ensslin, and T. Ihn. Scanning gate imaging in confined geometries. *Phys. Rev. B*, 93:085303, Feb 2016.

[9] Richard Steinacher. *Scanning gate imaging in confined geometries*. PhD thesis, ETH Zurich, 2016.

[10] M. P. Nowak, K. Kolasiński, and B. Szafran. Signatures of spin-orbit coupling in scanning gate conductance images of electron flow from quantum point contacts. *Phys. Rev. B*, 90:035301, Jul 2014.

[11] Rodolfo A. Jalabert, Wojciech Szewc, Steven Tomsovic, and Dietmar Weinmann. What is measured in the scanning gate microscopy of a quantum point contact? *Phys. Rev. Lett.*, 105:166802, Oct 2010.

[12] Rodolfo A. Jalabert. *The semiclassical tool in mesoscopic physics, in New directions in quantum chaos.* IOS Press, Amsterdam, 2000.

[13] B Kramer and A MacKinnon. Localization: theory and experiment. *Reports on Progress in Physics*, 56(12):1469, 1993.

[14] P. A. Mello and N. Kumar. *Quantum Transport in Mesoscopic Systems.* Oxford University Press, 2004.

[15] Cosimo Gorini, Rodolfo A. Jalabert, Wojciech Szewc, Steven Tomsovic, and Dietmar Weinmann. Theory of scanning gate microscopy. *Phys. Rev. B*, 88:035406, Jul 2013.

[16] Ryogo Kubo, Mario Yokota, and Sadao Nakajima. Statistical-mechanical theory of irreversible processes. ii. response to thermal disturbance. *Journal of the Physical Society of Japan*, 12(11):1203–1211, 1957.

[17] Rolf Landauer. Electrical resistance of disordered one-dimensional lattices. *Philosophical Magazine*, 21(172):863–867, 1970.

[18] Daniel S. Fisher and Patrick A. Lee. Relation between conductivity and transmission matrix. *Phys. Rev. B*, 23:6851–6854, Jun 1981.

[19] M. Büttiker. Four-terminal phase-coherent conductance. *Phys. Rev. Lett.*, 57:1761–1764, Oct 1986.

[20] A. D. Stone and A. Szafer. What is measured when you measure a resistance? - the landauer formula revisited. *IBM Journal of Research and Development*, 32(3):384–413, May 1988.

[21] Y. Imry. *Physics of Mesoscopic Systems, in directions in condensed matter physics.* World Scientific Press, Singapore, 1986.

[22] R. Landauer. Electrical transport in open and closed systems. *Zeitschrift für Physik B Condensed Matter*, 68(2):217–228, Jun 1987.

[23] Yigal Meir and Ned S. Wingreen. Landauer formula for the current through an interacting electron region. *Phys. Rev. Lett.*, 68:2512–2515, Apr 1992.

[24] Aaron Szafer and A. Douglas Stone. Theory of quantum conduction through a constriction. *Phys. Rev. Lett.*, 62:300–303, Jan 1989.

[25] L. I. Glazman, G. B. Lesovik, D. E. Khmel'Nitskiǐ, and R. I. Shekhter. Reflectionless quantum transport and fundamental ballistic-resistance steps in microscopic constrictions. *Soviet Journal of Experimental and Theoretical Physics Letters*, 48:238, August 1988.

[26] J.N.L. Connor. On the analytical description of resonance tunnelling reactions. *Molecular Physics*, 15(1):37–46, 1968.

[27] M. Büttiker. Quantized transmission of a saddle-point constriction. *Phys. Rev. B*, 41:7906–7909, Apr 1990.

[28] Patrick A. Lee and Daniel S. Fisher. Anderson localization in two dimensions. *Phys. Rev. Lett.*, 47:882–885, Sep 1981.

[29] D J Thouless and S Kirkpatrick. Conductivity of the disordered linear chain. *Journal of Physics C: Solid State Physics*, 14(3):235, 1981.

[30] Christoph W Groth, Michael Wimmer, Anton R Akhmerov, and Xavier Waintal. Kwant: a software package for quantum transport. *New J. Phys.*, 16(6):063065, 2014.

[31] Patrick R. Amestoy, Iain S. Duff, Jean-Yves L'Excellent, and Jacko Koster. A fully asynchronous multifrontal solver using distributed dynamic scheduling. *SIAM Journal on Matrix Analysis and Applications*, 23(1):15–41, 2001.

[32] Dominique Dresen. *Quantum transport of non-interacting electrons in 2D Systems of arbitrary geometry.* PhD thesis, RWTH Aachen University, 2014.

[33] A. Mrenca-Kolasiński and B. Szafran. Imaging backscattering in graphene quantum point contacts. arXiv:1704.08460, 2017.

[34] M. A. Eriksson, R. G. Beck, M. Topinka, J. A. Katine, R. M. Westervelt, K. L. Campman, and A. C. Gossard. Cryogenic scanning probe characterization of semiconductor nanostructures. *Appl. Phys. Lett.*, 69(5):671–673, 1996.

[35] G. Binnig, H. Rohrer, Ch. Gerber, and E. Weibel. Surface studies by scanning tunneling microscopy. *Phys. Rev. Lett.*, 49:57–61, Jul 1982.

[36] D A Wharam, T J Thornton, R Newbury, M Pepper, H Ahmed, J E F Frost, D G Hasko, D C Peacock, D A Ritchie, and G A C Jones. One-dimensional transport and the quantisation of the ballistic resistance. *J. Phys. C: Solid State Phys.*, 21(8):L209, 1988.

[37] M. P. Jura, M. A. Topinka, L. Urban, A. Yazdani, H. Shtrikman, L. N. Pfeiffer, K. W. West, and D. Goldhaber-Gordon. Unexpected features of branched flow through high-mobility two-dimensional electron gases. *Nature Physics*, 756:841, 2007.

[38] Eric J. Heller and Scot Shaw. Branching and fringing in microstructure electron flow. *Int. J. Mod. Phys. B*, 17(22n24):3977–3987, 2003.

[39] Cosimo Gorini, Dietmar Weinmann, and Rodolfo A. Jalabert. Scanning-gate-induced effects in nonlinear transport through nanostructures. *Phys. Rev. B*, 89:115414, Mar 2014.

[40] R. Crook, C. G. Smith, A. C. Graham, I. Farrer, H. E. Beere, and D. A. Ritchie. Imaging fractal conductance fluctuations and scarred wave functions in a quantum billiard. *Phys. Rev. Lett.*, 91:246803, Dec 2003.

[41] A. M. Burke, R. Akis, T. E. Day, Gil Speyer, D. K. Ferry, and B. R. Bennett. Periodic scarred states in open quantum dots as evidence of quantum darwinism. *Phys. Rev. Lett.*, 104:176801, Apr 2010.

[42] A A Kozikov, D Weinmann, C Rössler, T Ihn, K Ensslin, C Reichl, and W Wegscheider. Imaging magnetoelectric subbands in ballistic constrictions. *New J. Phys.*, 15(8):083005, 2013.

[43] R Steinacher, A A Kozikov, C Rössler, C Reichl, W Wegscheider, T Ihn, and K Ensslin. Scanning-gate-induced effects and spatial mapping of a cavity. *New J. Phys.*, 17(4):043043, 2015.

[44] Christina Pöltl, Aleksey Kozikov, Klaus Ensslin, Thomas Ihn, Rodolfo A. Jalabert, Christian Reichl, Werner Wegscheider, and Dietmar Weinmann. Classical origin of conductance oscillations in an integrable cavity. *Phys. Rev. B*, 94:195304, Nov 2016.

[45] A. A. Kozikov, D. Weinmann, C. Rössler, T. Ihn, K. Ensslin, C. Reichl, and W. Wegscheider. Electron backscattering in a cavity: Ballistic and coherent effects. *Phys. Rev. B*, 94:195428, Nov 2016.

[46] B. Hackens, F. Martins, T. Ouisse, H. Sellier, S. Bollaert, X. Wallart, A. Cappy, J. Chevrier, V. Bayot, and S. Huant. Imaging and controlling electron transport inside a quantum ring. *Nature Physics*, 2:826–830, 12 2006.

[47] F. Martins, B. Hackens, M. G. Pala, T. Ouisse, H. Sellier, X. Wallart, S. Bollaert, A. Cappy, J. Chevrier, V. Bayot, and S. Huant. Imaging electron wave functions inside open quantum rings. *Phys. Rev. Lett.*, 99:136807, Sep 2007.

[48] M. G. Pala, B. Hackens, F. Martins, H. Sellier, V. Bayot, S. Huant, and T. Ouisse. Local density of states in mesoscopic samples from scanning gate microscopy. *Phys. Rev. B*, 77:125310, Mar 2008.

[49] Michael T. Woodside and Paul L. McEuen. Scanned probe imaging of single-electron charge states in nanotube quantum dots. *Science*, 296(5570):1098–1101, 2002.

[50] S Schnez, J Güttinger, C Stampfer, K Ensslin, and T Ihn. The relevance of electrostatics for scanning-gate microscopy. *New Journal of Physics*, 13(5):053013, 2011.

[51] Damien Cabosart, Sébastien Faniel, Frederico Martins, Boris Brun, Alexandre Felten, Vincent Bayot, and Benoit Hackens. Imaging coherent transport in a mesoscopic graphene ring. *Phys. Rev. B*, 90:205433, Nov 2014.

[52] A. Pioda, S. Kičin, T. Ihn, M. Sigrist, A. Fuhrer, K. Ensslin, A. Weichselbaum, S. E. Ulloa, M. Reinwald, and W. Wegscheider. Spatially resolved manipulation of single electrons in quantum dots using a scanned probe. *Phys. Rev. Lett.*, 93:216801, Nov 2004.

[53] Parisa Fallahi, Ania C. Bleszynski, Robert M. Westervelt, Jian Huang, Jamie D. Walls, Eric J. Heller, Micah Hanson, and Arthur C. Gossard. Imaging a single-electron quantum dot. *Nano Letters*, 5(2):223–226, 2005. PMID: 15794600.

[54] Ania C. Bleszynski, Floris A. Zwanenburg, R. M. Westervelt, Aarnoud L. Roest, Erik P. A. M. Bakkers, and Leo P. Kouwenhoven. Scanned probe imaging of quantum dots inside inas nanowires. *Nano Letters*, 7(9):2559–2562, 2007. PMID: 17691848.

[55] K. Kolasiński and B. Szafran. Simulations of imaging of the local density of states by a charged probe technique for resonant cavities. *Phys. Rev. B*, 88:165306, Oct 2013.

[56] V. Gasparian, T. Christen, and M. Büttiker. Partial densities of states, scattering matrices, and green's functions. *Phys. Rev. A*, 54:4022–4031, Nov 1996.

[57] Satofumi Souma and Akira Suzuki. Local density of states and scattering matrix in quasi-one-dimensional systems. *Phys. Rev. B*, 65:115307, Feb 2002.

[58] M. Büttiker. *Electronic properties of multilayers and low-dimensional semiconductors structures.* Plenum Press, 1990.

[59] M. Büttiker and T. Christen. *Chapter in Quantum transport in semiconductor submicron structures.* Kluwer academic publishers, 1996.

[60] G. Iannaccone. General relation between density of states and dwell times in mesoscopic systems. *Phys. Rev. B*, 51:4727–4729, Feb 1995.

[61] Damien Cabosart, Alexandre Felten, Nicolas Reckinger, Andra Iordanescu, Sébastien Toussaint, Sébastien Faniel, and Benoît Hackens. Recurrent quantum scars in a mesoscopic graphene ring. *Nano Letters*, 17(3):1344–1349, 2017. PMID: 28166405.

[62] Liang Huang, Ying-Cheng Lai, David K. Ferry, Stephen M. Goodnick, and Richard Akis. Relativistic quantum scars. *Phys. Rev. Lett.*, 103:054101, Jul 2009.

[63] D. A. Wisniacki, E. Vergini, R. M. Benito, and F. Borondo. Signatures of homoclinic motion in quantum chaos. *Phys. Rev. Lett.*, 94:054101, Feb 2005.

[64] D. A. Wisniacki, E. Vergini, R. M. Benito, and F. Borondo. Scarring by homoclinic and heteroclinic orbits. *Phys. Rev. Lett.*, 97:094101, Sep 2006.

[65] R. Steinacher, C. Pöltl, T. Krähenmann, A. Hofmann, C. Reichl, R. A. Jalabert, D. Weinmann, W. Wegscheider, K. Ensslin, and T. Ihn. Scanning gate experiments: from strongly to weakly invasive probes. *arXiv:1709.08559*, 2017.

[66] V. S. Vladimirov. *Equations of mathematical physics.* MARCEL DEKKER, INC., New York, 1971.

[67] W. Szewc. *Theory and Simulation of Scanning Gate Microscopy Applied to the Investigation of Transport in Quantum Point Contacts*. PhD thesis, Université de Strasbourg, 2013.

[68] Adel Abbout, Gabriel Lemarié, and Jean-Louis Pichard. Thermal enhancement of interference effects in quantum point contacts. *Phys. Rev. Lett.*, 106:156810, Apr 2011.

[69] Ousmane Ly, Rodolfo A. Jalabert, Steven Tomsovic, and Dietmar Weinmann. Partial local density of states from scanning gate microscopy. *Phys. Rev. B*, 96:125439, Sep 2017.

[70] Michael G. Brown, John A. Colosi, Steven Tomsovic, Anatoly L. Virovlyansky, Michael A. Wolfson, and George M. Zaslavsky. Ray dynamics in long-range deep ocean sound propagation. *The Journal of the Acoustical Society of America*, 113(5):2533–2547, 2003.

[71] L. D. Landau and E. M. Lifshitz. *Quantum Mechanics, Non-relativistic Theory*. Pergamon Press, 1991.

[72] Rodolfo A. Jalabert and Dietmar Weinmann. Scattering approach to scanning gate microscopy. *Physica E: Low-dimensional Systems and Nanostructures*, 74:637 – 643, 2015.

[73] A. G. Aronov V. M. Gasparian and Ute Gummich. Transmission of waves through one-dimensional random layered systems. *J. Phys: Condens. Matter*, 3:3023–3039, 1991.

[74] Eric J. Heller. Bound-state eigenfunctions of classically chaotic hamiltonian systems: Scars of periodic orbits. *Phys. Rev. Lett.*, 53:1515–1518, Oct 1984.

[75] John H. Davies, Ivan A. Larkin, and E. V. Sukhorukov. Modeling the patterned two-dimensional electron gas: Electrostatics. *Journal of Applied Physics*, 77(9):4504–4512, 1995.

[76] Samuel Häusler, Shuta Nakajima, Martin Lebrat, Dominik Husmann, Sebastian Krinner, Tilman Esslinger, and Jean-Philippe Brantut. Scanning gate microscope for cold atomic gases. *Phys. Rev. Lett.*, 119:030403, Jul 2017.

[77] H Sellier, B Hackens, M G Pala, F Martins, S Baltazar, X Wallart, L Desplanque, V Bayot, and S Huant. On the imaging of electron transport in semiconductor quantum structures by scanning-gate microscopy: successes and limitations. *Semicond. Sci. Tech.*, 26(6):064008, 2011.

Ousmane Boune Oumar LY

Scanning gate microscopy as a tool for extracting local electronic propoerties in quantum transport

Résumé

La technique de la microscopie à grille de balayage (SGM) consiste à mesurer la conductance d'un gaz bi-dimensionnel d'électrons (2DEG) sous l'influence d'une pointe balayant la surface de l'échantillon. Dans ce travail, une approche analytique complétée par des simulations numériques est développée pour étudier la relation entre les mesures SGM et les propriétés électroniques locales dans des systèmes mésoscopiques. La correspondance entre la réponse SGM et la densité locale partielle (PLDOS) est étudiée pour un contact quantique entouré d'un 2DEG en présence ou en absence de désordre, pour une pointe pérturbative ou non-pérturbative. Une correspondance SGM-PLDOS parfaite est trouvée pour des transmissions entières et des pointes locales. La dégradation de la correspondance en dehors de cette situation est étudiée. D'autre part, la liaison entre la réponse SGM et la transformée de Hilbert de la densité locale est discutée. Pour étudier le rôle de la force de la pointe sur la conductance SGM, une formule analytique donnant la conductance totale est obtenue. Dans le cas d'une pointe à taille finie nous proposons une méthode basée sur les fonctions de Green permettant de calculer la conductance en connaissant les propriétés non-pérturbées. En plus, nous avons étudié la dépendance des branches de la PLDOS en fonction de l'énergie de Fermi.

Mots-clés : Transport quantique, théorie de la diffusion, contact quantique, quantification de la conductance, simulations numériques

Résumé en anglais

The scanning gate microscopy (SGM) technique consists in measuring the conductance of a two dimensional electron gas (2DEG) under the influence of a scanning tip. In this work, an analytical approach complemented by numerical simulations is developed to study the connection between SGM measurements and local electronic properties in mesoscopic devices. The connection between the SGM response and the partial local density of states (PLDOS) is studied for the case of a quantum point contact surrounded by clean or disordered 2DEG for perturbative or non-perturbative, local or extended tips. An SGM-PLDOS correspondence is found for integer transmissions and local tips. The degradation of this correspondence out of these conditions is studied. Moreover, a presumed link between the SGM response and the Hilbert transform of the LDOS is discussed. To study the role of the tip strength, an analytical formula giving the full conductance in the case of local tips is obtained. Furthermore, a Green function method enabling to calculate the quantum conductance in the presence of a finite size tip in terms of the unperturbed properties is proposed. Finally the dependence of the PLDOS branches on the Fermi energy is studied.

Keywords : Quantum transport, scattering theory, quantum point contacts, conductance quantization, numerical simulations.